Università degli Studi di Genova
Department of Physics

PhD Thesis in Physics

Superconducting magnets for future accelerators

PhD Candidate
Alessandro Maria Ricci

Supervisor
Dr. Pasquale Fabbricatore

PhD Cycle XXXII

This thesis has been written in collaboration with the Istituto Nazionale di Fisica Nucleare (INFN).

External Referees

Prof. Marco Breschi - Università di Bologna

Prof. Michela Greco - Università di Torino

οὐ γὰρ ὡς ἀγγεῖον ὁ νοῦς ἀποπληρώσεως ἀλλ' ὑπεκκαύματος μόνον ὥσπερ ὕλη δεῖται, ὁρμὴν ἐμποιοῦντος εὑρετικὴν καὶ ὄρεξιν ἐπὶ τὴν ἀλήθειαν.

Plutarch, *The Art of Listening*, 48a

Contents

Preface

The Large Hadron Collider (LHC) at CERN, which is now in operation for ten years, is not only the largest and more powerful particle accelerator in the world, but also constitutes one of the greatest applications of the superconducting magnet technology. Nevertheless, the need to increase both the luminosity in the next future and the energy in more far future is demanding for the developments of new and more challenging superconducting magnets generating higher magnetic fields. Presently all laboratories worldwide involved in the superconducting magnet technology for accelerators are performing R&D activities aimed to the development of a high field superconducting magnet (16 T) for the Future Circular Collider, an accelerator for 50-TeV energy protons (7 times higher than the energy of the LHC beams). The needed technology demands for the use of superconducting material (Niobium Tin) well-known but of difficult application requiring a considerable development before it can be used for 16-T magnet. It is also under study the possible use of cables based on high critical temperature superconductors (HTS), which are even more difficult and have never been used in accelerators.

The design of the superconducting magnets for accelerators is closely related to the physics of the accelerator. In particular, the optics of the beams is determined by the quality of the magnetic field controlled by dipoles, quadrupoles and higher-order correctors. To a greater extent than existing magnets, the optimization of a magnetic design for the dipoles of the Future Circular Collider, for energies of 100 TeV in the center of mass, has many critical aspects partly related to the intrinsic limitations of superconducting cables (critical fields and currents) and partly to the need to develop stable geometric layouts with respect to geometric variations (mechanical deformation or manufacturing tolerances).

This thesis is focused on the optimization of the field quality for the magnets in the twin-coil configuration (for FCC as for LHC the two openings of the dipoles that curve the proton beams circulating in the opposite direction are assembled in a single cold mass). For this class of magnets, the magnetic

cross-talk between the apertures presents considerable complications considering that in a dipole the components of higher-order multipoles must be at the most of the order of 10^{-4} with respect to the main dipole field. We have developed analytical methodologies, complemented with numerical analyzes, to minimize magnetic cross-talk through suitable asymmetrical configurations. We have applied these methodologies in the various studies carried out for the development of magnets for the Future Circular Collider contributing to finalize a design, which has been presented as the baseline of an European project funded within H2020 framework, named EuroCirCol. We have also applied the developed methods for studying possible improvements to the present design of the recombination dipoles (called D2) for the high luminosity upgrade of LHC. These are NbTi magnets with a strong cross-talk between the two apertures and are under construction at ASG Superconductors in Genova with a design developed at INFN Genova. At the same time, we have developed the 3D electromagnetic models of both magnet classes. In particular, we have been responsible for the 3D electromagnetic simulations of the EuroCirCol magnet. Finally, we have helped to develop a preliminary design of the FCC recombination dipoles (called DARD), which have required a completely different approach with respect to the D2 magnets for LHC.

The thesis is structured in two main sections with five chapters. The first section (including three chapters) reports the theoretical background and the developed methods. The second section (two further chapters) reports the design activities of the magnets for the high luminosity upgrade of LHC and for FCC.

- The first chapter is dedicated to a description of the application of superconductivity to particle accelerators.
- In the second chapter, the complex formalism for the magnetic field is presented and the concept of integrated multipole for an accelerator magnet is introduced.
- In the third chapter, the developed methods for optimizing the field quality in magnets with magnetic cross-talk are presented.
- The fourth chapter is dedicated to the design activities of the FCC dipole, requiring a strong interplay between magnetic and mechanical design.
- The fifth chapter illustrates the proposal for optimizing the field quality in D2 magnets and the preliminary design of the recombination dipoles for FCC.

Part I

Theoretical Framework

Chapter 1

Superconducting Accelerator Magnets

1.1 Introduction

The main scope of the High-Energy Physics (HEP) is to study the internal structure of the particles. The research is carried out by smashing particles into pieces and by analyzing the nature and the features of the pieces. The charged particles are broken by accelerating them at high momenta and either by blasting them against a fixed target or by colliding them among themselves. To achieve high event rates, the particles are bunched together into high-intensity beams, which are focused near the targets or collision points. The more elementary the particles, the higher the energy needed to smash them. Experiments at the proton scale require beam energies of the order of 1 TeV or more.

Nowadays, the most powerful accelerator is the Large Hadron Collider (LHC) at CERN, near Geneva, which accelerates proton beams at an energy of about 7 TeV per beam [12]. A research infrastructure of such a scale is the result of advanced technologies, which required a long R&D activity. The superconducting magnets, which bend and focus the high-energy beams, have been among the most costly and the most challenging components of the machine. In the last 30 years, the superconducting magnets have been a fundamental technology to realize all the high-energy accelerators (Tevatron, HERA, RHIC, LHC).

In this chapter, we will introduce the layout of the high-energy particle accelerators and we will illustrate the state of art of the superconducting magnet technology. A more detailed discussion can be found in Ref. [7, 14].

1.2 Particle accelerators

1.2.1 Layout of the particle accelerators

There are two main types of particle accelerators: linear accelerators, called *linacs*, and circular accelerators. In a linac, the charged particles travel along a straight trajectory and go successively through a large number of accelerating stations. In a circular accelerator, the beam is circulated many times around a closed orbit. A circular accelerator only relies on a few accelerating stations, through which the particles go at every run. However, it needs a large number of guiding elements, which are distributed over the accelerator arcs. The most powerful machines are made up of several stages, which progressively raise the beam energy. Each stage is a fully-fledged accelerator, which can be of either linear or circular.

The last stage of these accelerator chains is a closed-orbit ring, called *main ring*. It works in three phases, as a synchrotron-type accelerator. In the *injection* phase, the beam is prepared in various pre-accelerators and is injected in the main ring at low-energy. In the *acceleration* phase, the beam is accelerated to nominal energy and, in the *storage* phase, the beam is made available for physics experiments.

The main ring is usually made up of several *bending arcs*, separated by almost-straight *insertion regions*. The insertion regions house the accelerating stations and the beam injection and extraction lines. In the case of a collider ring, the two counter-rotating beams are designed to cross in the middle of at least one of the insertion regions. The points where the beams cross are called *interaction points* and the space around them is surrounded by a detector array.

1.2.2 Accelerating stations and element guides

The particles are accelerated by using electric fields, generated by Radio-Frequency (RF) resonant cavities, which can be either normal conducting or superconducting [15].

The beams are bended and focused by using magnetic fields, generated by normal or superconducting magnets. The Lorentz force, $\boldsymbol{F}_L$, exerted by the magnetic field, $\boldsymbol{B}$, on a charge, q, traveling at a velocity, $\boldsymbol{v}$, is given by Lorentz' law

$$\boldsymbol{F}_L = q\,\boldsymbol{v} \times \boldsymbol{B}\,. \tag{1.1}$$

The Lorentz force is perpendicular to the directions of $\boldsymbol{v}$ and $\boldsymbol{B}$. Its only action is to bend the particle trajectory. If $\boldsymbol{v}$ and $\boldsymbol{B}$ are perpendicular, the

Table 1.1: Curvature radius versus magnetic field for a 10-TeV synchrotron-type, proton accelerator [7].

	B(T)	r(km)	Circumference (km)
Low field	2	16.7	105
Medium field	6	5.6	35
High field	10	3.3	21

particle is deviated on an arc of circle, tangent to $\boldsymbol{v}$ and perpendicular to $\boldsymbol{B}$, and of curvature radius, r, which can be computed by the formula

$$r = \frac{\gamma m v}{qB} = \frac{p}{qB} \approx \frac{p\,(\text{GeV})}{0.3\,q_e B}\,, \tag{1.2}$$

where γ is Lorentz's factor, m is the particle mass and p its linear momentum. For convenience, we approximate the formula by using a factor 0.3 for the light speed, the particle charge in units of electron charge, q_e, and the linear momentum in GeV. Eq. (1.2) shows that, during the acceleration phase, B must be ramped up linearly with p to maintain a constant curvature radius.

Let us use Eq. (1.2) to dimension a 10-TeV proton accelerator, choosing successively three different values for B. The results are presented in Table 1.1. They show that, when we design a large synchrotron-type accelerator, a trade-off must be found between, on one hand, the availability of land and the tunneling costs, and, on the other hand, the feasibility and costs of the electromagnets.

For LHC at CERN, the curvature radius of the existing LEP tunnel limited the r-value to 2.5 km. The maximum magnetic field generated by superconducting magnets is 8.3 T. From Eq. (1.2) follows that the maximum beam energy is 7 TeV.

1.2.3 Magnet classification

The electromagnets around an accelerator main ring can be classified into three categories: *arc magnets*, *insertion and final focusing magnets* and *detector magnets*.

The magnets distributed over the ring arcs have two main functions: bending the beam around a closed and constant orbit and focusing it to achieve proper size and intensity. In large machines, the bending and focusing functions are separated: the former is provided by dipole magnets, whereas

the latter is provided by pairs of focusing/defocusing quadrupole magnets (see section 1.3). These magnets are arranged around the arcs in a regular lattice of cells, made up of a focusing quadrupole, a string of bending dipoles, a defocusing quadrupole and another string of bending dipoles [5, 14]. This arrangement is referred to as the *FODO cell* (Focusing, zero, Defocusing, zero). Several correction magnets are also implemented within each cell to allow better control of the beam optics. Due to their large number, the arc magnets are usually mass-produced in industry.

In addition to the arc magnets, an accelerator main ring includes several special magnets. Some of them are used to transport the beam from the injector chain to the main ring. Sets of strongly focusing quadrupole magnets are located near the targets or collision points. The design and fabrication of the insertion and final focusing magnets are very similar to those of the arc dipole and quadrupole magnets.

The physics experiments surrounding the targets or collision points usually rely on large magnets systems, which are embedded in the detector array. The magnet system is based either on a solenoid or on a toroid or on a combination of them. The technology of detector magnets is very different from that of accelerator magnets.

1.2.4 Example: LHC at CERN

Figure 1.1 shows the schematic layout of the Large Hadron Collider (LHC) at CERN [12]. The LHC ring is divided into 8 bending arcs, separated by 8 insertion regions. The ring circumference is about 27 km and each insertion region is about 530 m long. The two counter-rotating proton beams are circulated around the eight arcs and cross in the middle of four insertion regions. The accelerating stations are located in one of the insertion regions, where the beams do not cross. They are made up of 8 single-cell, RF cavities per beam.

The 8 bending arcs of LHC have identical magnet lattices. They include 23 FODO cells, which are made up of 6 dipole magnets, 1 focusing and 1 defocusing quadrupole magnet, and several corrector magnets. The arc dipole and quadrupole magnets have two apertures, housing pipes for the two counter-rotating proton beams. Such magnets are called *twin-aperture* magnets. The arc dipole magnets are 14.3 m long and are designed to produce a magnetic field of 8.33 T during the storage phase. The arc quadrupole magnets are 3.1 m long and designed to operate with a maximum field gradient of 223 T/m. The inner bore diameter of each coil is 56 mm for both magnet types. The cell length is about 106.9 m.

The final focusing is provided by the so-called *inner triplets*, made up

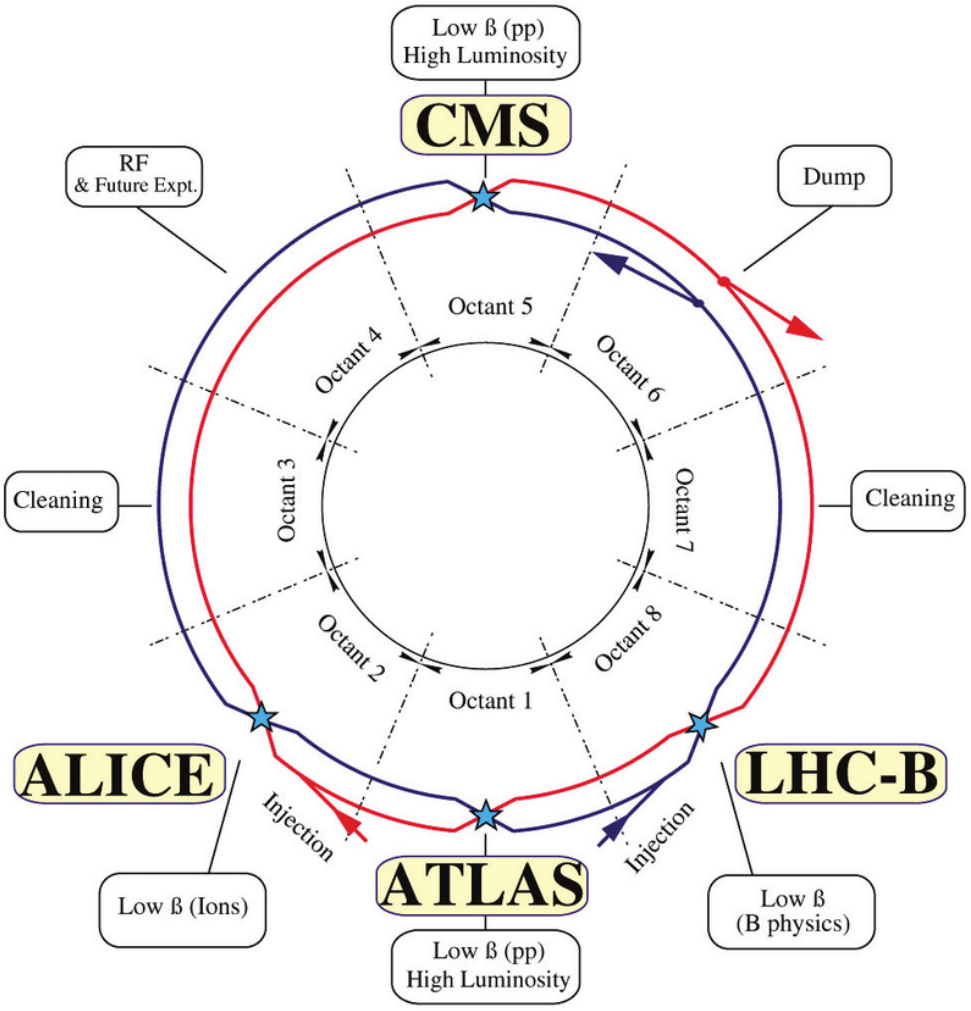

Figure 1.1: Schematic layout of the Large Hadron Collider (LHC) at CERN [7].

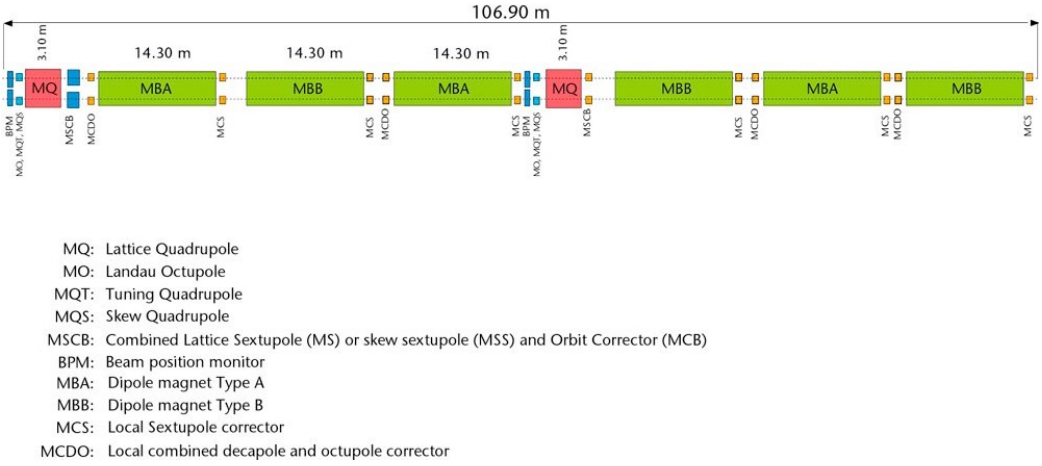

Figure 1.2: Cell of the magnet lattice of the LHC arcs [7].

of four, high-field-gradient quadrupole magnets. These magnets have one large aperture with a 70-mm inner bore diameter, and accommodate the two beams within a single pipe.

1.3 Dipole and quadrupole magnets

1.3.1 Coordinate systems

Let $(\Omega, \boldsymbol{X}, \boldsymbol{Y}, \boldsymbol{Z})$ designate a Cartesian coordinate system, and let us consider an accelerator ring, whose design orbit is planar and is located in the $(\Omega, \boldsymbol{X}, \boldsymbol{Z})$ plane, as represented in Fig. 1.3. Let Ω be the center of the design orbit and r its curvature radius. Let a particle of mass m travel along the orbit with a relativistic velocity $\boldsymbol{v}$. Furthermore, let $(O, \boldsymbol{x}, \boldsymbol{y}, \boldsymbol{z})$ be a Cartesian coordinate system, such that the center O is a given point of the design orbit, the x-axis defines the horizontal direction, the y-axis defines the vertical direction, and the z-axis corresponds to the main direction of particle motion.

1.3.2 Normal dipole magnet

An ideal normal dipole magnet, whose center is positioned at O, produces, within its aperture, a uniform magnetic field, parallel to the y-axis (see Fig. 1.4), and such that

$$B_x = 0\,, \qquad B_y = B_1 \qquad \text{and} \qquad B_z = 0\,, \tag{1.3}$$

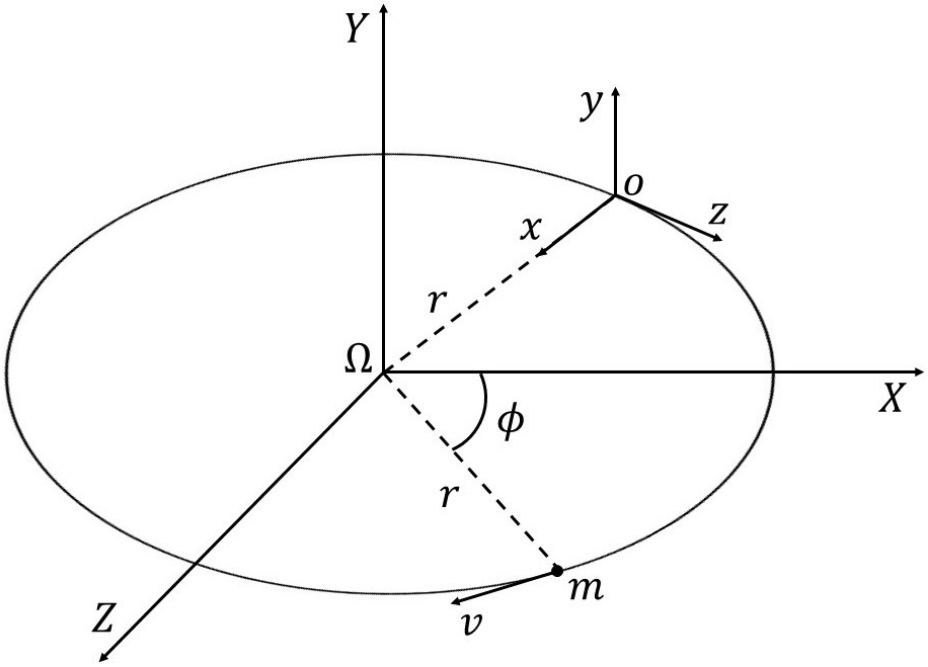

Figure 1.3: Coordinate systems associated with the design orbit of an accelerator ring.

where B_x, B_y and B_z are, respectively, the x-, y- and z-components of the magnetic field, and B_1 is a constant, referred to as the *dipole field strength* and expressed in T.

A charged particle describes an arc of circle parallel to the $(O, \boldsymbol{x}, \boldsymbol{z})$ plane, traveling along the direction of the z-axis through the aperture of a normal dipole magnet of length l_d. The angular deflection, ϕ, of the particle trajectory is defined as

$$\phi = \frac{l_d}{r} \approx \frac{0.3\, q_e B_1 l_d}{p\,(\mathrm{GeV})}\,, \tag{1.4}$$

where we used Eq. (1.2) to make explicit the curvature radius, r.

The effect of a dipole magnet on a beam of charged particles can be compared to the effect of a prism on a light ray. The beam is deflected and dispersed.

For the storage phase of LHC, we have: $B_1 = 8.3$ T, $l_d = 14.3$ m and $p = 7$ TeV. It follows from Eq. (1.4) that a single arc dipole magnet bends the proton trajectory by an angle $\phi \approx 5.1$ mrad. Hence, a full (2π) rotation requires a total of 1232 arc dipole magnets.

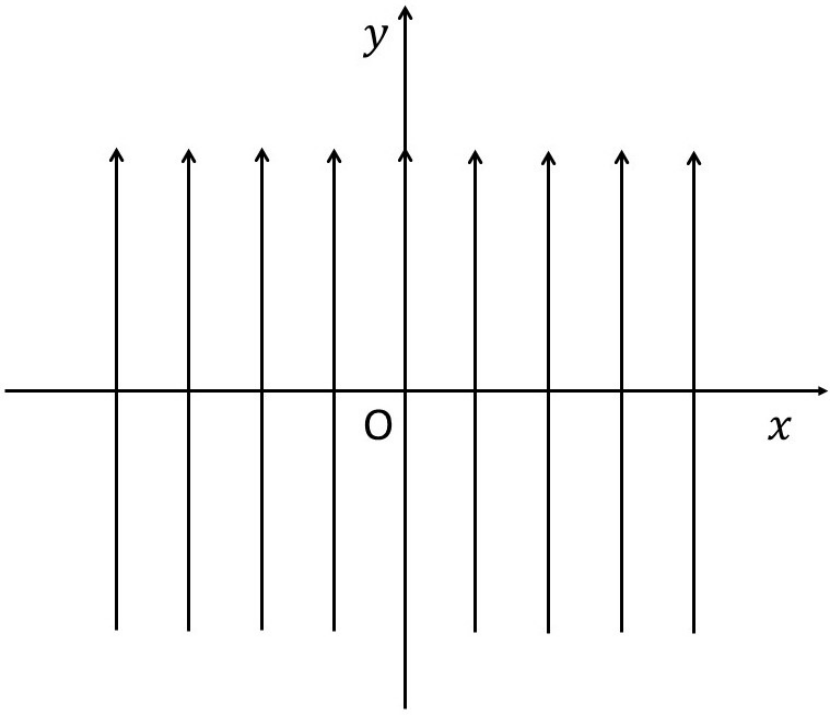

Figure 1.4: Magnetic field lines, generated by an ideal normal dipole magnet.

1.3.3 Normal quadrupole magnet

An ideal normal quadrupole magnet, whose center is positioned at O, produces, within its aperture, a two-dimensional magnetic field, parallel to the $(O, \boldsymbol{x}, \boldsymbol{y})$ plane and such that

$$B_x = gy\,, \qquad B_y = gx \qquad \text{and} \qquad B_z = 0\,, \tag{1.5}$$

where g is a constant, referred to as the *quadrupole field gradient* and expressed in T/m. The field lines of an ideal normal quadrupole magnet are hyperbolas of center O, whose asymptotes are the bisectors of the first and second quadrant (see Fig. 1.5). The ideal normal quadrupole magnet generates a magnetic field, which increases linearly as a function of the distance from the magnet center.

A beam of positively charged particles, traveling along the direction of the z-axis through the aperture of an ideal normal quadrupole magnet, is horizontally focused and vertically defocused when g is positive (see Figures 1.6 and 1.7). Conversely, the beam is vertically focused and horizontally defocused when g is negative. In reference to its action along the x-axis (on a beam of positively charged particles traveling in the positive z-direction),

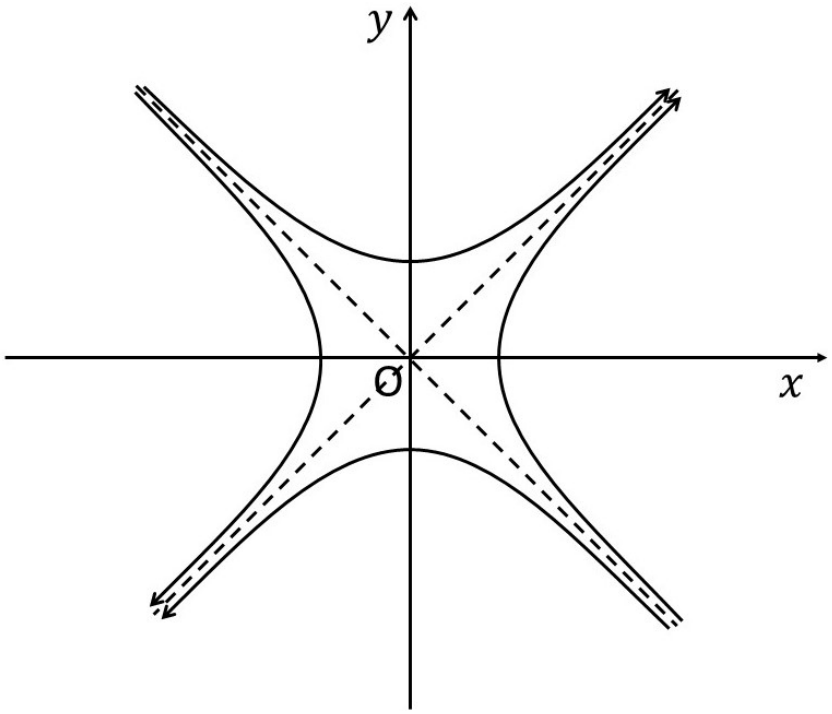

Figure 1.5: Magnetic field lines, generated by an ideal normal quadrupole magnet.

a magnet with a positive gradient is called a *focusing* quadrupole magnet, while a magnet with a negative gradient is called a *defocusing* quadrupole magnet. To obtain a net focusing effect along both x- and y-axes, focusing and defocusing quadrupole magnets must be alternated in the magnet lattice [5, 14].

The effects of focusing/defocusing quadrupole magnets on a beam of charged particles are similar to those of convex/concave lenses on a light ray. By analogy, the focusing/defocusing effect of a normal quadrupole magnet of length l_q can be characterized by the *focal length*, f, given by

$$f = \frac{1}{k\, l_q}\,, \tag{1.6}$$

where f is taken from the magnet end, where the beam exits (see Figures 1.6 and 1.7), and k is the *normalized field gradient*, expressed in m^{-2} and defined as

$$k = \frac{g}{Br} \approx \frac{0.3\, q_e g}{p\,(\mathrm{GeV})}\,. \tag{1.7}$$

Eq. (1.6) shows that in order to keep the focal length constant during the acceleration phase, k must be kept constant. Eq. (1.7) shows that in

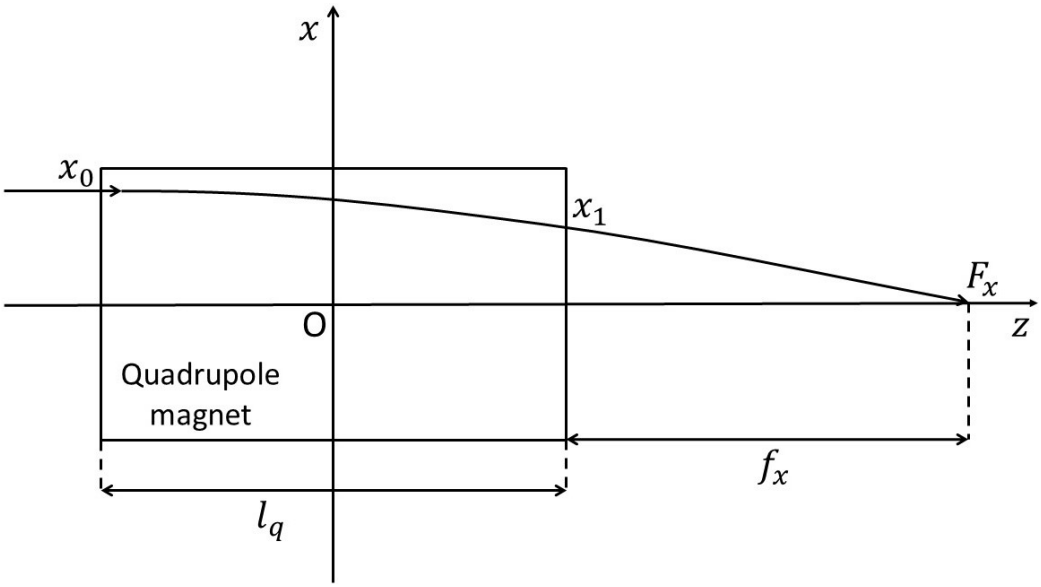

Figure 1.6: Horizontal focusing of positively charged particles circulating through the aperture of an ideal normal quadrupole magnet with a positive gradient.

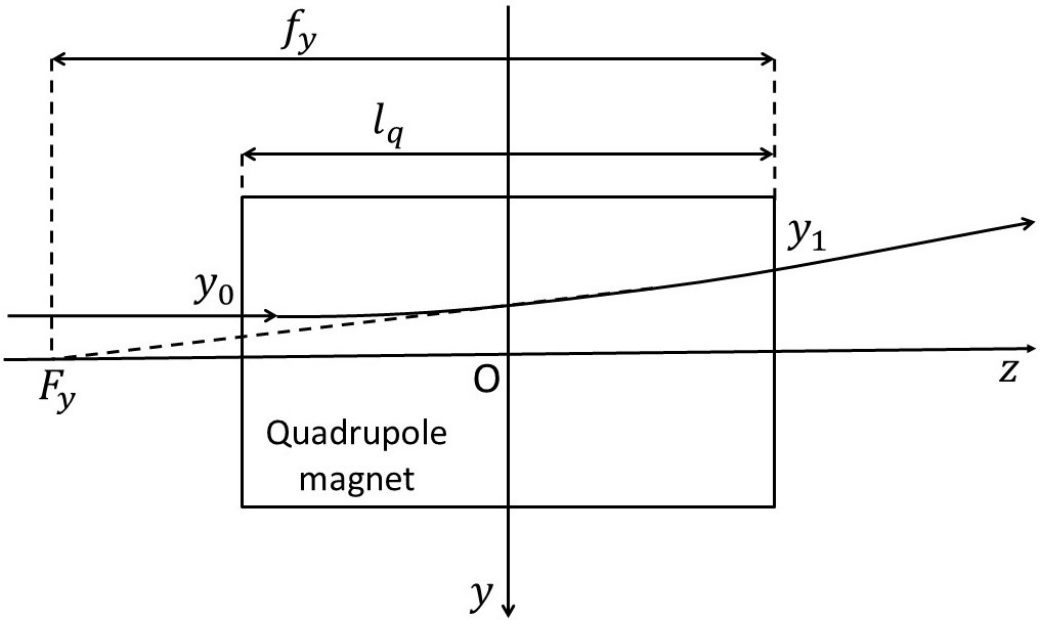

Figure 1.7: Vertical defocusing of positively charged particles circulating through the aperture of an ideal normal quadrupole magnet with a positive gradient.

order to keep k constant, g must be raised in proportion to beam energy. As a result, during the acceleration phase, the arc dipole and quadrupole magnets are ramped up together so as to ensure that the bending dipole field strength and the focusing/defocusing quadrupole field gradients track the beam energy.

For the storage phase of the LHC, we have: $g = 223$ T/m, $l_q = 3.1$ m and $p = 7$ TeV. It follows from Eq. (1.7) that $k \approx 0.01$ m^{-2}, while Eq. (1.6) yields $f = 32.3$ m. The LHC arcs count a total number of 386 quadrupole magnets.

1.4 Superconducting particle accelerators

1.4.1 Why superconductivity?

Throughout the years, the quest for elementary particles promoted the development of ever more powerful accelerators. Eq. (1.2) shows that, for a synchrotron, the particle energy is directly proportional to the product rB. Hence, to reach higher energies, one must increase either the bending radius or the magnetic field generated by the arc dipoles (or both). Increasing the bending radius means to dig a longer tunnel. Increasing the magnetic field above 2 T implies to use of superconducting magnets. Since the late 1970s, the trade-off between tunneling costs, magnet development costs, and accelerator operating costs is in favor of using superconducting magnets to generate the highest possible fields and field gradients [5].

Superconductivity is a unique property exhibited by some materials at low temperatures, where the resistivity drops to zero. As a result, materials in the superconducting state can transport current without power dissipation by the Joule effect. This offers at least three advantages for the large magnet systems of the accelerators:

1. a significant reduction in electrical power consumption;

2. the possibility of relying on much higher current densities in magnets;

3. a significant reduction of the overall magnet dimensions.

However, there are at least three drawbacks in using superconducting magnets:

1. superconductors generate magnetization effects, which result in field distortions that have to be corrected;

2. to reach the superconducting state, the magnets must be cooled down and maintained at low temperatures, which require large cryogenic systems;

3. an energized magnet, initially in the superconducting state, can quickly and irreversibly switch back to the normal resistive state, in a phenomenon called *quench*.

The occurrence of a quench causes an instantaneous beam loss and requires that the magnet ring is rapidly ramped down to limit the conductor heating and to avoid possible damages in the quenching magnet. Once the quenching magnet is discharged, it can be cooled down again and restored into the superconducting state. Then, the machine operations can resume. A quench is seldom fatal, but it is always a serious disturbance. All must be done to prevent it from happening and all cautions must be taken to ensure the safety of the installation when it does happen.

1.4.2 Past and present accelerators

The first large-scale application of superconductivity was the Tevatron, a proton synchrotron with a circumference of 6.3 km, completed in 1983 at Fermi National Accelerator Laboratory (FNAL, also referred to as Fermilab) near Chicago, in Illinois. The Tevatron operated as a proton/antiproton collider with a maximum energy of 980 GeV per beam. It relied on about 1000 superconducting dipoles and quadrupoles, with a maximum operating magnetic field of 4.3 T in the arc dipoles.

The second large particle accelerator to rely massively on superconducting magnets was HERA (Hadron Elektron Ring Anlage), completed in 1992 at DESY (Deutsches Elektronen-SYnchrotron) laboratory near Hamburg, in Germany. HERA was an electron/proton collider with a circumference of 6.3 km. It included two large rings positioned on top of each other: an electron ring, relying on conventional magnets, and a proton ring, relying on superconducting magnets. In the proton ring, the superconducting arc dipoles generated a maximum operating magnetic field of 5.3 T. The electron beam was accelerated to a maximum energy of 27.5 GeV. Instead, the proton beam was accelerated to a maximum energy of 920 GeV.

Brookhaven National Laboratory (BNL), on Long Island, in New York, completed in 2000 the construction of the Relativistic Heavy Ion Collider (RHIC). RHIC has been the first heavy-ion collider in the world. Nowadays, it is one of the two only operating heavy-ion colliders and the only spin-polarized proton collider. The proton beams are accelerated in two identical

Table 1.2: Main features of the major superconducting particle accelerators [7, 30].

Laboratory	FNAL	DESY	BNL	CERN
Machine name	Tevatron	HERA	RHIC	LHC
Circumference (km)	6.3	6.3	3.8	27
Particle type	$p\bar{p}$	ep	pp/heavy ions	pp
Energy/beam (TeV)	0.98	0.92[1]	0.25 / 0.1[2]	7
Arc dipole magnets				
Number	776	416	264	1232[3]
Aperture (mm)	76.2	75	80	56
Magnetic length (m)	6.1	8.8	9.45	14.3
Magnetic field (T)	4.3	5.3	3.5	8.3
Arc quadrupole magnets				
Number	216	256	276	386[3]
Aperture (mm)	88.9	75	80	56
Magnetic length[4] (m)	1.7	1.9	1.1	3.1
Gradient (T/m)	76	91.2	71	223
Commissioning	1983	1992	2000	2009

[1] Energy of the proton beam, colliding with the 27.5-GeV electron beam.
[2] Per unit of atomic mass.
[3] Twin-aperture magnets.
[4] Quadrupoles have several lengths.

rings to a maximum energy of 250 GeV per beam. Instead, the heavy-ion beams are accelerated to a maximum energy of 100 GeV per beam and unit of atomic mass. Each ring has a circumference of 3.8 km. The superconducting arc dipoles generate a maximum operating magnetic field of 3.5 T.

In 2009, the European Organization for Nuclear Research (CERN), near Geneva, completed the construction of the Large Hadron Collider (LHC) in the 27-km circumference LEP tunnel. As described in section 1.2.4, LHC is a proton/proton collider with a maximum energy of 7 TeV per beam. For a few months per year, LHC collides heavy-ion beams at higher energies than RHIC.

Table 1.2 summarizes the main features of the superconducting particle accelerators described above. Figure 1.8 shows the cross-sections (to scale) of

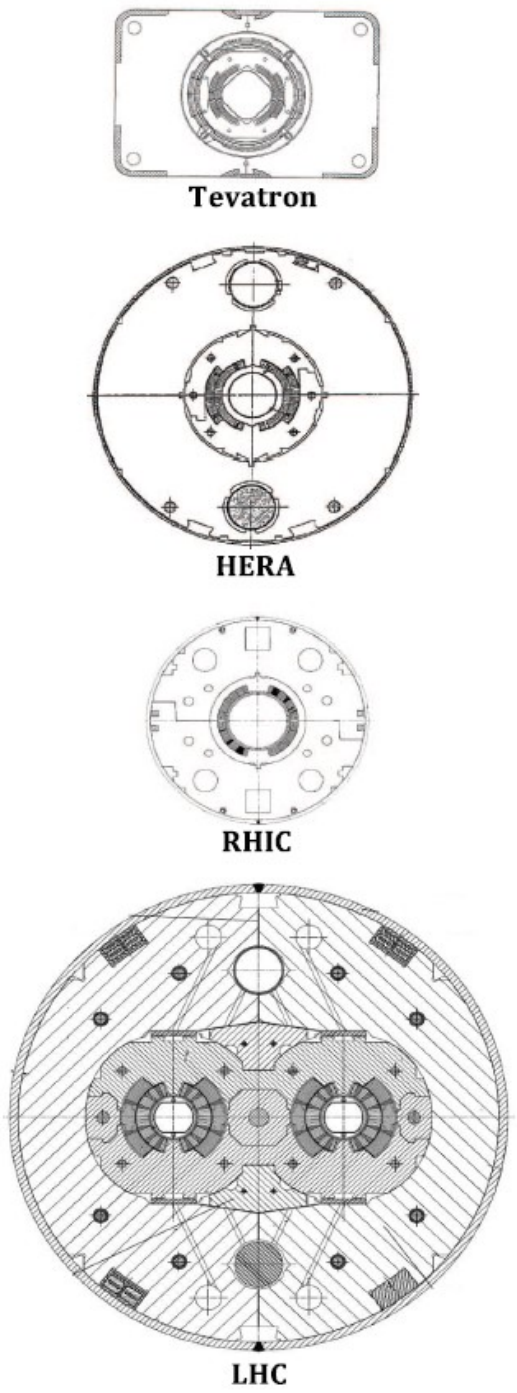

Figure 1.8: Cross-section (to scale) of the dipoles of the four major superconducting hadron accelerators built to date [30].

their arc dipole magnets. The field is produced by saddle shape coils that, in their long straight sections, approximate $\cos\theta$-type conductor distributions for dipole magnets and $\cos 2\theta$-type conductor distributions for quadrupole magnets (see section 2.4). The coils are wound by Rutherford-type cables, made up of NbTi multifilamentary strands, and are mechanically restrained by means of laminated *collars*. The collars apply a suitable compression (*pre-stress*) to the coil to avoid movements due to Lorentz forces, which would lead to heat generation, driving the conductor in the normal state. The coil in the collar can be pictured as a Roman arch, where the pre-compression is achieved by inserting an oversized wedge into the coil pole. The collars, assembled in halves around the coil and locked by keys, provide the radial load that translates into the required coil pre-compression. The collar-coil assembly is placed within an iron yoke providing a return path for the magnetic field.

In the case of the Tevatron, the collar-coil assembly is cold, while the iron yoke is warm. Starting with HERA, the iron yoke is included in the magnet cryostat and an outer shell delimiting the region of helium circulation completes the cold mass. In the case of LHC, the cold mass includes two collar-coil assemblies within a common iron yoke. The particle beams are circulated within a vacuum chamber inserted into the magnet coil apertures. The vacuum chamber, usually called *beam pipe*, is cooled by the helium bathing the magnet coil.

1.4.3 Next coming accelerators

As it has been pointed out in Ref. [34], LHC will remain the most powerful accelerator in the world for at least the next two decades. Its full exploitation is the highest priority of the European Strategy for Particle Physics. To extend its discovery potential and its operability by another decade, LHC will need a major upgrade in the 2020s to increase its luminosity (and thus collision rate) by a factor of five beyond its design value. The project goal is to raise the integrated luminosity by a factor of ten. As a highly complex machine, such an upgrade must be carefully studied. The necessary developments require about 10 years to prototype, test and realize new equipment. The novel machine configuration, the High Luminosity LHC (HL-LHC), will rely on several key innovative technologies representing exceptional technological challenges. These include among others: cutting-edge 11–12 T superconducting magnets, very compact superconducting cavities for beam rotation with ultra-precise phase control, a new technology for beam collimation and high-power superconducting links with almost zero energy dissipation.

In accelerator physics, the particle beam is assumed to have a Gaussian

shape in the transverse direction. The transverse size is described by the formula

$$\sigma\left(z\right) = \sqrt{\epsilon \cdot \beta\left(z\right)}\,, \tag{1.8}$$

where z is the position along the nominal beam trajectory, $\sigma(z)$ is the width of the Gaussian function, ϵ is the root mean square (RMS) geometrical beam emittance and $\beta(z)$ is a periodic function given by the overall focusing properties of the storage ring. It cannot be directly calculated by an analytical approach, but it has to be determined numerically [23].

The value of the β-function at the interaction point z_0 is referred to as β^*. The β-function is typically adjusted to have a local minimum at such point in order to minimize the beam size and thus maximize the interaction rate. Assuming that this point is in a drift space, one can show that the evolution of the β-function around the minimum point is given by

$$\beta\left(s\right) = \beta^* + \frac{s^2}{\beta^*}\,, \tag{1.9}$$

where $s = z - z_0$ is the distance along the nominal beam direction. Eq. (1.9) implies that the smaller the beam size at the interaction point, the faster the rise of the β-function (and thus the beam size) when going away from the interaction point. In practice, the aperture of the beam-line elements (e.g. focusing magnets) around the interaction point limits how small β^* can be made.

The instantaneous luminosity L can be expressed as a function of β^* by the formula

$$L = \gamma \frac{n_b N^2 f_{\text{rev}}}{4\pi\beta^*\epsilon_n} R\,, \qquad R = \left(\sqrt{1 + \frac{\theta_c \sigma_z}{2\sigma}}\right)^{-1}\,, \tag{1.10}$$

where γ is Lorentz's factor, n_b is the number of bunches per beam colliding at the interaction point, N is the bunch population, f_{rev} is the revolution frequency, ϵ_n is the transverse normalized emittance, R is a luminosity geometrical reduction factor from the crossing angle not including the Hourglass effect, θ_c is the full crossing angle between colliding beams and σ and σ_z are the transverse and longitudinal RMS sizes, respectively.

From Eq. (1.10), one can see that L and β^* are inversely proportional. To increase the luminosity we must decrease the factor $\beta^*\epsilon_n$. This needs the substitution of the magnets (see Fig. 1.9) before and after the interaction points of the ATLAS and CMS experiments.

The INFN section of Genova has the task to design the new recombination dipoles [31, 40, 46, 59] (called D2), which bend the two beams in opposite

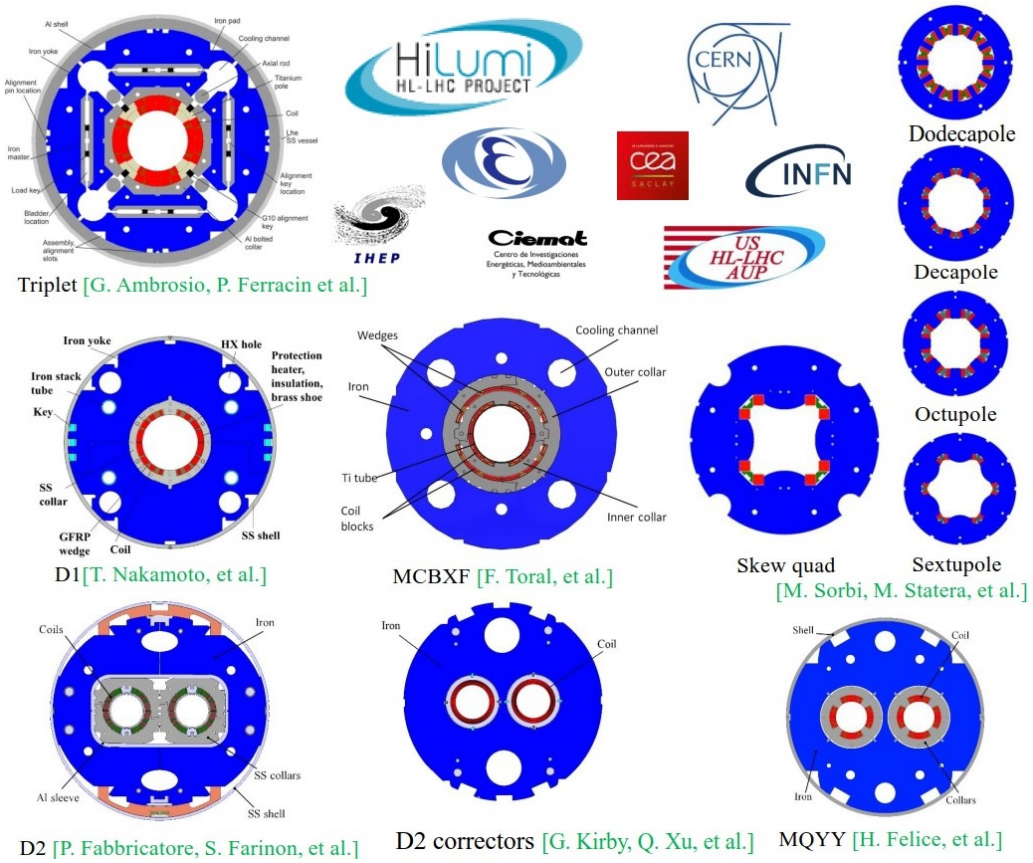

Figure 1.9: Cross-sections of the magnets that must be substituted for the High Luminosity upgrade of LHC [49].

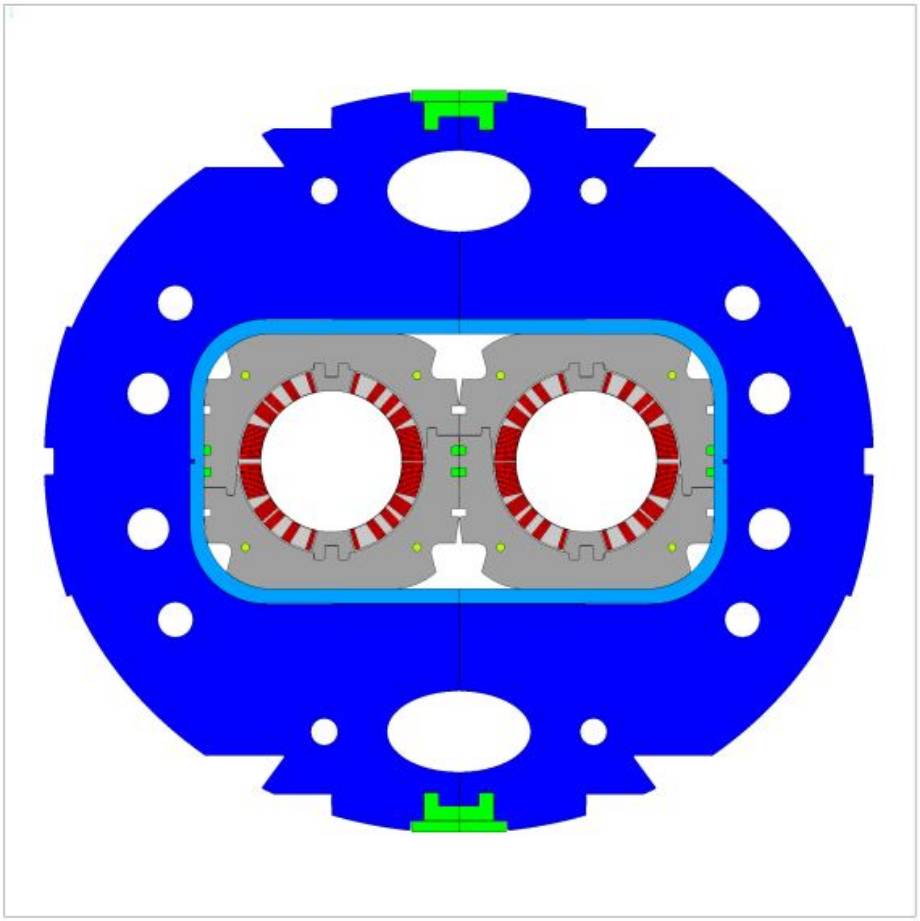

Figure 1.10: Cross-section of the D2 short model, which is under construction at ASG Superconductors in Genova. The main components are the conductors (in red), the copper wedges (in light grey), the stainless steel collars (in grey), the Al alloy sleeve (in light blue), the iron yoke (in blue), and stainless steel keys, pins and clamps (in green) [40].

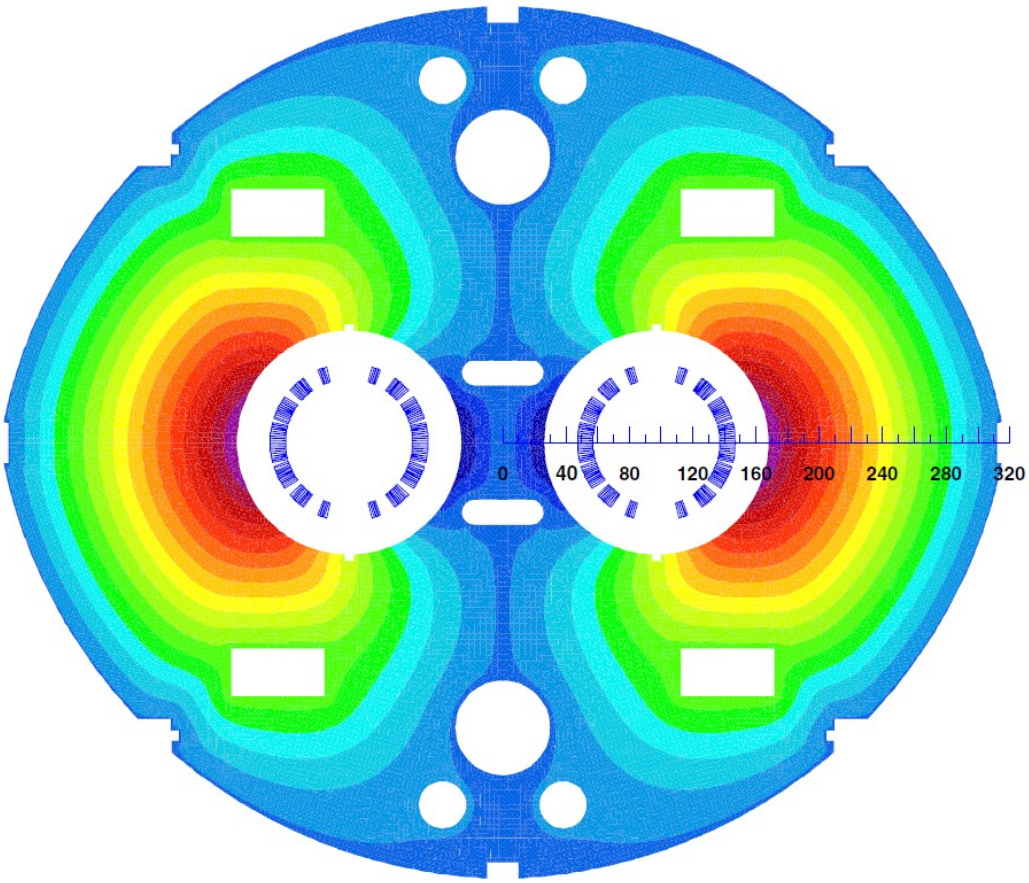

Figure 1.11: Cross-section of the LHC recombination dipoles [18]. The magnetic field has the same polarity in both apertures. The iron yoke between the bores is not saturated and magnetically decouples the coils.

directions (see Fig. 1.10). These magnets have a twin-aperture layout with a separation between the apertures of 188 mm and a bore diameter of 105 mm. They must generate an integrated magnetic field of 35 T/m with the same polarity in both apertures. The separation distance between the coils allows their magnetic coupling with a dramatic worsening of the field quality [1]. In the LHC recombination dipoles [8, 18] (see Fig. 1.11), this issue has been solved by interposing the iron yoke between the apertures. The magnetic field is low enough (2.77 T) for allowing the iron to magnetically decouple the two coils. This solution is not practicable in the new D2 design. Due to the length limitation, the HL-LHC dipole will have to generate a magnetic field of 4.5 T in each aperture. Because the field direction is identical in both apertures, the magnetic field between the coils sums up saturating the iron yoke, which contributes to get dramatically worse the field quality [22].

1.4.4 Far away accelerators

Around 2040, HL-LHC will complete its study program. Hence, new particle accelerators will be needed to explore unknown regions of High-Energy Physics (HEP). For this reason, the Future Circular Collider (FCC) study was launched [21] as a worldwide international collaboration under the auspices of the European Committee for Future Accelerators (ECFA).

Since its beginning, the FCC collaboration studied the physics opportunities, the technical challenges, the costs and the schedule of three circular colliders: an High-Energy update of LHC (HE-LHC), a new lepton collider (FCC-ee) and a new hadron collider (FCC-hh), which would be housed in 100-km circumference tunnel in the area of Geneva. Some of these accelerators could be part of an integrated program extending until the end of the 21st century. The results of these studies have been published in a Conceptual Design Report (CDR) [53–56] at the beginning of 2019, in time for the 2020 Update of the European Strategy for Particle Physics (EPPSU).

Between the three projects, the most difficult to achieve is the hadron collider, which will provide proton-proton collisions with 100-TeV energy in the center of mass, about seven times higher than in LHC. The collider will require 4668 arc dipole magnets and 744 arc quadrupole magnets in the twin-aperture layout, because the available space in the FCC tunnel does not allow two separate storage rings. For bending in the same direction the 50-TeV beams, the dipoles will have to generate a 16-T magnetic field with the same polarity in the two apertures of 50-mm diameter. For focusing these beams, the quadrupoles will have to generate a 367-T/m field gradient

[1] See section 2.3.

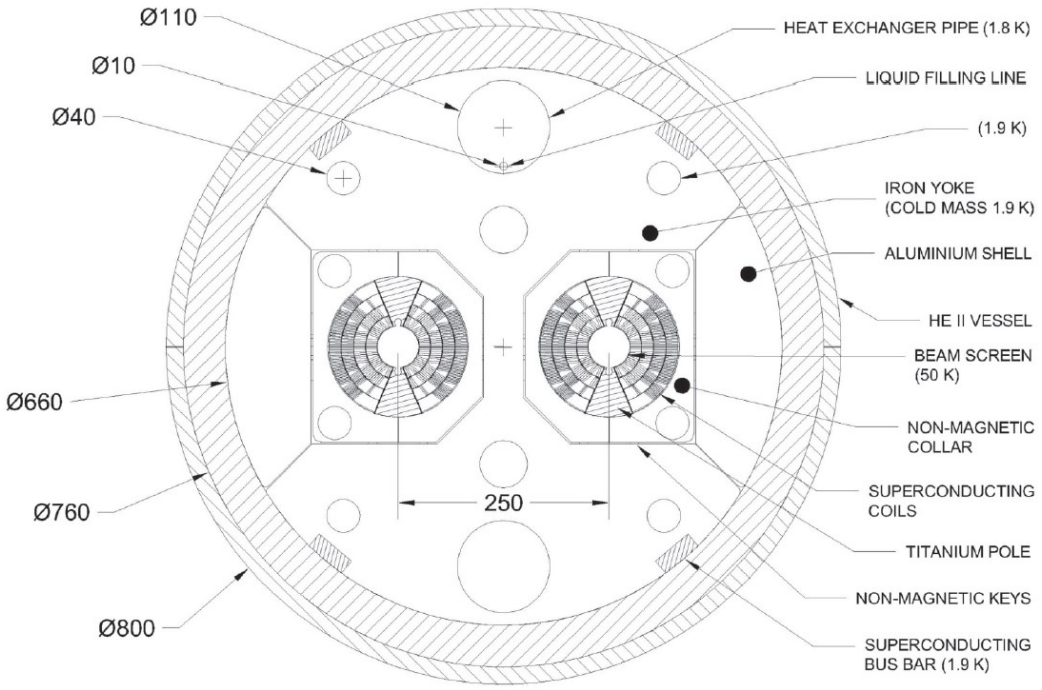

Figure 1.12: Cold mass cross-section of the 16-T arc dipole magnet [55].

in each aperture.

A research infrastructure of such a scale depends on the feasibility of key technologies, pushed beyond the current state of the art. The accelerator magnets require innovative designs to generate high-quality fields [2] up to 16 T. The cryogenic beam vacuum system must be designed to cope with unprecedented synchrotron light power. Therefore, with European Union support in the H2020 framework and under the umbrella of the FCC collaboration, the European Circular Collider (EuroCirCol) consortium was launched [28] to study the FCC-hh conceptual design.

Until now, all the superconducting accelerator magnets used a NbTi alloy, which has a critical field of about 15 T. So, a 10-T magnetic field in the beam pipe is considered to be the practical limit for this material. Nowadays, the intermetallic Nb_3Sn compound is the only functional material, which can generate a higher field with affordable costs on an industrial scale [67]. However, it is a brittle material, whose superconductivity may be reduced or destroyed from too high strains [3]. Therefore, the EuroCirCol collaboration studied different layouts for the 16-T bending dipole (arc dipole magnet) [41, 50, 66]. Block-coil, common-coil, $\cos\theta$ and canted-$\cos\theta$ designs have been

[2] See section 2.3.

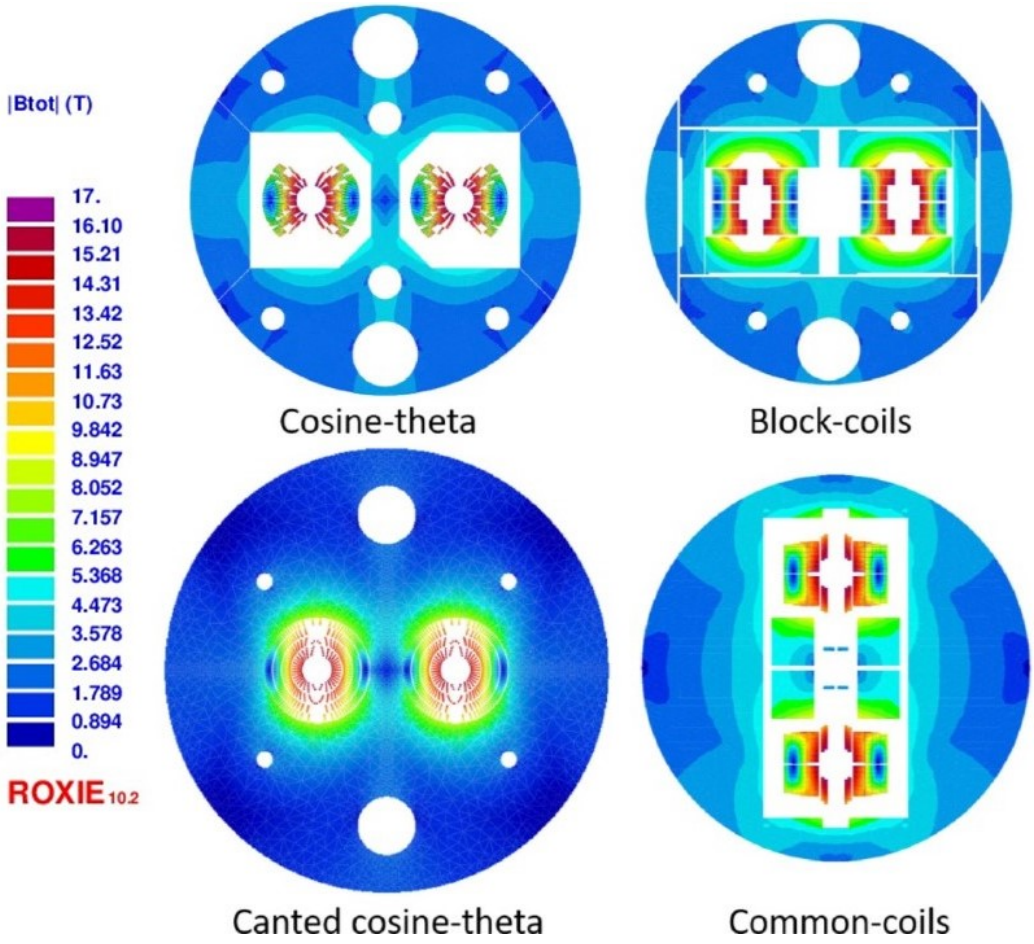

Figure 1.13: Electromagnetic cross-sections of the 16-T dipole design variants [56].

explored by four different teams (see Fig. 1.13) [35, 39, 42–44, 47, 48, 51, 61, 68, 69]. These studies led to choose as baseline design the $\cos\theta$ layout, designed by the INFN sections of Genoa and Milan (see cross-section sketch in Fig. 1.12 and details in chapter 4). It turned out to be the most efficient in terms of conductor amount. Compared to the $\cos\theta$ design, the block-coil requires 3.7%, the common-coil 25.4% and the CCT 27.7% more conductor. Minimizing the superconductor amount in the coils allows to significantly reduce the magnet costs, which are an important voice in the overall costs of the accelerator.

The FCC-hh superconducting magnets have been designed to be compatible with the LHC tunnel. So, they can be alternatively used for the High-Energy upgrade of LHC (HE-LHC). This would allow LHC to achieve a 27-TeV energy in the center of mass.

Chapter 2

Complex Formalism for the Magnetic Field

2.1 Introduction

The accelerator magnets must generate a high-homogeneous field. The general rule is that, in the power series expansion of the magnetic field, any higher-order multipole must be lower than 10^{-4} of the main component.

The complex formalism is an elegant way to compute two-dimensional fields in the magnet aperture. This was a standard method in the design process of the early superconducting magnets. For a long time, Beth's papers [1, 2] have been the main references for the magnet designers. Although numerical methods have widely replaced the complex analysis, the definition of the field quality is still based on this formalism [7, 18].

2.2 Complex magnetic field

2.2.1 Conductor model and problem symmetry

Let $(O, \boldsymbol{x}, \boldsymbol{y}, \boldsymbol{z})$ is the Cartesian coordinate system. Let us assume that the beam runs along the z-axis and is surrounded from a cylinder of indefinite radius, which represents the beam pipe. Let us consider a set of conductors parallel to the z-axis and uniform in z, located outside the cylinder. This case is representative of a coil assembly around the aperture of an accelerator magnet. Furthermore, let us assume that the conductors carry a constant current density, parallel to the z-axis and uniform in z. If we point out V_{cond}

the volume inside the conductors, we can write

$$\boldsymbol{J} = \begin{cases} J_z\,(x,y)\,\boldsymbol{z} & \forall\,(x,y,z) \in V_{\text{cond}}\,, \\ \boldsymbol{0} & \text{otherwise}\,. \end{cases} \tag{2.1}$$

Given the problem symmetry, the currents carried by the conductors produce a magnetic field $\boldsymbol{B}$ uniform in z. Hence, we can write

$$\boldsymbol{B} = B_x\,(x,y)\,\boldsymbol{x} + B_y\,(x,y)\,\boldsymbol{y} + B_z\,(x,y)\,\boldsymbol{z}\,. \tag{2.2}$$

According to Biot and Savart's law, the magnetic field $\boldsymbol{B}$ is perpendicular to the z-axis, and therefore

$$B_z\,(x,y) = 0 \qquad \forall\,(x,y)\ . \tag{2.3}$$

Given the two-dimensional problem symmetry, we work below in the plane $(O, \boldsymbol{x}, \boldsymbol{y})$ and designate by Σ_{cond} the cross-section of the conductors.

Making explicit Maxwell-Gauss's equation

$$\nabla \cdot \boldsymbol{B} = 0\,, \tag{2.4}$$

we get

$$\frac{\partial B_x\,(x,y)}{\partial x} + \frac{\partial B_y\,(x,y)}{\partial y} = 0 \qquad \forall\,(x,y)\ . \tag{2.5}$$

Instead, making explicit Maxwell-Ampere's equation

$$\nabla \times \boldsymbol{B} = \mu_0 \boldsymbol{J}\,, \tag{2.6}$$

where $\mu_0 = 4\pi \cdot 10^{-7}$ H/m, we obtain

$$\frac{\partial B_y\,(x,y)}{\partial x} - \frac{\partial B_x\,(x,y)}{\partial y} = \mu_0 J_z\,(x,y) \qquad \forall\,(x,y) \in \Sigma_{\text{cond}} \tag{2.7}$$

and

$$\frac{\partial B_y\,(x,y)}{\partial x} - \frac{\partial B_x\,(x,y)}{\partial y} = 0 \qquad \forall\,(x,y) \notin \Sigma_{\text{cond}}\,. \tag{2.8}$$

2.2.2 Magnetic field outside the conductors

Let us consider the region outside the conductors and let s is the complex variable defined as

$$s = x + iy\,. \tag{2.9}$$

Furthermore, let us define the complex magnetic field B as

$$B(s) = B_y(x,y) + iB_x(x,y) \qquad \forall s \notin \Sigma_{\text{cond}}\,. \tag{2.10}$$

The real and imaginary parts, $\mathrm{Re}(B)$ and $\mathrm{Im}(B)$, are simply

$$\mathrm{Re}(B) = B_y(x,y) \qquad \text{and} \qquad \mathrm{Im}(B) = B_x(x,y)\,. \tag{2.11}$$

The complex function B is continuous and single-valued. Now we demonstrate that it is holomorphic. This can be done by demonstrating that $\mathrm{Re}(B)$ and $\mathrm{Im}(B)$ satisfy Cauchy-Riemann's equations:

$$\frac{\partial \mathrm{Re}(B)}{\partial x} - \frac{\partial \mathrm{Im}(B)}{\partial y} = 0 \tag{2.12}$$

and

$$\frac{\partial \mathrm{Re}(B)}{\partial y} + \frac{\partial \mathrm{Im}(B)}{\partial x} = 0\,. \tag{2.13}$$

On one hand, we have

$$\frac{\partial \mathrm{Re}(B)}{\partial x} - \frac{\partial \mathrm{Im}(B)}{\partial y} = \frac{\partial B_y(x,y)}{\partial x} - \frac{\partial B_x(x,y)}{\partial y}\,, \tag{2.14}$$

which by combining with Eq. (2.8) yields Eq. (2.12).

On the other hand, we have

$$\frac{\partial \mathrm{Re}(B)}{\partial y} + \frac{\partial \mathrm{Im}(B)}{\partial x} = \frac{\partial B_y(x,y)}{\partial y} + \frac{\partial B_x(x,y)}{\partial x}\,, \tag{2.15}$$

which by combining with Eq. (2.5) yields Eq.(2.13).

From these results follows that the complex magnetic field B is single-valued and holomorphic on the region outside the conductors.

For deriving Cauchy-Riemann's equations from Maxwell's equations, the complex magnetic field must be defined as $B_y + iB_x$ or $B_x - iB_y$. Indeed, the function defined as $B_x + iB_y$ is not holomorphic.

2.2.3 Magnetic field inside the conductors

Let us now consider the region inside the conductors Σ_{cond} and let us assume that the z-component of the current density is uniform over Σ_{cond}:

$$J_z(x,y) = J_0 \qquad \forall\,(x,y) \in \Sigma_{\text{cond}}\,, \tag{2.16}$$

where J_0 is a constant.

Let us define the complex magnetic field B as

$$B(s) = B_y(x,y) + iB_x(x,y) - \frac{\mu_0 J_0}{2} s^* \qquad \forall (x,y) \in \Sigma_{\text{cond}}\,, \tag{2.17}$$

where s^* is the complex conjugate of s. This time, the real and imaginary parts, $\mathrm{Re}(B)$ and $\mathrm{Im}(B)$, are

$$\mathrm{Re}(B) = B_y(x,y) - \frac{\mu_0 J_0}{2} x \tag{2.18}$$

and

$$\mathrm{Im}(B) = B_x(x,y) + \frac{\mu_0 J_0}{2} y\,. \tag{2.19}$$

The complex function B is continuous and single-valued. Now we show that it is holomorphic over Σ_{cond} by demonstrating that $\mathrm{Re}(B)$ and $\mathrm{Im}(B)$ satisfy Cauchy-Riemann's equations (2.12) and (2.13). On one hand, we have

$$\frac{\partial \mathrm{Re}(B)}{\partial x} - \frac{\partial \mathrm{Im}(B)}{\partial y} = \frac{\partial B_y(x,y)}{\partial x} - \frac{\partial B_x(x,y)}{\partial y} - \mu_0 J_0\,, \tag{2.20}$$

which by combining with Eq. (2.7) and Eq. (2.16) yields Eq. (2.12). On the other hand, we have

$$\frac{\partial \mathrm{Re}(B)}{\partial y} + \frac{\partial \mathrm{Im}(B)}{\partial x} = \frac{\partial B_y(x,y)}{\partial y} + \frac{\partial B_x(x,y)}{\partial x}\,, \tag{2.21}$$

which by combining with Eq. (2.5) yields Eq. (2.13).

From these results follows that the complex magnetic field B is single-valued and holomorphic over Σ_{cond}.

2.3 Multipole expansion

Let $(O, \boldsymbol{x}, \boldsymbol{y}, \boldsymbol{z})$ designate a Cartesian coordinate system and let us consider a current line of intensity I, parallel to z-axis and crossing the plane $(O, \boldsymbol{x}, \boldsymbol{y})$ at the position $s_0 \equiv x_0 + iy_0$, as represented in Fig. 2.1.

As we showed in the previous section, Biot and Savart's law set that the current line I generates a magnetic field $\boldsymbol{B}$ parallel to the plane $(O, \boldsymbol{x}, \boldsymbol{y})$ and independent from the variable z. Its module can be represented by the complex function $B(s)$, defined by Eq. (2.10) and explicitly expressed according to Biot and Savart's law, as

$$B(s) = \frac{\mu_0 I}{2\pi (s - s_0)} \qquad \text{for } s \neq s_0\,. \tag{2.22}$$

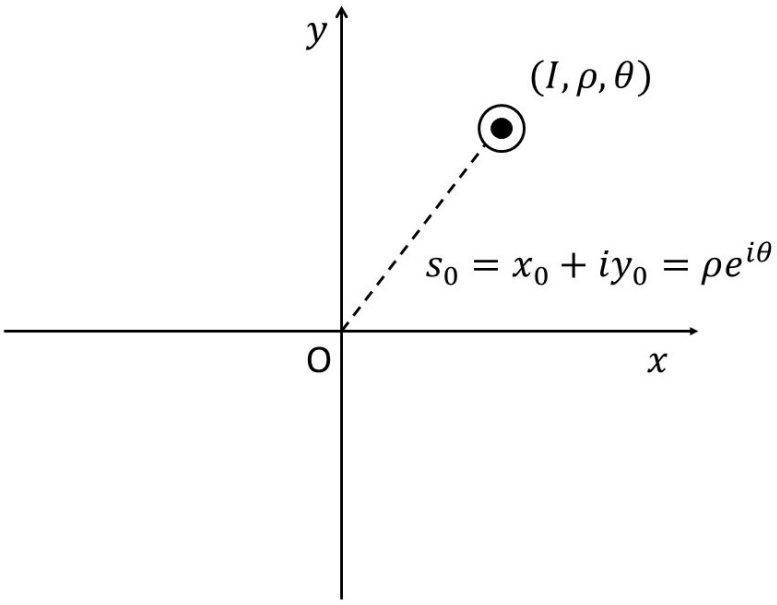

Figure 2.1: Current line of intensity I at the position s_0 in the complex plane. The versus of the current line is outgoing from the page.

Because $B(s)$ is holomorphic, it can be expanded in a power series. Knowing that for $s < 1$

$$\frac{1}{1-s} = 1 + s + s^2 + s^3 + \cdots = \sum_{n=1}^{\infty} s^{n-1}\,, \tag{2.23}$$

we can develop the multipolar expansion of the magnetic field for $s < s_0$, as

$$\begin{aligned} B\,(s) &= \frac{\mu_0 I}{2\pi\,(s - s_0)} = -\frac{\mu_0 I}{2\pi s_0}\frac{1}{1 - s/s_0} \\ &= -\frac{\mu_0 I}{2\pi s_0}\sum_{n=1}^{\infty}\left(\frac{s}{s_0}\right)^{n-1} \\ &= -\frac{\mu_0 I}{2\pi s_0}\sum_{n=1}^{\infty}\left(\frac{R_{ref}}{s_0}\right)^{n-1}\left(\frac{s}{R_{ref}}\right)^{n-1}\,, \end{aligned} \tag{2.24}$$

where R_{ref} is a *reference radius*. It is just introduced to avoid coefficients with the physical dimensions depending over the order of the multipoles. It does not have any physical meaning and it has nothing to do with the convergence radius of the series.

We can re-write the multipolar expansion in the European notation as

$$B\left(x,y\right)=B_{y}\left(x,y\right)+iB_{x}\left(x,y\right)=\sum_{n=1}^{\infty}\left(B_{n}+iA_{n}\right)\left(\frac{x+iy}{R_{ref}}\right)^{n-1}\,, \quad (2.25)$$

where

$$B_{n}+iA_{n}=-\frac{\mu_{0}I}{2\pi s_{0}}\left(\frac{R_{ref}}{s_{0}}\right)^{n-1}=-\frac{\mu_{0}I}{2\pi R_{ref}}\left(\frac{R_{ref}}{s_{0}}\right)^{n}\,. \quad (2.26)$$

The coefficients A_n and B_n have the dimensions of the magnetic field (T) and they are called *skew and normal cylindrical harmonics*, respectively. In the European definition (2.25), each term of order n represents the $2n$-pole component.

Eq. (2.26) shows that, except for $n = 1$, the cylindrical harmonics depend on the reference radius and that their values change according to the scaling law

$$B_{n}^{'}+iA_{n}^{'}=\left(\frac{R_{\mathrm{ref}}^{'}}{R_{\mathrm{ref}}}\right)^{n-1}\left(B_{n}+iA_{n}\right)\,, \quad (2.27)$$

where $B_n^{'}$ and $A_n^{'}$ are the coefficients at a reference radius $R_{\mathrm{ref}}^{'}$ and B_n and A_n are the coefficients at a different reference radius R_{ref}.

The choice of the reference radius has evolved in the time [7]. It was 12.7 mm for the Tevatron magnets, which had a 38.1-mm aperture radius. It was 12.5 mm for the HERA magnets, which had a 37.5-mm aperture radius. In those days, the general rule for R_{ref} was to take 1/3 of the aperture radius. Today, the reference radius for an accelerator magnet is usually chosen as 2/3 of the aperture radius.

The cylindrical harmonics can be dimensionless and normalized to units as

$$b_{n}=10^{4}\frac{B_{n}}{B_{\mathrm{ref}}}\qquad\text{and}\qquad a_{n}=10^{4}\frac{A_{n}}{B_{\mathrm{ref}}}\,, \quad (2.28)$$

where B_{ref} is the *main field component* at the reference radius R_{ref}. Thus, Eq. (2.25) becomes

$$\begin{aligned}B\left(x,y\right)&=B_{y}\left(x,y\right)+iB_{x}\left(x,y\right)\\&=10^{-4}B_{\mathrm{ref}}\sum_{n=1}^{\infty}\left(b_{n}+ia_{n}\right)\left(\frac{x+iy}{R_{ref}}\right)^{n-1}\,,\end{aligned} \quad (2.29)$$

where a_n and b_n are called *normalized* skew and normal cylindrical harmonics, respectively.

The representation of the magnetic field by a power series expansion is very useful for computing the beam orbits in the accelerator physics. As a consequence, the field quality requirements, for the accelerator magnets, are usually formulated as tolerances on the various terms of the power series expansion of the magnetic field. An important aspect in the accelerator magnet design is to find the conductor arrangements, which minimize the coefficients of the power series expansion in the magnet aperture. Typical acceptable field quality deviations from the ideal field are of the order of 0.01% at 2/3 of the reference radius. This is why the factor 10^{-4} is factored in Eq. (2.29). In this way the normalized harmonics have values of the order of the unity and the exponential notation can be avoided.

2.4 Sector model

Let us consider Fig. 2.1 again. From Eq. (2.26) follows that the cylindrical harmonics generated by the current line I are

$$\begin{aligned} B_n + iA_n &= -\frac{\mu_0 I}{2\pi R_{\text{ref}}} \left(\frac{R_{\text{ref}}}{s_0}\right)^n \\ &= -\frac{\mu_0 I}{2\pi R_{\text{ref}}} \left(\frac{R_{ref}}{\rho}\right)^n e^{-in\theta} \\ &= -\frac{\mu_0 I}{2\pi R_{\text{ref}}} \left(\frac{R_{ref}}{\rho}\right)^n (\cos n\theta - i \sin n\theta) \ . \end{aligned} \tag{2.30}$$

Now let us consider the quadruplet of current lines $(I, \rho, \theta), (-I, \rho, \pi - \theta), (-I, \rho, \pi + \theta)$ and $(I, \rho, -\theta)$ shown in Fig. 2.2. The magnetic field generated by this quadruplet is the sum of the contributions of each current line. Within the circle of center O and radius ρ, the field $B(s)$ can be calculated for $s < \rho$ by Eq. (2.25), where

$$\begin{aligned} B_n + iA_n = &-\frac{\mu_0 I}{2\pi R_{ref}} \left(\frac{R_{ref}}{\rho}\right)^n \\ &\times \left[e^{-in\theta} - e^{-in(\pi-\theta)} - e^{-in(\pi+\theta)} + e^{in\theta}\right] \ . \end{aligned} \tag{2.31}$$

Knowing that

$$\begin{aligned} \cos n\,(\pi - \theta) &= (-1)^n \cos n\theta \,, \\ \cos n\,(\pi + \theta) &= (-1)^n \cos n\theta \end{aligned} \tag{2.32}$$

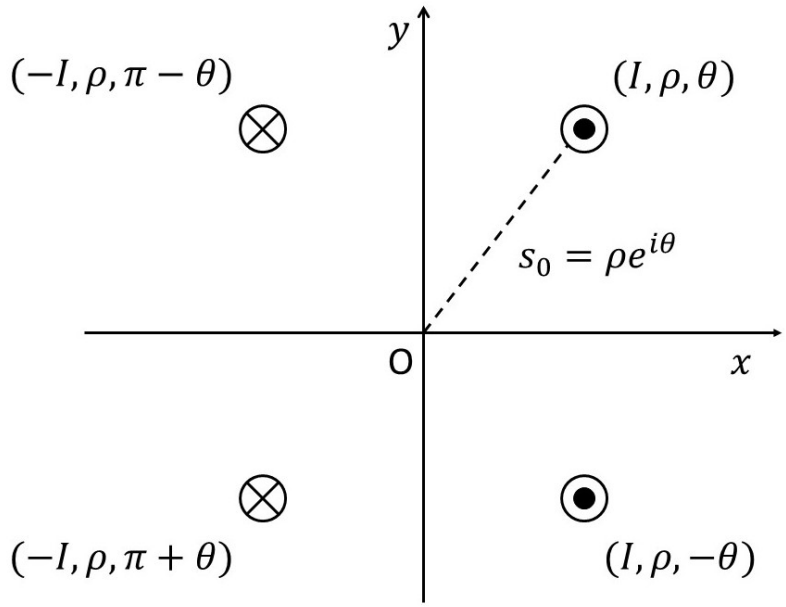

Figure 2.2: Quadruplet of current lines with an even symmetry about the x-axis and an odd symmetry about the y-axis.

and similarly

$$\begin{aligned} \sin n\,(\pi - \theta) &= -\,(-1)^n \sin n\theta\,, \\ \sin n\,(\pi + \theta) &= (-1)^n \sin n\theta\,, \end{aligned} \tag{2.33}$$

we get

$$e^{-in\theta} - e^{-in(\pi-\theta)} - e^{-in(\pi+\theta)} + e^{in\theta} = 2\,[1 - (-1)^n] \cos n\theta\,, \tag{2.34}$$

which is only non-zero when n is odd. Therefore, the complex magnetic field can be written for $s < \rho$ with the only non-zero coefficients

$$B_n = -\frac{2\mu_0 I}{\pi R_{ref}} \left(\frac{R_{ref}}{\rho}\right)^n \cos n\theta \quad n \text{ odd}\,, \tag{2.35}$$

which are called *allowed* cylindrical harmonics of this current distribution. The even symmetry about the x-axis deletes the skew harmonics and the odd symmetry about the y-axis drops the even normal harmonics.

Let us consider a dipole, whose quarter coil layout is a sector of width w and bending radius R, spanning the angle from 0 to ϕ. The layout is symmetric both about the x-axis and about the y-axis. A uniform current density J flows in the right half coil and $-J$ in the left (see Fig. 2.3). The

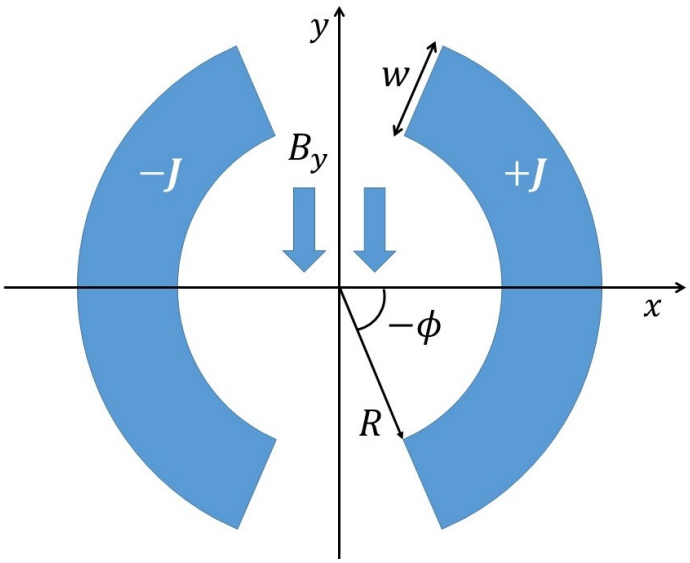

Figure 2.3: Sector coil layout for a dipole of inner radius R and coil width w, spanning the angle from 0 to ϕ. The layout is symmetric both about the x-axis and about the y-axis. A uniform current density J flows in the right half coil and $-J$ in the left. The magnetic field for $r < R$ has the component B_y only.

allowed harmonics can be obtained by integrating the current in Eq. (2.35) over the sector ($I \to J\rho\, d\rho\, d\theta$):

$$B_n = \frac{2\mu_0 J R_{ref}^{n-1}}{\pi n\,(n-2)} \left(\frac{1}{(R+w)^{n-2}} - \frac{1}{R^{n-2}} \right) \sin n\phi\,. \tag{2.36}$$

Solving Eq. (2.36) we find that the first allowed harmonics B_3 vanishes for $\phi = 60°$ and the second allowed harmonics B_5 for $\phi = 36°$ and for $\phi = 72°$. Therefore, we cannot have $B_3 = B_5 = 0$ with a single sector.

If we consider a coil composed by two sectors $[0, \phi_1]$ and $[\phi_2, \phi_3]$, with a wedge between ϕ_1 and ϕ_2 (see Fig. 2.4), we can set $B_3 = B_5 = B_7 = 0$ by numerically solving the equation system

$$\begin{aligned} \sin(7\phi_3) - \sin(7\phi_2) + \sin(7\phi_1) &= 0\,, \\ \sin(5\phi_3) - \sin(5\phi_2) + \sin(5\phi_1) &= 0\,, \\ \sin(3\phi_3) - \sin(3\phi_2) + \sin(3\phi_1) &= 0\,, \end{aligned} \tag{2.37}$$

which gives the solution $(0° - 43.2°, 52.2° - 67.3°)$. Putting a second wedge in the coil, we add two free parameters and we can set to zero from b_3 to b_{11},

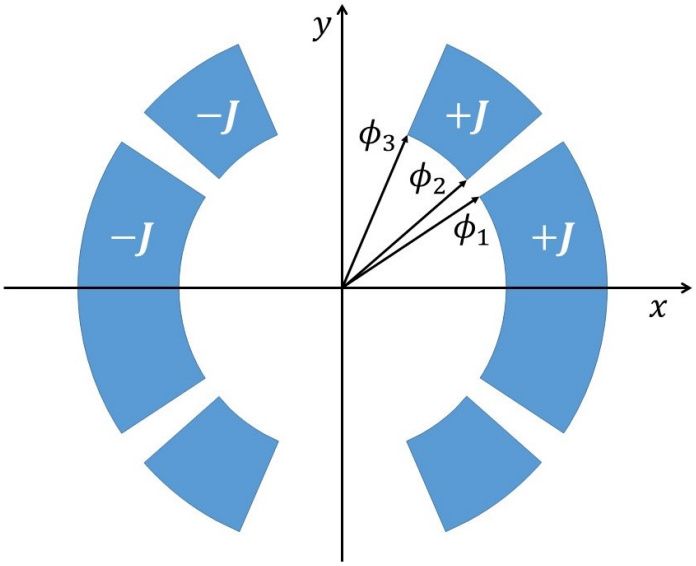

Figure 2.4: Sector coil layout with a dipole symmetry and an angular wedge.

by resolving the new equation system

$$\begin{aligned}
&\sin(11\phi_5) - \sin(11\phi_4) + \sin(11\phi_3) - \sin(11\phi_2) + \sin(11\phi_1) = 0\,,\\
&\sin(9\phi_5) - \sin(9\phi_4) + \sin(9\phi_3) - \sin(9\phi_2) + \sin(9\phi_1) = 0\,,\\
&\sin(7\phi_5) - \sin(7\phi_4) + \sin(7\phi_3) - \sin(7\phi_2) + \sin(7\phi_1) = 0\,,\\
&\sin(5\phi_5) - \sin(5\phi_4) + \sin(5\phi_3) - \sin(5\phi_2) + \sin(5\phi_1) = 0\,,\\
&\sin(3\phi_5) - \sin(3\phi_4) + \sin(3\phi_3) - \sin(3\phi_2) + \sin(3\phi_1) = 0\,,
\end{aligned} \tag{2.38}$$

which gives the solution $(0° - 33.3°, 37.1° - 53.1°, 63.4° - 71.8°)$.

Theoretically, P wedges allow setting to zero up to $(2P + 1)$ allowed harmonics. The wedges introduce a geometric spacing in the current distribution, which imitates with a good approximation the ideal $\cos\theta$ annulus, i.e., an annulus crossed from a current density proportional to the cosine of the azimuth. It has been demonstrated that this arrangement produces a pure dipole magnetic field in its aperture. The coils based on this geometry are called $\cos\theta$ *coils*. All the superconducting accelerators described in section 1.4.2 used $\cos\theta$ dipole magnets and $\cos 2\theta$ quadrupole magnets.

2.5 Integrated multipoles

The overall effect of the multipoles on the particle trajectory is described by the cylindrical harmonics integrated over the magnet length (*integrated harmonics*).

Let $(O, \boldsymbol{x}, \boldsymbol{y}, \boldsymbol{z})$ designate a Cartesian coordinate system and let z-axis be the magnet axis. Formally, the *3D main field component* is defined as the average of the 2D main field component, B_{ref}, on the straight part of the magnet:

$$\bar{B}_{\text{ref}} \equiv \frac{\int_{\text{s.p.}} B_{\text{ref}}(z)\, dz}{\int_{\text{s.p.}} dz}\,. \tag{2.39}$$

The *magnetic length* or *effective length*, L_m, of the magnet is defined as the length of an equivalent magnet without the coil ends and with the same 3D main field component:

$$L_{\text{mag}} \equiv \frac{\int_{-\infty}^{\infty} B_{\text{ref}}(z)\, dz}{\bar{B}_{\text{ref}}}\,. \tag{2.40}$$

The magnetic length is an important parameter in the magnet design. The magnet length is always given in terms of magnetic length.

Knowing that, for the accelerator magnets, $\bar{B}_{\text{ref}} = B_{\text{ref}}$, the integrated harmonics are defined as

$$\bar{b}_n \equiv \frac{\int_{-\infty}^{\infty} B_n(z)\, dz}{\int_{-\infty}^{\infty} B_{\text{ref}}(z)\, dz} = \frac{\int_{-\infty}^{\infty} B_n(z)\, dz}{L_{\text{mag}} B_{\text{ref}}} = \frac{\int_{-\infty}^{\infty} b_n(z)\, dz}{L_{\text{mag}}} \tag{2.41}$$

and

$$\bar{a}_n \equiv \frac{\int_{-\infty}^{\infty} A_n(z)\, dz}{\int_{-\infty}^{\infty} B_{\text{ref}}(z)\, dz} = \frac{\int_{-\infty}^{\infty} A_n(z)\, dz}{L_{\text{mag}} B_{\text{ref}}} = \frac{\int_{-\infty}^{\infty} a_n(z)\, dz}{L_{\text{mag}}}\,. \tag{2.42}$$

Then, the integrated harmonics can be computed by integrating the $b_n(z)$ and $a_n(z)$ harmonics along the z-axis and dividing by L_{mag}.

Chapter 3

Extended Sector Model

3.1 Introduction

The first step in the coil design is to find the block arrangements, which generate a high-homogeneous magnetic field, given the bending radius, the cable width, the layer number and the inter-beam distance. These configurations cannot be derived explicitly and many numerical algorithms exist to find the optimal cross-sections [18]. Owing to the complicated magnet geometry (coils made of blocks, blocks made of cables and cables made of strands), they are time-consuming and, to be really effective, they have to operate on configurations which are not too far from a local optimum.

In the single-aperture layout, the sector model, approximating the blocks as annular sectors, is a powerful analytical tool, which allows to carry out an initial scan on a very large number of possible configurations [16, 25, 60]. This makes easier to find the cross-section which best suits the specifications.

The twin-aperture layout introduces a complicating factor: the contribution to the harmonic components which one coil exerts on the other aperture. This effect is referred to as *cross-talk*. If it is not negligible, an extension of the single-aperture sector model is required to analytically scan the parameter space. This is the case of the recombination dipole D2 for the High Luminosity upgrade of LHC (HL-LHC) and the 16-T bending dipole for the Future Circular Collider (FCC).

The FCC bending dipole presents two further issues. On one hand, the small keystoning of the conductors brings to non-negligible geometrical differences between real blocks and radial sectors. This gap leads to non-negligible errors in the computation of the coil harmonics[1] (*geometric harmonics*), which could cause the optimization process to fail. On the other hand, the

[1] Up to 100 units on b_3 in the first layer.

minimal distance between neighboring blocks makes difficult to consider the harmonic contribution generated by the iron saturation (*saturation harmonics*) only in the next phase of the design process. Indeed, fine-tuning the block positions to correct the too high geometrical and saturation harmonics could lead to too small wedges.

For solving the previous issues, we developed an extension of the sector model [64], which we used to find the asymmetric coil configurations, that minimize the cross-talk in the new dipole D2 of HL-LHC and the 16-T bending dipole of FCC. In a computational time of few minutes for D2 and few tens of minutes for the FCC dipole, this method allowed to find magnetic designs better than those found with the standard techniques [18] (see sections 4.4 and 5.2.2). These results show that this method can be used as an optimal tool at the early stage of the coil design of a twin-aperture dipole, which presents a non-negligible cross-talk.

3.2 Theoretical model

3.2.1 Asymmetric layout

Compared to the single-aperture layout described in Section 2.4, the magnetic cross-talk can bring to non-zero normal multipole coefficients also for even orders. To control the even normal harmonics we must break the symmetry of the current lines about the y-axis.

Let us consider a quadruplet of current lines, which is symmetric only about the x-axis (see Fig. 3.1). The normal multipoles can be written as

$$\begin{aligned} B_n = &- \frac{\mu_0 I}{\pi R_{ref}} \left(\frac{R_{ref}}{\rho}\right)^n \cos n\theta_1 \\ &- \frac{\mu_0 (-I)}{2\pi R_{ref}} \left(\frac{R_{ref}}{\rho}\right)^n \cos n(\pi - \theta_2) \\ &- \frac{\mu_0 (-I)}{2\pi R_{ref}} \left(\frac{R_{ref}}{\rho}\right)^n \cos n(\pi + \theta_2) \ . \end{aligned} \tag{3.1}$$

Owing to Eq. (2.32), Eq. (3.1) becomes

$$B_n = -\frac{\mu_0 I}{\pi R_{ref}} \left(\frac{R_{ref}}{\rho}\right)^n \left[\cos n\theta_1 - (-1)^n \cos n\theta_2\right] . \tag{3.2}$$

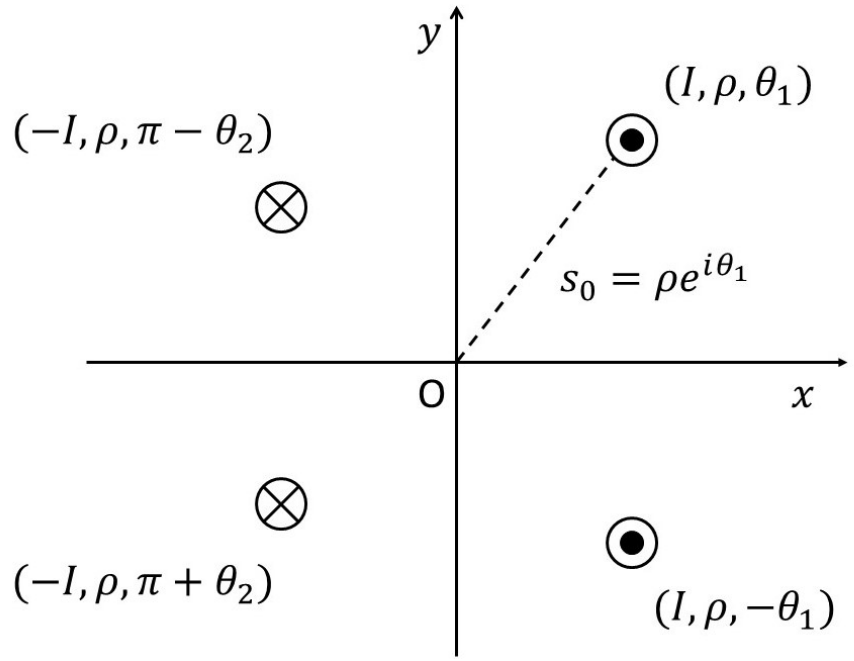

Figure 3.1: Asymmetric quadruplet of current lines about the y-axis and with an even symmetry about the x-axis.

Integrating the current for passing to an asymmetric sector coil about the y-axis (see Fig. 3.2), we obtain

$$\begin{aligned} B_n = &-\frac{\mu_0 J R_{ref}^{n-1}}{\pi} \int_R^{R+w} \frac{1}{\rho^{n-1}} d\rho \\ &\times \left(\int_\phi^{\phi'} \cos n\theta_1 d\theta_1 - (-1)^n \int_\psi^{\psi'} \cos n\theta_2 d\theta_2 \right) , \end{aligned} \tag{3.3}$$

where R is the bending radius, w is the coil width, ϕ and ϕ' are the starting and final angles respectively for the right sector and ψ and ψ' are the starting and final angles respectively for the left sector. For $n \neq 2$ we get

$$\begin{aligned} B_n = &\frac{\mu_0 J R_{ref}^{n-1}}{\pi n\,(n-2)} \left(\frac{1}{(R+w)^{n-2}} - \frac{1}{R^{n-2}} \right) \\ &\times \left[\sin n\phi' - \sin n\phi - (-1)^n \left(\sin n\psi' - \sin n\psi \right) \right] , \end{aligned} \tag{3.4}$$

and for $n = 2$

$$B_2 = \frac{\mu_0 J R_{ref}}{2\pi} \ln \frac{R}{R+w} \left(\sin 2\phi' - \sin 2\phi - \sin 2\psi' + \sin 2\psi \right) . \tag{3.5}$$

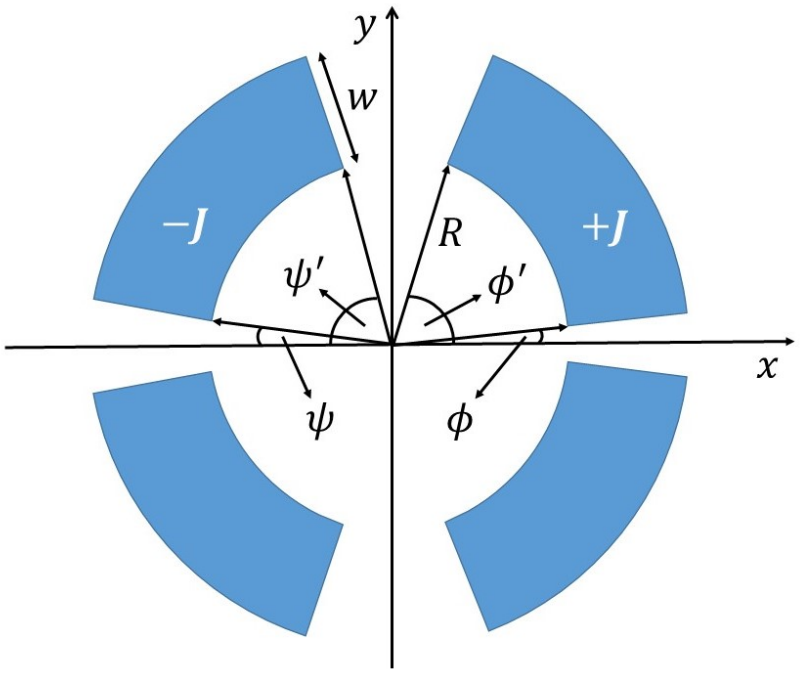

Figure 3.2: Asymmetric sector coil about the y-axis and symmetric about the x-axis. ϕ and $\phi^{'}$ are the starting and final angles of the right sector respectively. ψ and $\psi^{'}$ are the starting and final angles of the left sector respectively. All sectors have the bending radius R and the width w.

3.2.2 Cable modeling

For solving the conductor issue with a small keystoning, we include the cable in the sector model. We define the final angles of the sectors as

$$\begin{aligned} \phi^{'} &= \phi + m\,\Delta\phi\,, \\ \psi^{'} &= \psi + m\,\Delta\phi\,, \end{aligned} \tag{3.6}$$

where m is the number of turns of each sector and $\Delta\phi$ is the angle underlying the turn (see Fig. 3.3). The angle $\Delta\phi$ is calculated as

$$\Delta\phi = \arcsin\frac{\bar{l}}{\bar{R}}\,, \tag{3.7}$$

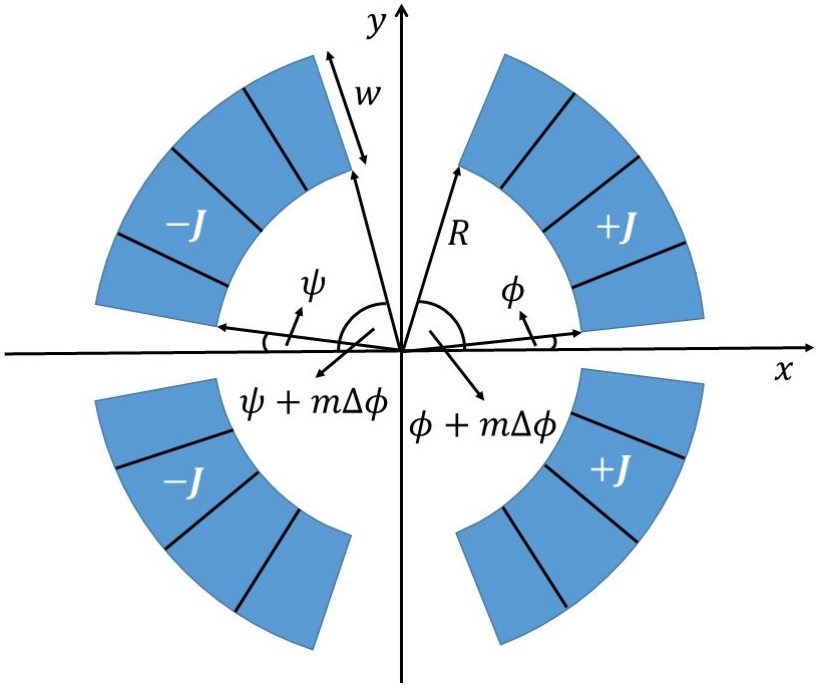

Figure 3.3: Asymmetric sector coil about the y-axis and symmetric about the x-axis. ϕ and ψ are the starting angles of the right and left sectors respectively. Both sectors have the bending radius R and the width w. They are composed from m turns and $\Delta\phi$ is the angle underlying each turn.

where $\bar{l}$ is the mean cable thickness, considered as conductor plus insulation, and $\bar{R}$ is the mean bending radius of the cable, computed as

$$\bar{R} = R + \frac{w}{2}\,. \tag{3.8}$$

The choice to work with the mean cable thickness on the mean bending radius leads to geometric differences of opposite sign between real blocks and radial sectors (see Fig. 3.4 for the dipole D2, Fig. 3.5 and Fig. 3.6 for the FCC bending dipole). These geometrical differences bring to errors of opposite sign in the harmonic computation. The opposite sign errors partially offset each other and minimize the overall harmonic error. The maximum error on the most sensible harmonic becomes $\Delta b_3 < 19$ units in the 16-T bending dipole and $\Delta b_3 < 11$ units in the dipole D2.

The equations (3.4) and (3.5) are rewritten as

$$B_n = \frac{\mu_0 J R_{ref}^{n-1}}{\pi n\,(n-2)} \left(\frac{1}{(R+w)^{n-2}} - \frac{1}{R^{n-2}} \right) \times \left[\sin n\,(\phi + m\,\Delta\phi) - \sin n\phi - (-1)^n \left(\sin n\,(\psi + m\,\Delta\phi) - \sin n\psi \right) \right] \tag{3.9}$$

and

$$B_2 = \frac{\mu_0 J R_{ref}}{2\pi} \ln \frac{R}{R+w} \times \left[\sin 2\,(\phi + m\,\Delta\phi) - \sin 2\phi - \sin 2\,(\psi + m\,\Delta\phi) + \sin 2\psi \right]. \tag{3.10}$$

In the twin-aperture layout, Eq. (3.9) and Eq. (3.10) are the harmonics generated from the right coil in its aperture and, hereafter, we will indicate them as B_n^r.

3.2.3 Cross-talk: sector model

Let us consider a quadruplet of current lines $(-I, \rho, \theta_1), (I, \rho, \pi - \theta_2), (I, \rho, \pi + \theta_2)$ and $(-I, \rho, -\theta_1)$, as reported in Fig. 3.7. The polar coordinates of the quadruplet are in the coordinate system centered in O'. The quadruplet is symmetric about the x-axis and asymmetric about its vertical axis. The positions of the current lines in the complex plane centered in O are

$$\begin{aligned} s_1 &= -2d + \rho\, e^{i\theta_1}\,, & s_2 &= -2d + \rho\, e^{i(\pi-\theta_2)}\,, \\ s_3 &= -2d + \rho\, e^{i(\pi+\theta_2)}\,, & s_4 &= -2d + \rho\, e^{-i\theta_1}\,, \end{aligned} \tag{3.11}$$

where d is half of the inter-beam distance.

The multipoles generated on the reference radius follow from Eq. (2.26):

$$\begin{aligned} B_n + iA_n &= -\frac{\mu_0 I R_{\text{ref}}^{n-1}}{2\pi} \left(\frac{1}{s_1^n} + \frac{1}{s_4^n} \right) - \frac{\mu_0\,(-I)\,R_{\text{ref}}^{n-1}}{2\pi} \left(\frac{1}{s_2^n} + \frac{1}{s_3^n} \right) \\ &= -\frac{\mu_0 I R_{\text{ref}}^{n-1}}{2\pi} \left[\frac{1}{(-2d + \rho\, e^{i\theta_1})^n} + \frac{1}{(-2d + \rho\, e^{-i\theta_1})^n} \right] \\ &\quad - \frac{\mu_0\,(-I)\,R_{\text{ref}}^{n-1}}{2\pi} \left[\frac{1}{(-2d + \rho\, e^{i(\pi-\theta_2)})^n} + \frac{1}{(-2d + \rho\, e^{i(\pi+\theta_2)})^n} \right]. \end{aligned} \tag{3.12}$$

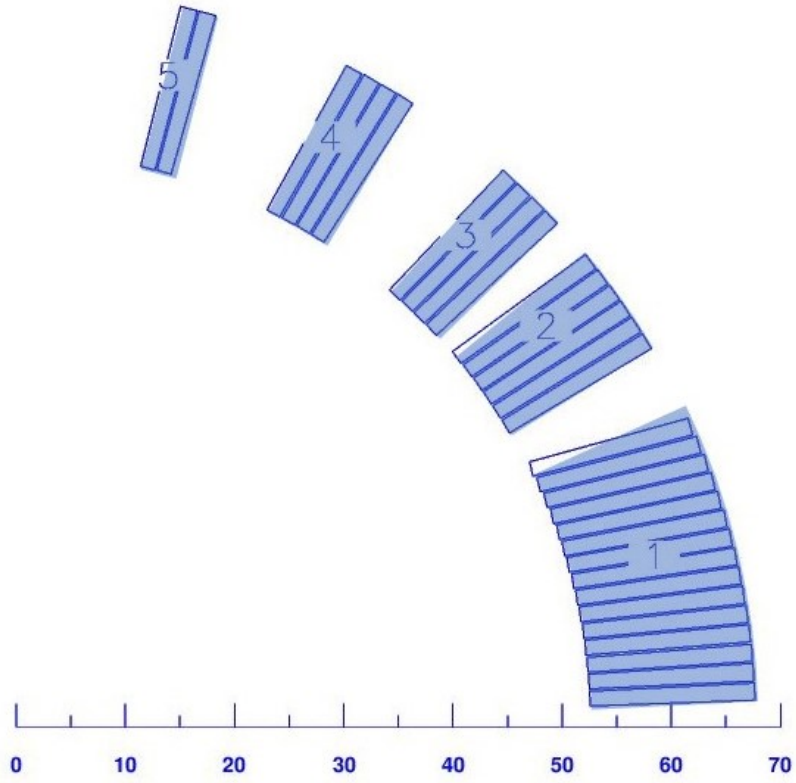

Figure 3.4: Drawing of a coil quarter of the dipole D2. The blue areas, overlapped to the conductors, are the radial sectors, built with the angle $\Delta\phi$ computed as in Eq. (3.7). The geometric differences are always of opposite signs and this allows to minimize the errors in the computation of field harmonics.

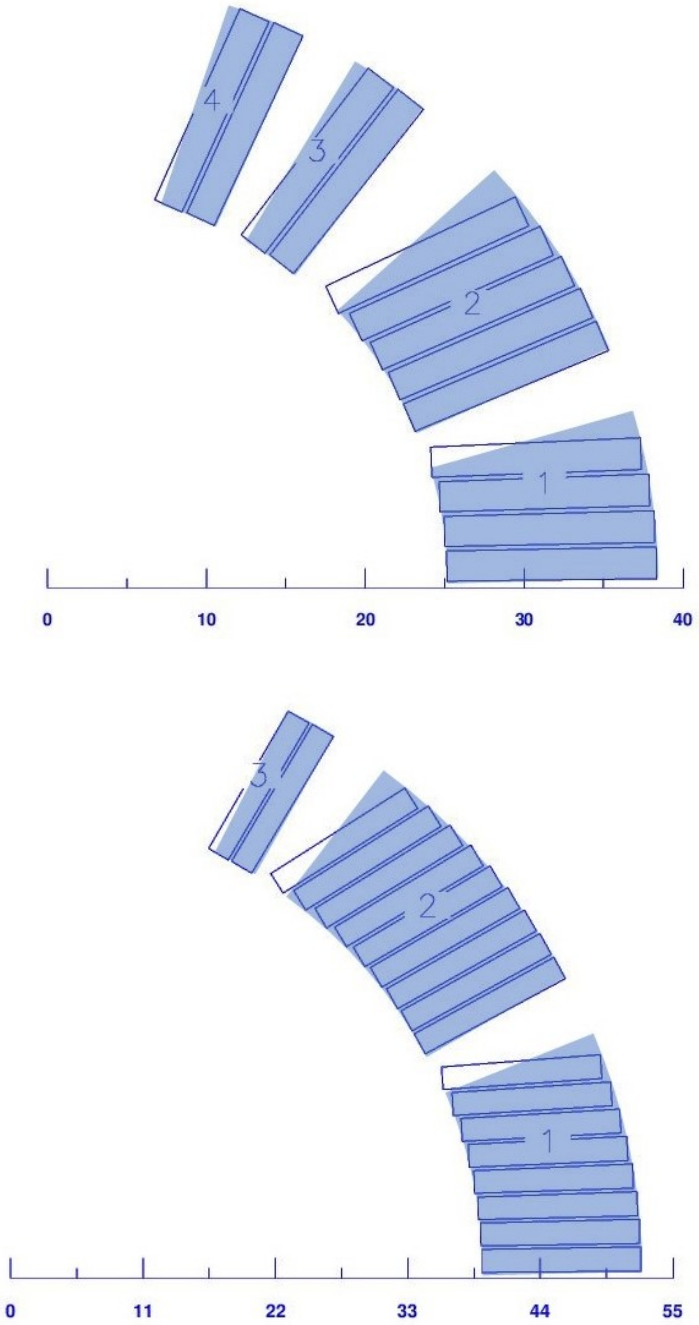

Figure 3.5: Drawing of a coil quarter of the first (top) and second (bottom) layer of FCC bending dipole. The blue areas, overlapped to the conductors, are the radial sectors, built with the angle $\Delta\phi$ computed as in Eq. (3.7). The geometric differences are always of opposite signs and this allows to minimize the errors in the computation of field harmonics.

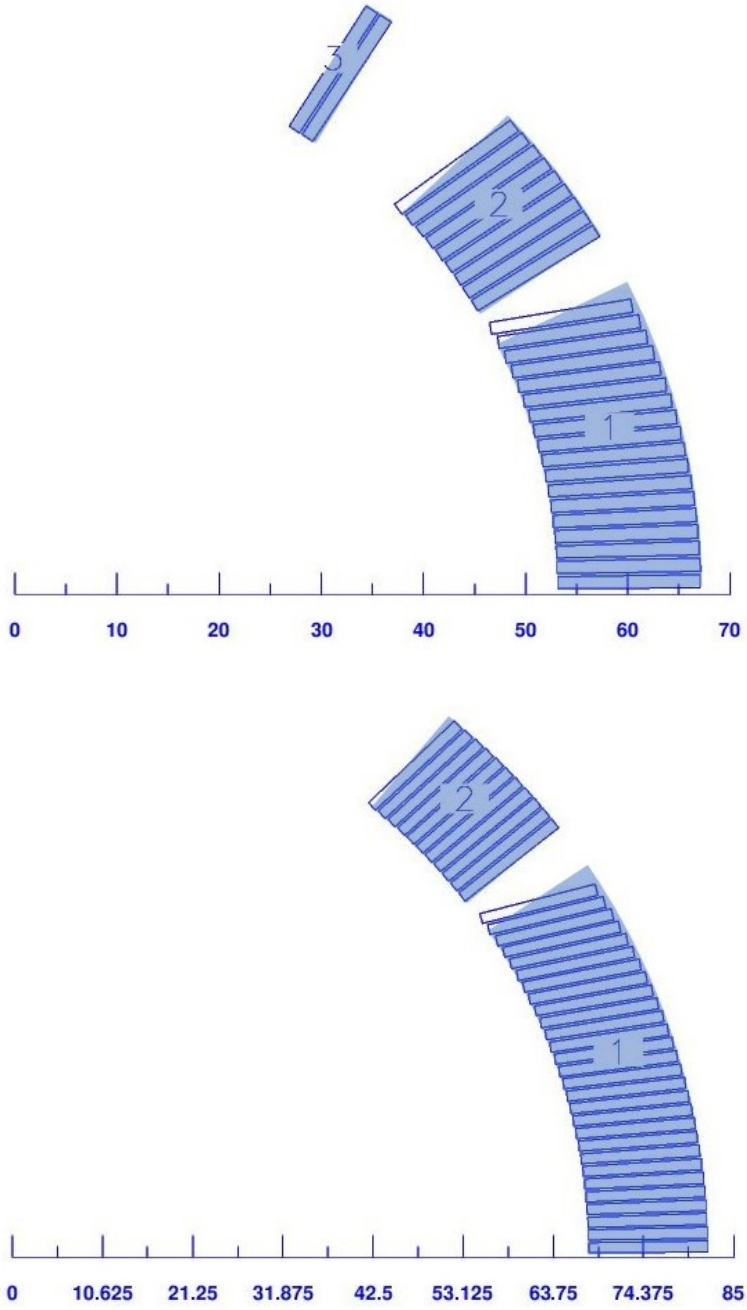

Figure 3.6: Drawing of the third (top) and fourth (bottom) layer of FCC bending dipole. The blue areas, overlapped to the conductors, are the radial sectors, built with the angle $\Delta\phi$ computed as in Eq. (3.7). The geometric differences are always of opposite signs and this allows to minimize the errors in the computation of field harmonics.

The presence of the inter-beam distance prevents the analytical development of the power elevation, as it has been done in Eq. (2.31). The simplest way to work around the problem is to pass through the Cartesian coordinates, as

$$\begin{aligned} B_n + iA_n &= -\frac{\mu_0 I R_{\text{ref}}^{n-1}}{2\pi}\left(\frac{1}{s_1^n}+\frac{1}{s_4^n}\right) - \frac{\mu_0\,(-I)\,R_{\text{ref}}^{n-1}}{2\pi}\left(\frac{1}{s_2^n}+\frac{1}{s_3^n}\right) \\ &= -\frac{\mu_0 I R_{\text{ref}}^{n-1}}{2\pi}\left[\left(\frac{x_1-iy_1}{x_1^2+y_1^2}\right)^n + \left(\frac{x_4-iy_4}{x_4^2+y_4^2}\right)^n\right] \\ &\quad - \frac{\mu_0\,(-I)\,R_{\text{ref}}^{n-1}}{2\pi}\left[\left(\frac{x_2-iy_2}{x_2^2+y_2^2}\right)^n + \left(\frac{x_3-iy_3}{x_3^2+y_3^2}\right)^n\right]. \end{aligned} \tag{3.13}$$

Knowing that

$$\cos(\pi-\theta) = -\cos\theta\,, \quad \cos(\pi+\theta) = -\cos\theta\,, \quad \cos(-\theta) = \cos\theta\,, \tag{3.14}$$

$$\sin(\pi-\theta) = \sin\theta\,, \quad \sin(\pi+\theta) = -\sin\theta\,, \quad \sin(-\theta) = -\sin\theta\,, \tag{3.15}$$

we get

$$\begin{aligned} \frac{x_1-iy_1}{x_1^2+y_1^2} &= \frac{(-2d+\rho\cos\theta_1)-i\rho\sin\theta_1}{(-2d+\rho\cos\theta_1)^2+\rho^2\sin^2\theta_1} \\ &= \frac{-2d+\rho\,(\cos\theta_1-i\sin\theta_1)}{4d^2+\rho^2-4d\rho\cos\theta_1}\,, \end{aligned} \tag{3.16}$$

$$\begin{aligned} \frac{x_2-iy_2}{x_2^2+y_2^2} &= \frac{(-2d-\rho\cos\theta_2)-i\rho\sin\theta_2}{(-2d-\rho\cos\theta_2)^2+\rho^2\sin^2\theta_2} \\ &= \frac{-2d-\rho\,(\cos\theta_2+i\sin\theta_2)}{4d^2+\rho^2-4d\rho\cos\theta_2}\,, \end{aligned} \tag{3.17}$$

$$\begin{aligned} \frac{x_3-iy_3}{x_3^2+y_3^2} &= \frac{(-2d-\rho\cos\theta_2)+i\rho\sin\theta_2}{(-2d-\rho\cos\theta_2)^2+\rho^2\sin^2\theta_2} \\ &= \frac{-2d-\rho\,(\cos\theta_2-i\sin\theta_2)}{4d^2+\rho^2-4d\rho\cos\theta_2} \end{aligned} \tag{3.18}$$

and

$$\begin{aligned}\frac{x_4 - iy_4}{x_4^2 + y_4^2} &= \frac{(-2d + \rho\cos\theta_1) + i\rho\sin\theta_1}{(-2d + \rho\cos\theta_1)^2 + \rho^2\sin^2\theta_1} \\ &= \frac{-2d + \rho\left(\cos\theta_1 + i\sin\theta_1\right)}{4d^2 + \rho^2 - 4d\rho\cos\theta_1}\,.\end{aligned} \tag{3.19}$$

Eq. (3.13) becomes

$$\begin{aligned}B_n + iA_n = &-\frac{\mu_0 I R_{\text{ref}}^{n-1}}{2\pi}\left[\left(\frac{-2d + \rho\left(\cos\theta_1 - i\sin\theta_1\right)}{4d^2 + \rho^2 - 4d\rho\cos\theta_1}\right)^n\right. \\ &\left. + \left(\frac{-2d + \rho\left(\cos\theta_1 + i\sin\theta_1\right)}{4d^2 + \rho^2 - 4d\rho\cos\theta_1}\right)^n\right] \\ &-\frac{\mu_0\left(-I\right)R_{\text{ref}}^{n-1}}{2\pi}\left[\left(\frac{-2d - \rho\left(\cos\theta_2 + i\sin\theta_2\right)}{4d^2 + \rho^2 - 4d\rho\cos\theta_2}\right)^n\right. \\ &\left. + \left(\frac{-2d - \rho\left(\cos\theta_2 - i\sin\theta_2\right)}{4d^2 + \rho^2 - 4d\rho\cos\theta_2}\right)^n\right].\end{aligned} \tag{3.20}$$

For passing to a sector coil, we have to integrate the current lines over the sectors ($I \rightarrow J\rho d\rho d\theta$). However, Eq. (3.20) can not be analytically integrated over the polar coordinates, and a numerical solution is required. In an optimization process, we should iteratively solve the integral over a higher number of sectors. The iterative numerical solution of this integral would be time-consuming and slow down the optimization process. Thereby, we considered another way.

3.2.4 Cross-talk: current-line model

The left coil conductors are far from the right coil aperture, the region where the harmonics are computed. Therefore, we can analytically describe the left coil harmonic contribution approximating each conductor by a single current line, flowing in the center of the turn itself (see Fig. 3.8). Modeling each conductor of the left coil by a matrix of current lines, we verified that this approximation brings to a maximum error of about 5% on the harmonics computation.

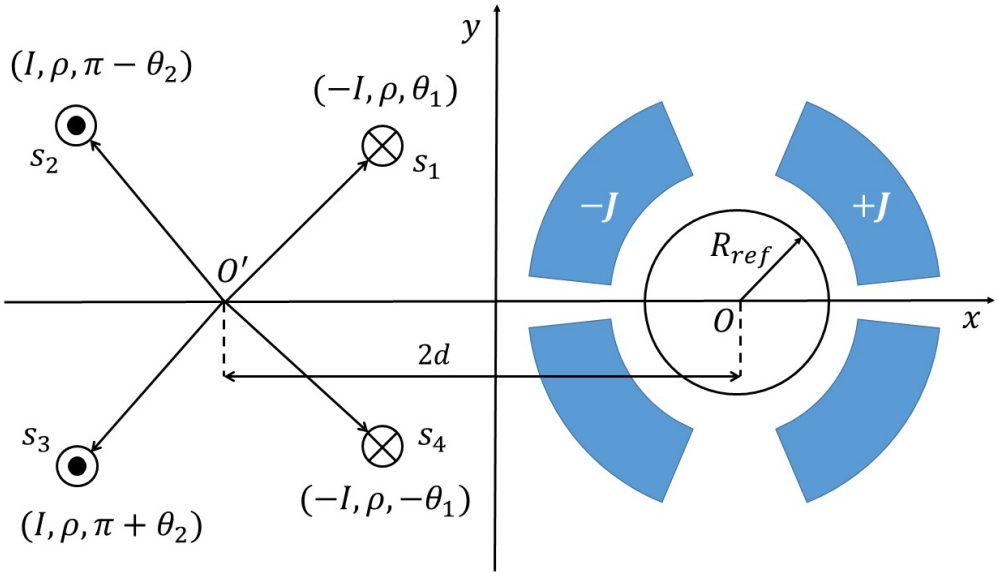

Figure 3.7: Quadruplet of current lines for building the left coil in the twin-aperture layout. The quadruplet is symmetric about the x-axis and asymmetric about its vertical axis. d is half of the inter-beam distance.

The contribution of the left coil, in the right coil aperture, is

$$\begin{aligned} B_n^l = &-\frac{\mu_0 I R_{ref}^{n-1}}{2\pi} \sum_{i=1}^{m} \frac{\cos n\,(\pi - \theta_i)}{\rho_i^n} \\ &- \frac{\mu_0 I R_{ref}^{n-1}}{2\pi} \sum_{i=1}^{m} \frac{\cos n\,(\pi + \theta_i)}{\rho_i^n} \\ &- \frac{\mu_0\,(-I)\,R_{ref}^{n-1}}{2\pi} \sum_{i=1}^{m} \frac{\cos n\,\left(\pi - \theta_i^{'}\right)}{\left(\rho_i^{'}\right)^n} \\ &- \frac{\mu_0\,(-I)\,R_{ref}^{n-1}}{2\pi} \sum_{i=1}^{m} \frac{\cos n\,\left(\pi + \theta_i^{'}\right)}{\left(\rho_i^{'}\right)^n}\,, \end{aligned} \tag{3.21}$$

where ρ_i and θ_i are the polar coordinates of the current lines of the left sectors and $\rho_i^{'}$ and $\theta_i^{'}$ are the polar coordinates of the current lines of the

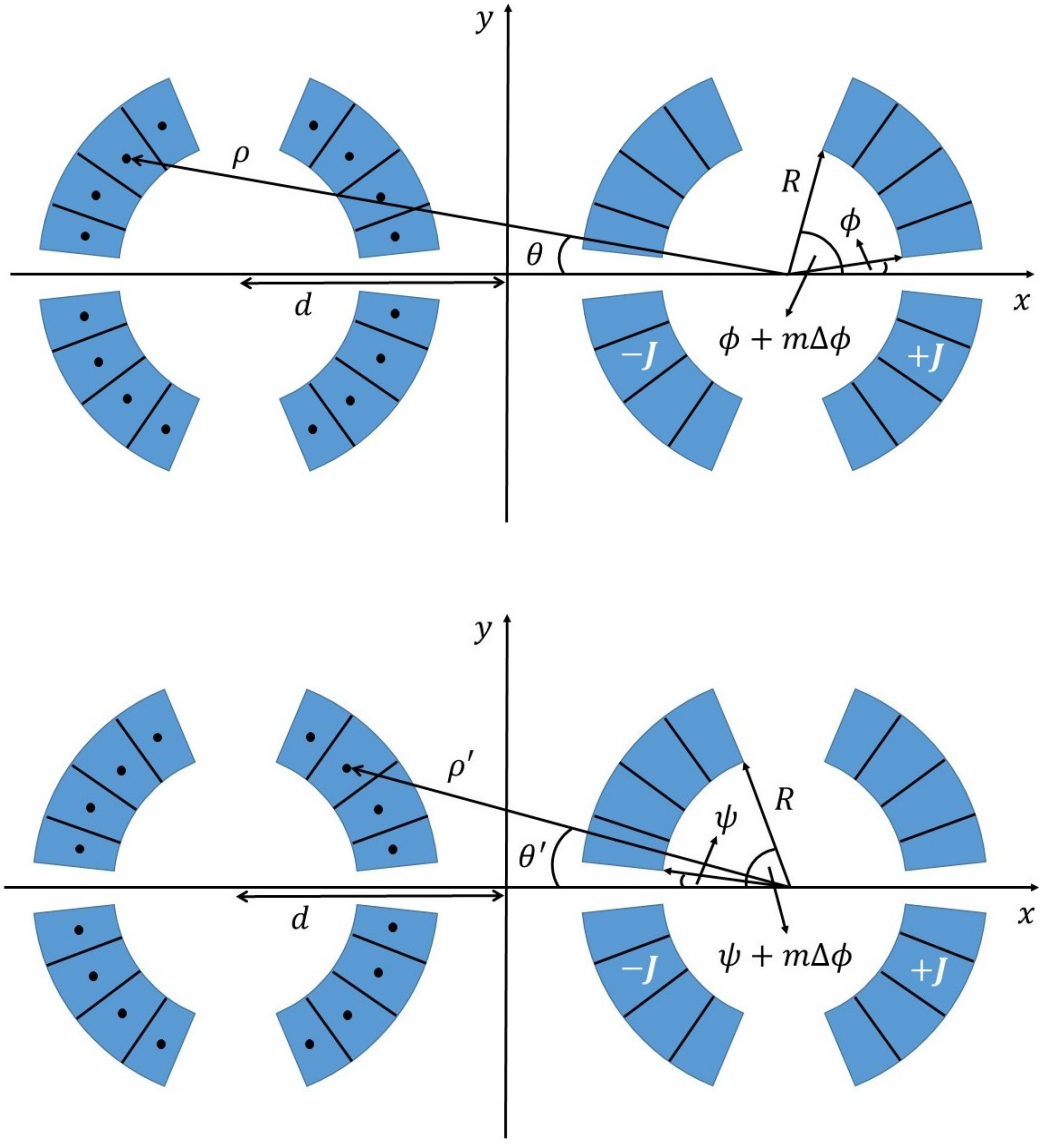

Figure 3.8: Twin-aperture layout. The two sector coils are mirrored, because the beams are counter-rotating. Each coil has the asymmetric cross-section about its vertical axis. The conductors of the left coil are approximated by single current lines, flowing in the center of the conductors themselves (black points). $\rho, \theta, \rho^{'}, \theta^{'}$ are the coordinates of each current line. ρ and θ are linked to the coordinates ϕ and m of the corresponding sector in right half of the right coil (top figure), while $\rho^{'}$ and $\theta^{'}$ are linked to the coordinates ψ and m of the corresponding sector in the left half of the right coil (bottom figure). d is half of the inter-beam distance.

right sectors. By using Eq. (2.32), we get

$$\begin{aligned} B_n^l = &- (-1)^n \frac{\mu_0 I R_{ref}^{n-1}}{\pi} \sum_{i=1}^{m} \frac{\cos n\theta_i}{\rho_i^n} \\ &- (-1)^n \frac{\mu_0 (-I) R_{ref}^{n-1}}{\pi} \sum_{i=1}^{m} \frac{\cos n\theta_i'}{\left(\rho_i'\right)^n} . \end{aligned} \tag{3.22}$$

We set the verses of the currents in a way that the magnetic field in the left aperture has polarity opposite than the right aperture. This is the case of the 16-T bending dipole for FCC. Instead, for the recombination dipole D2 of HL-LHC, the magnetic field must have the same polarity in the two aperture and this condition is realized if we reverse the verses of the currents in Eq. (3.22).

The current density J, which flows in the conductors of the right coil, is linked to the current intensity I, as $J = I/S$, where S is the area of each conductor, computed as

$$S = \int_R^{R+w} \rho \, d\rho \int_0^{\Delta\phi} d\theta = \frac{(R+w)^2 - R^2}{2} \Delta\phi \, . \tag{3.23}$$

The polar coordinates of the current lines, $\rho_i, \theta_i, \rho_i', \theta_i'$, are linked to the angles ϕ or ψ of the corresponding sector of the right coil, by the simple trigonometric formulas. First, we define the polar coordinates of the current lines in the middle of each turn of the right coil as

$$\begin{aligned} r &= R + \frac{w}{2} \, , \\ \gamma_i &= \phi + \left(i + \frac{1}{2} \right) \Delta\phi \, , \\ \gamma_i' &= \psi + \left(i + \frac{1}{2} \right) \Delta\phi \, , \end{aligned} \tag{3.24}$$

where i is an integer number from 0 to $m-1$. Then, we set the polar coordinates of the current lines of the left coil, splitting between right and left sectors. Indeed, because the beams are counter-rotating, the left coil is mirrored to the right coil. Therefore, the left sectors of the left coil correspond to the right sectors of the right coil and the right sectors of the left coil correspond to the left sectors of the right coil.

For the left sectors of the left coil, the trigonometric formulas are

$$\begin{aligned} \theta_i &= \arctan\left(\frac{r\sin\gamma_i}{2d + r\cos\gamma_i}\right), \\ \rho_i &= \frac{2d + r\cos\gamma_i}{\cos\theta_i}, \end{aligned} \tag{3.25}$$

where d is half of the inter-beam distance; while for the right sectors of the left coil we have

$$\begin{aligned} \theta_i^{'} &= \arctan\left(\frac{r\sin\gamma_i^{'}}{2d - r\cos\gamma_i^{'}}\right), \\ \rho_i^{'} &= \frac{2d - r\cos\gamma_i^{'}}{\cos\theta_i^{'}}. \end{aligned} \tag{3.26}$$

Equations (3.24), (3.25) and (3.26) require to rewrite the summation in Eq. (3.22), which becomes

$$\begin{aligned} B_n^l = &-(-1)^n \frac{\mu_0 I R_{ref}^{n-1}}{\pi} \sum_{i=0}^{m-1} \frac{\cos n\theta_i}{\rho_i^n} \\ &-(-1)^n \frac{\mu_0 (-I) R_{ref}^{n-1}}{\pi} \sum_{i=0}^{m-1} \frac{\cos n\theta_i^{'}}{\left(\rho_i^{'}\right)^n}. \end{aligned} \tag{3.27}$$

3.2.5 Total normalized harmonics

The normalized harmonics, produced in the right coil aperture by the two coils, are

$$\begin{aligned} &b_n^{coil}\left(\phi_1, \psi_1, m_1, \ldots, \phi_N, \psi_N, m_N\right) \\ &= 10^4 \frac{\sum_{p=1}^{N}\left[B_n^r\left(\phi_p, \psi_p, m_p\right) + B_n^l\left(\phi_p, \psi_p, m_p\right)\right]}{\sum_{p=1}^{N}\left[B_1^r\left(\phi_p, \psi_p, m_p\right) + B_1^l\left(\phi_p, \psi_p, m_p\right)\right]}, \end{aligned} \tag{3.28}$$

where N is the number of the coil sectors.

In the FCC bending dipole, the minimal distance between neighboring blocks makes difficult to consider the iron yoke saturation only in the next phase of the design process. Indeed, fine-tuning of the block positions to correct too big iron yoke contributions and too large errors in the harmonics computation could lead to too small wedges.

For solving this issue, we must consider in the theoretical model the iron yoke saturation and the harmonic error due to the geometric differences between the sector coil and the real coil. We observed that these contributions poorly depend from the "coordinates" of the configuration (ϕ_p, ψ_p, m_p). Then, we can regard the shift from the model solution, $\Delta b_n^{sat+geom}$, approximately as a constant value, which can be estimated by a single FEM evaluation [18]. Therefore, the total normalized harmonics are

$$\begin{aligned} & b_n\left(\phi_1, \psi_1, m_1, \ldots, \phi_N, \psi_N, m_N\right) \\ & \quad = b_n^{coil}\left(\phi_1, \psi_1, m_1, \ldots, \phi_N, \psi_N, m_N\right) + \Delta b_n^{sat+geom} . \end{aligned} \tag{3.29}$$

3.3 Numerical solution

3.3.1 Objective function and iterative method

The global minimization of the quadratic sum of the total normalized harmonics is a so-called *Mixed-Integer Non-Linear Programming* (MINLP) problem, which can be solved through the *Evolutionary Algorithms* (EA). The *Genetic Algorithms* (GA) have been the prototype of EA. They can quickly scan design spaces with multiple minimums and discrete design variables, but undergo the problem of the so-called *premature convergence*, i.e., they stop before the global optimum is reached because they remain trapped into a local optimum [18].

This problem turned out particularly important in the global minimization of the quadratic sum of the total harmonics. Setting to zero the overall contributions of both coils is more complicated than setting to zero the contributions of only one coil. Moreover, we want to find the coil designs with few sectors as possible. Decreasing the number of the sectors, we have fewer design variables to minimize the same number of harmonics. Considering that we must put also some non-linear constraints over the variables, the problem becomes computationally difficult. For simplifying the issue and for reducing the probability of premature convergence, we minimize the objective function through an iterative procedure:

1. we generate a random configuration of the left coil (ϕ_1, ψ_1, m_1, …, ϕ_N, ψ_N, m_N) and compute the harmonics $B_n^l\left(\phi_p, \psi_p, m_p\right)$ in Eq. (3.28);

2. we numerically find a configuration of the right coil ($\phi_1^{'}$, $\psi_1^{'}$, $m_1^{'}$, …, $\phi_N^{'}$, $\psi_N^{'}$, $m_N^{'}$), for whom the multipoles $B_n^r\left(\phi_p^{'}, \psi_p^{'}, m_p^{'}\right)$ delete the harmonics $B_n^l\left(\phi_p, \psi_p, m_p\right)$;

3. we check the total normalized harmonics $b_n(\phi_1^{'}, \psi_1^{'}, m_1^{'}, \ldots, \phi_N^{'}, \psi_N^{'}, m_N^{'})$ and we stop if b_2 and b_3 are within few units (the higher order harmonics are already within one unit after the first iteration);

4. otherwise we update the contributions of the left coil $B_n^l\left(\phi_p^{'}, \psi_p^{'}, m_p^{'}\right)$ and we repeat the steps 2 and 3.

3.3.2 Differential Evolution algorithm

The second step of the iterative method is solved through the *Differential Evolution* (DE) algorithm [4, 6]. It is arguably one of the most powerful stochastic real-parameter optimization algorithms in current use. Many engineering applications have benefited from the powerful nature of DE. An overview of the main algorithm variants and the engineering applications can be found in Ref. [19].

We used the version implemented in Wolfram Mathematica 11.3 [70]. The algorithm works with a population of m points, $(x_1, x_2, \ldots, x_j, \ldots, x_m)$, where $m \gg n$, with n being the number of variables. A new population of m points is generated during each iteration of the algorithm. The new point x_j is built by picking three random points x_u, x_v and x_w from the old population and forming the point x_s as

$$x_s = x_w + s\left(x_u - x_v\right) , \tag{3.30}$$

where s is a real scaling factor. Then, a new point x_{new} is generated from x_j and x_s by taking the coordinates from x_s with probability ρ and from x_j with probability $1-\rho$. If $f(x_{new}) < f(x_j)$, x_{new} replaces x_j in the population. The probability ρ is called cross probability.

The process stops if the difference between the best function values in the new and old populations, as well as the distance between the new best point and the old best point, is less than the tolerances.

We empirically determined that the optimal values of the scaling factor s are 0.2 for the dipole D2 and 0.3 for the FCC bending dipole. We used a population of 2000 points for the dipole D2 and 1800 points for the FCC bending dipole.

3.3.3 Non-linear constraints

The objective function is minimized with lower and upper limits on each variable ϕ_p, ψ_p, m_p. However, if the positions and the dimensions of the coil blocks are unknown, as it usually happens in the early stage of the design process, these limits require careful. Indeed, too tight limits could lead to

fail the optimization process and too wide limits could bring to overlap the sectors. This problem is solved by putting the non-overlapping constraints:

$$\begin{aligned} \phi_{p+1} &\geq \phi_p + m_p \, \Delta\phi \,, \\ \psi_{p+1} &\geq \psi_p + m_p \, \Delta\phi \,. \end{aligned} \tag{3.31}$$

Owing to the previous constraints, we can put wide limits on each variable because the non-overlapping of the sectors is guaranteed.

Eq. (3.31) is sufficient in the dipole D2 of HL-LHC, but not in the FCC bending dipole. Due to the geometric differences between the real blocks and the radial sectors (see Fig. 3.5 and Fig. 3.6), it still allows the overlapping of the real blocks. This issue can be solved reinforcing Eq. (3.31) in two different ways. On one hand, we can add a distance factor D, as

$$\begin{aligned} \phi_{p+1} &\geq \phi_p + (m_p + D) \, \Delta\phi \,, \\ \psi_{p+1} &\geq \psi_p + (m_p + D) \, \Delta\phi \,. \end{aligned} \tag{3.32}$$

On the other hand, in the constraint definition we can use an angle $\Delta\phi^{'}$ greater than $\Delta\phi$, as

$$\begin{aligned} \phi_{p+1} &\geq \phi_p + m_p \, \Delta\phi^{'} \,, \\ \psi_{p+1} &\geq \psi_p + m_p \, \Delta\phi^{'} \,. \end{aligned} \tag{3.33}$$

Eq. (3.32) and (3.33) impose a minimum distance between the sectors and then guarantee that when we change to the real blocks, they are not overlapped. For FCC bending dipole we chose to use the distance factor, which we empirically determined for each layer.

To ensure that the found solutions generate the nominal dipole field in the bore, we put constraints on the number of conductors per layer, as

$$M_{inf} \leq \sum_{p=1}^{N_l} m_p \leq M_{sup} \,, \tag{3.34}$$

where N_l is the number of blocks per layer, M_{inf} and M_{sup} are the minimum and maximum number of conductors per layer, respectively. Eventually, it is possible to put a constraint also on the overall number of the coil conductors.

Part II

Numerical Simulations

Chapter 4

Bending Dipole for FCC

4.1 Introduction

As members of the EuroCirCol collaboration, we have helped to develop the 2D electromagnetic design of the $\cos\theta$ layout. In particular, we have been responsible for the 3D electromagnetic modeling, which we have realized by two different tools. The first is the commercial software Opera [45] based on the Finite Element Method (FEM). The second is a specific CERN program, ROXIE [9], based on the coupling between the Boundary Element Method and the Finite Element Method (BEM-FEM) [18].

In this chapter, we describe two designs of the 16-T bending dipole (arc dipole magnet). The former is characterized by a symmetric coil cross-section and an inter-beam distance of 204 mm. This layout is an evolution of that published in Ref. [44, 48] and has been the first design to be chosen as baseline. However, it has a high quadrupole harmonics due to the magnetic cross-talk. Studies on the beam dynamics showed that this component is not acceptable. So, the design has been changed by increasing the inter-beam distance to 250-mm and by adopting an asymmetric coil layout [69]. The analytical methodologies described in chapter 3 have been useful to quickly scan the parameter space and ensure that the proposed configuration is one of the best possible.

4.2 Design with symmetric coil

4.2.1 Design parameters

The EuroCirCol collaboration approved a common design parameter set for comparing the different layouts and choosing the preferred design between

Table 4.1: Main design parameters.

Feature	Unit	Value
Material		Nb_3Sn
Bore magnetic field	T	16
Magnetic length	m	14.3
Aperture diameter	mm	50
Beam distance	mm	204
Iron yoke outer radius	mm	300
Operating temperature	K	1.9
Critical current density	A/mm^2	2250
Operating point on load-line	%	86
Maximum no. of strands		40
Cu/non-Cu		≥ 0.8
Insulation thickness	mm	0.15
Field harmonics (geom/sat)	unit	$\leq 3/10$
Number of apertures		2

the four options (see Fig. 1.13) [41, 50]. We report these parameters in Table 4.1.

Initially, the inter-beam distance had been set to 250 mm to accommodate an adequate mechanical structure. However, after an optimization process, we found that smaller and more compact solutions are possibles. So, the collaboration reduced the inter-beam distance to 204 mm.

The analysis of the fringe magnetic field, i.e., the magnetic field dispersed in the tunnel, permitted to fix the maximum iron yoke diameter at 600 mm.

These choices are not strictly necessary for the FCC tunnel. However, they allow to fit the cryostat dimension at the LHC tunnel and to use the same magnet design both for FCC and HE-LHC. Unfortunately, in these size constraints, the cross-talk is not negligible and requires careful evaluation in the magnetic optimization process.

An important feature of the superconducting material is the *critical current density* (J_c). It defines the maximum current density that can flow in the superconductor. Consequently, it set how much superconductor is needed in the coils to achieve the nominal field. Reducing this amount is very important for decreasing the magnet costs. An R&D program is in progress to increase the Nb_3Sn strand performances. The EuroCirCol collaboration decided to use the expected J_c-value, which is fixed to about 1500 A/mm^2 at 16 T with a temperature of 4.2 K [27, 58]. The cost target is fixed to

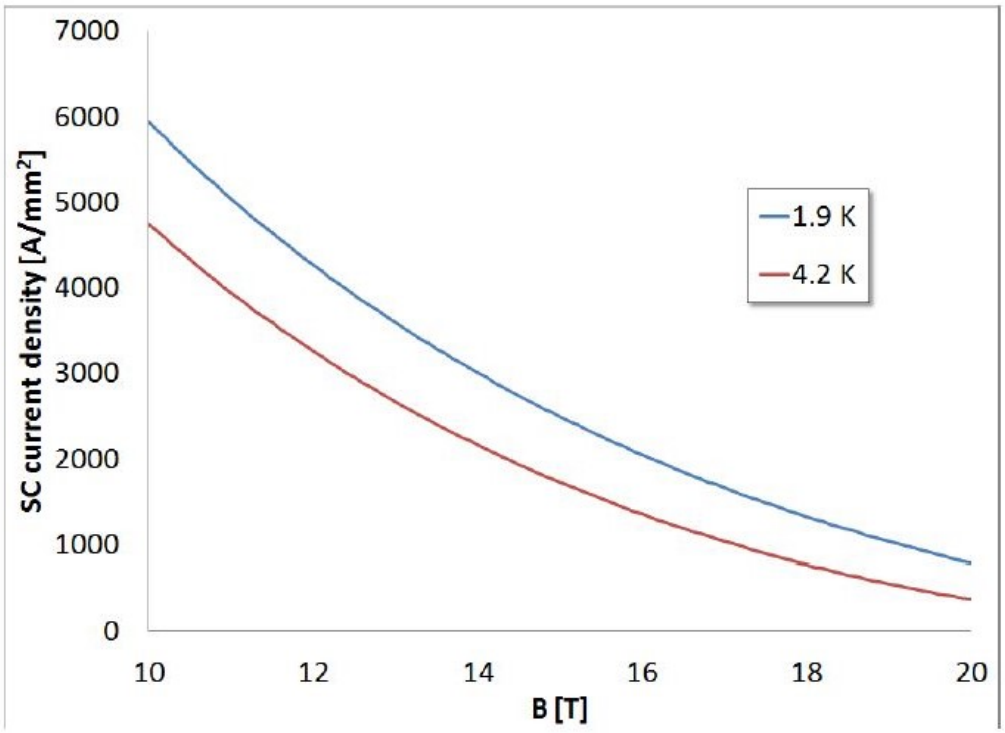

Figure 4.1: The superconductor critical current density, J_c, as a function of the magnetic field in the aperture. The red curve corresponds to Nb_3Sn strands cooled at the temperature of 4.2 K. The blue curve corresponds to strands cooled at the temperature of 1.9 K.

5 €/kAm, which is competitive for the industrial production [38, 66].

If we plot the critical current density as a function of the magnetic field in the aperture, we obtain the critical curve of the superconducting material. Fig. 4.1 shows the critical curves expected from the high-performance Nb_3Sn strands. The red curve corresponds to strands cooled at the temperature of 4.2 K. The blue curve corresponds to strands cooled at the temperature of 1.9 K. Because the magnet must work at the temperature of 1.9 K, the corresponding critical current density at 16 T is about 2250 A/mm^2.

If we plot the current density that really flows in the superconductor as a function of the magnetic field generated in the aperture, we obtain the so-called *load-line* (see Fig. 4.4). It must cross the critical current density in an intersection point, which depends on the temperature. This point represents the maximum current that the magnet can carry. Above this value, a quench certainly occurs. A superconducting magnet cannot work at its maximum current, because the slightest disturbance can induce a quench. Therefore,

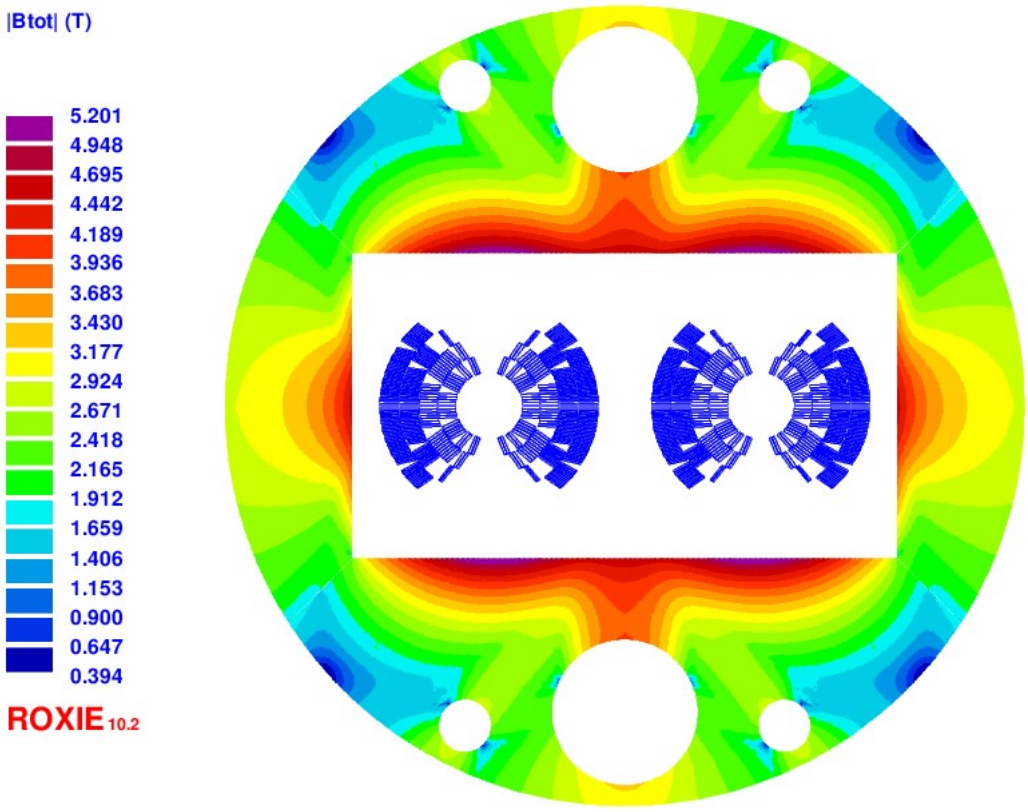

Figure 4.2: Design of the iron yoke surrounding the two coils. The magnetic field is shown at the operating current.

the magnet must work at an operating point, which is under the critical curve with a minimum margin. For the FCC bending dipole, the EuroCirCol collaboration chose a minimum margin of about 14%.

4.2.2 Magnetic design

2D model

The magnet cross-section is shown in Figures 4.2 and 4.3. The former shows the design of the iron yoke surrounding the two coils. The latter displays the coil cross-section, symmetric with respect to the horizontal and vertical axes. As we demonstrated in Section 2.4, these symmetries delete the skew and normal even harmonics, which are generated by only one coil. Due to the cross-talk, only the skew harmonics are zero and the normal harmonics must be controlled by the optimization process.

For obtaining the nominal field in the bore, we designed the coil with

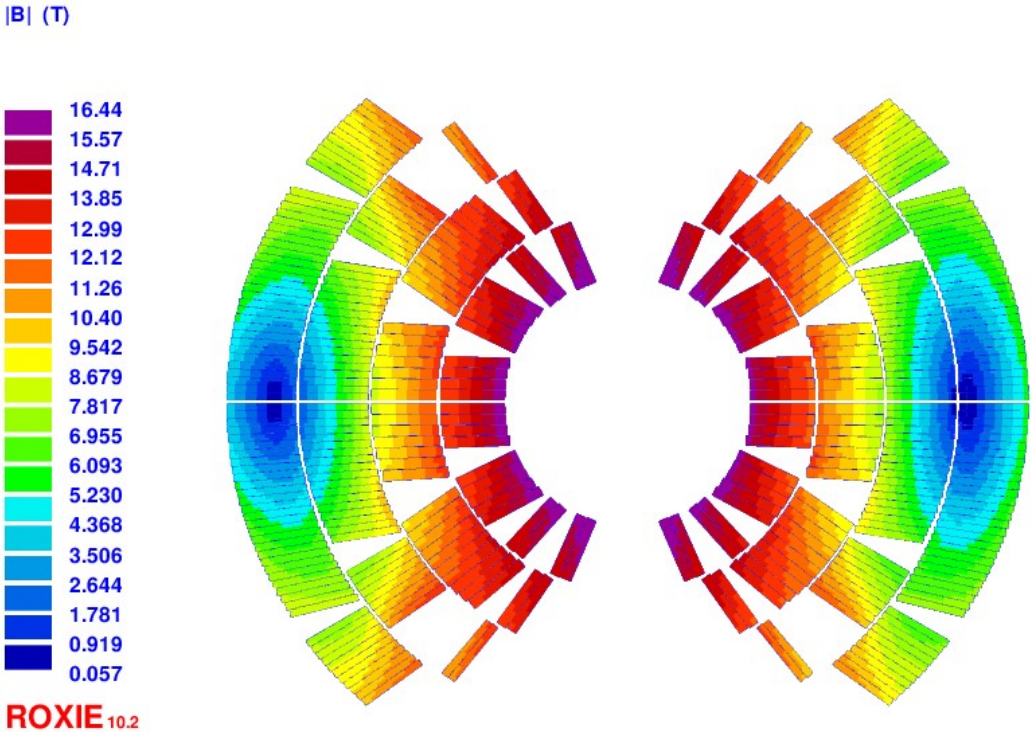

Figure 4.3: Symmetric coil cross-section. The magnetic field is shown at the operating current.

four layers. The cable used in the first and second layer is different from that used in the third and the fourth layer. This technique is called *grading* and is commonly used to increase the cable efficiency in the areas far away from the bore, where the field is smaller. Indeed, the conductor used in the last two layers is thinner and permits to obtain a higher current density. In this way, the cable efficiency is higher and allows to minimize the conductor amount. At the same time, the copper content in the cable is higher for decreasing the current density that flows in the copper during a quench. Table 4.2 shows the main features of the two conductors and Fig. 4.4 shows their load-lines. "High-field (HF) conductor" refers to the cable used in the first two layers, while "low-field (LF) conductor" refers to the cable used in the last two.

Each coil is shaped by winding the two conductors to form four double pancakes, which are connected in series on the mid-plane by using joints in NbTi, a technique which has been already used for the Nb_3Sn MQXF magnets [32].

The number of turns for each layer is shown in Table 4.3. The large amount of wedges between the blocks (8 for coil quarter) helps to reduce the

peak field on the conductors. The minimum wedge thickness is 0.86 mm, between second and third block of the first layer. The peak field (16.4 T) on the HF conductor is localized on the fourth block of the first layer in the coil side facing the other coil (the left side of the coil in Fig. 4.3). The peak field (12.8 T) on the LF conductor is situated on the third block of the third layer in the coil side facing the other coil (the left side of the coil in Fig. 4.3).

Fig. 4.5 shows the inductance and the energy stored in the magnet as a function of the current. At the nominal one, the inductance is 39.6 mH/m and the stored energy is 2.6 MJ/m. The total inductance is about 570 mH and the stored energy is roughly 37 MJ.

Tables 4.4 and 4.5 show the normal harmonics at the nominal current up to the 20th order. They depend only on the geometry and the iron saturation, because the persistent current effect has not been yet considered at this design stage. All harmonics are within requirements (see Table 4.1), except b_2. Fig. 4.6 shows the field quality as a function of the current intensity. The strong variation of b_2 and b_3 is due to the iron saturation.

3D model

A magnet for accelerator has two ends: the side of the connections between the blocks and the layers (see Figures 4.7), and the side opposite to the connections (see Fig. 4.8). Due to the complexity of the coil and for easing the computation through ROXIE and Opera, we have created an independent model for each extremity with a magnetic length arbitrarily shorter than the design one. These models have allowed to quickly evaluate the effects of each head on the harmonics of the cross-section. Then, we have predicted the overall harmonics integrated over the nominal magnetic length ($L_{\mathrm{mag}} =$ 14.3 m) by using the formula

$$\bar{b}_n = \frac{\bar{b}_{n,\,\mathrm{soc}}\, L_{\mathrm{mag,\,soc}} + \bar{b}_{n,\,\mathrm{cs}}\, L_{\mathrm{mag,\,cs}} + b_n\,(z=0)\,(L_{\mathrm{mag}} - L_{\mathrm{mag,\,soc}} - L_{\mathrm{mag,\,cs}})}{L_{\mathrm{mag}}}\,, \tag{4.1}$$

where $\bar{b}_{n,\,\mathrm{soc}}$ and $L_{\mathrm{mag,\,soc}}$ are respectively the integrated harmonics and the magnetic length of the short model for the side opposite to the connections, and $\bar{b}_{n,\,\mathrm{cs}}$ and $L_{\mathrm{mag,\,cs}}$ are respectively the integrated harmonics and the magnetic length of the short model for the connection side. The electromagnetic analysis has shown that the two ends have similar effects on the field quality. In particular, the connection side generates a small component of the dipole skew harmonics ($a_1 = -0.35$ units at the nominal magnetic length) due to the connections that break the coil symmetry with respect to the x-axis. The elevate number of blocks allows to minimize the contribution of each head

Table 4.2: Main features of the conductors.

Feature	Unit	HF	LF
Material		Nb_3Sn	Nb_3Sn
Cu/Non-Cu		0.82	2.08
No. of strands		22	38
Strand diameter	mm	1.1	0.7
Bare width	mm	13.2	14
Bare inner thickness	mm	1.892	1.204
Bare outer thickness	mm	2.0072	1.3261
Insulation thickness	mm	0.15	0.15
Keystone angle	°	0.5	0.5
Operating current	kA	11.39	11.39
Peak field	T	16.4	12.8
Operating point on load-line	%	86	86

Table 4.3: Number of turns on a coil quarter.

Layer 1	13
Layer 2	19
Layer 3	29
Layer 4	39
Total	200

Table 4.4: Lower-order normal harmonics at the operating current.

b_2	b_3	b_4	b_5	b_6	b_7	b_8	b_9	b_{10}
−56.61	1.52	−1.17	−0.97	−0.01	1.78	0	1.45	0

Table 4.5: Higher-order normal harmonics at the operating current.

b_{11}	b_{12}	b_{13}	b_{14}	b_{15}	b_{16}	b_{17}	b_{18}	b_{19}	b_{20}
1.06	0	−0.19	0	0	0	−0.07	0	0	0

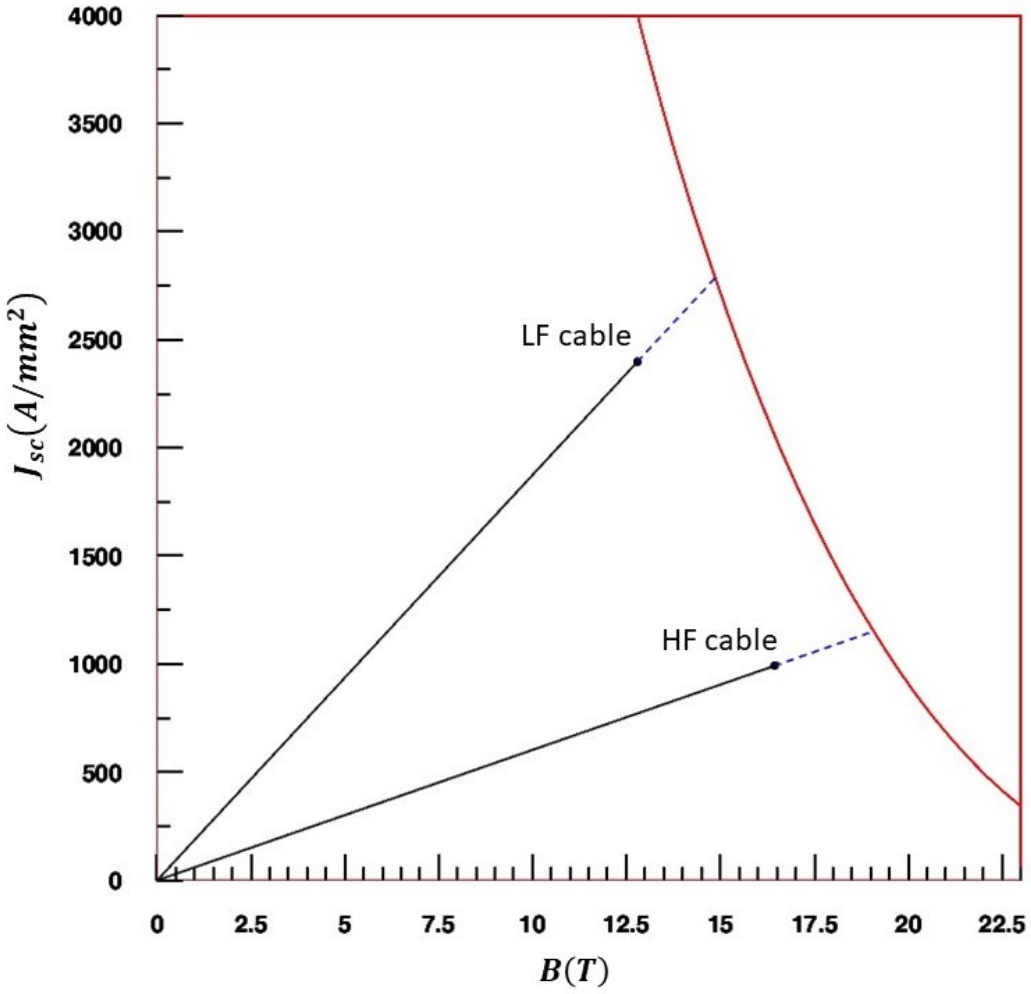

Figure 4.4: Load-lines of the Low-Field (LF) conductor and the High-Field (HF) conductor. The red curve is the Nb_3Sn critical current density. The operating points are about at 86% of the load-lines.

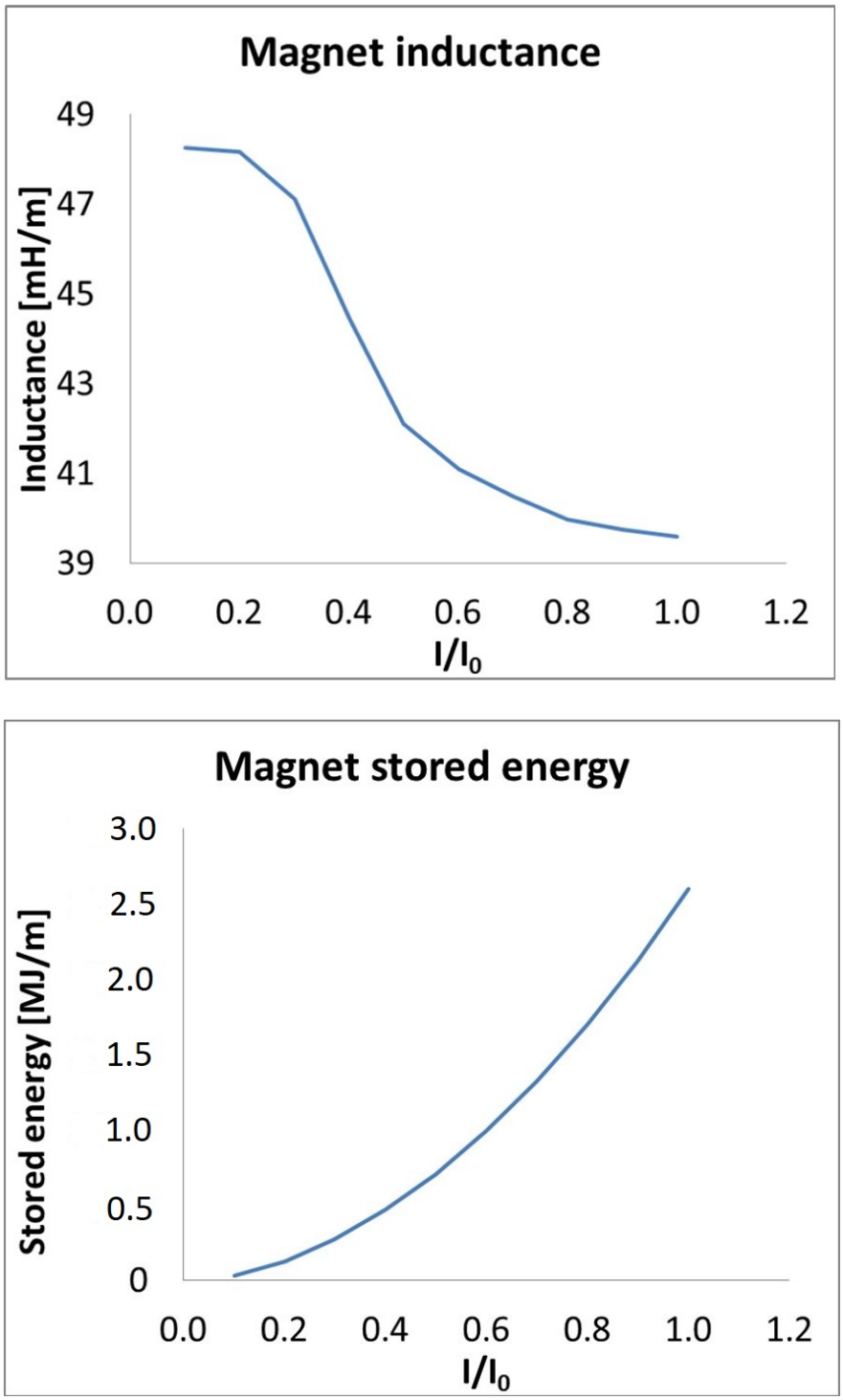

Figure 4.5: Inductance (top) and energy stored (bottom) in the magnet as a function of the current intensity. I_0 is the operating current.

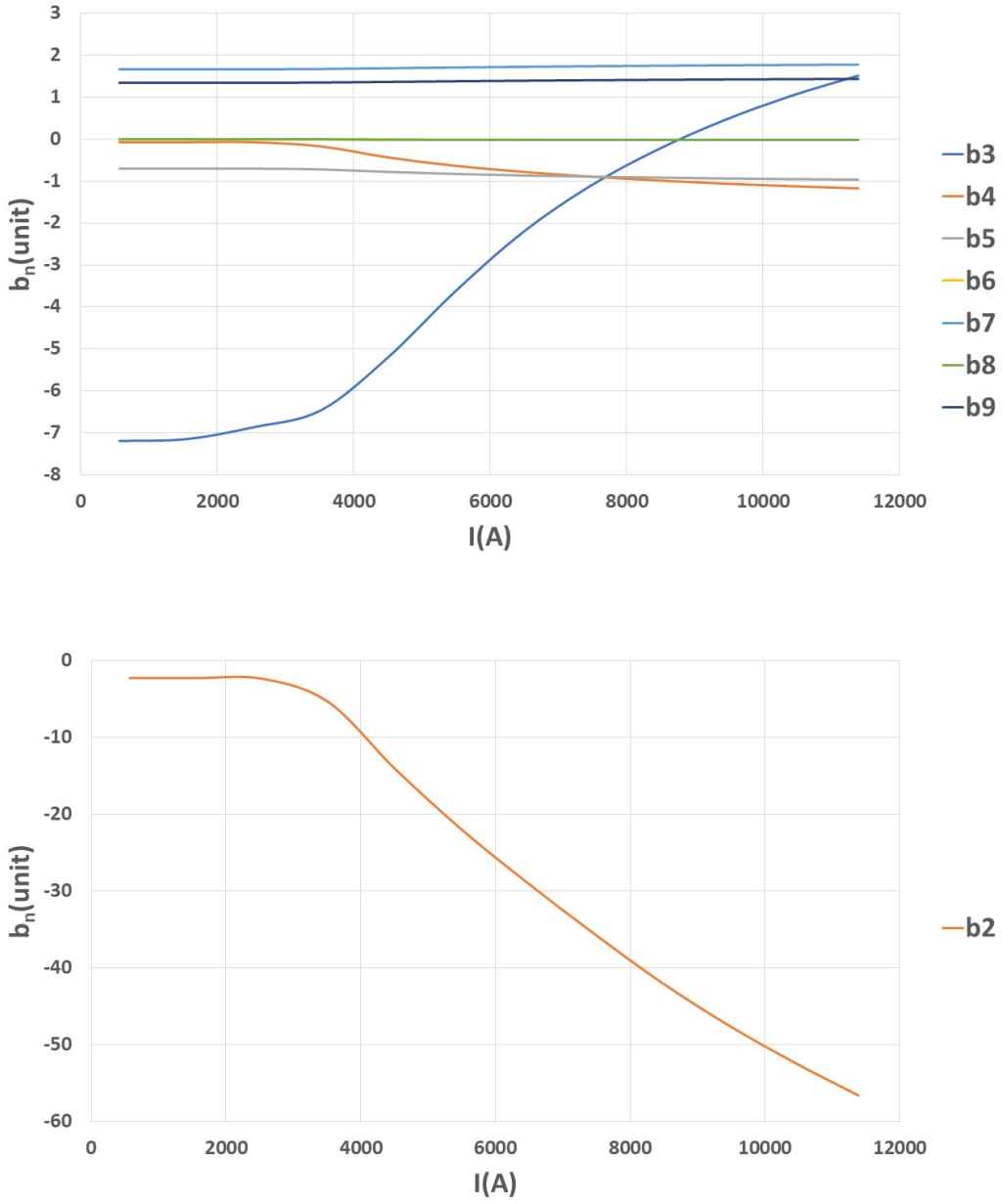

Figure 4.6: Field harmonics as a function of the current intensity.

Table 4.6: Peak fields on the conductors at the operating current in the side opposite to the magnet connections.

Conductor	Cross-section (T)	Coil end (T)	ΔB_{peak} (T)
LF	12.8	12.7	0.1
HF	16.4	14.9	1.5

Table 4.7: Lower-order normal harmonics at the operating current and integrated over the nominal magnetic length for the magnet with the symmetric coil ends (two sides opposite to the connections).

$\bar{b}_2$	$\bar{b}_3$	$\bar{b}_4$	$\bar{b}_5$	$\bar{b}_6$	$\bar{b}_7$	$\bar{b}_8$	$\bar{b}_9$	$\bar{b}_{10}$
−57.23	1.56	−1.17	−0.95	−0.01	1.78	0	1.45	0

by only optimizing the end spacer positions without the need to compensate the residual harmonics with small corrections of the straight part.

Due to the coil return, the peak field on the conductors in the ends is usually higher than in the cross-section (typically several %) [18]. So, spacers are often added in the extremities to reduce the magnetic field. This behavior manifests in the external layers of the coil. In the mechanical design, each layer has its pole (see Fig. 4.19) and this allows the cables to curve in different longitudinal positions (see Figures 4.9 and 4.10). This possibility can be exploited to reduce the peak field without adding spacers and/or drawing back the iron yoke (see Fig. 4.12). In the internal layers, the peak field on the conductors begins to quickly drop after the end of the yoke (see Fig. 4.13). This phenomenon simplifies the design process, precisely where the magnetic field is greater and more difficulties may arise.

In light of these results, we decided to finalize only the side opposite to the connections and postpone the other side after the 3D mechanical simulations. Figures 4.8, 4.10 and 4.11 show the final design. The conductors begin to curve about 10 mm after the end of the iron yoke. The minimum and maximum longitudinal distances between the blocks are about 5.5 mm and 55 mm respectively. The coil end is 230 mm long. The head has a major number of blocks than the cross-section. The first blocks in the third and in the fourth layer have been split with respect to the cross-section. This division has been done because, in a preliminary phase, we have evaluated that such big blocks could be difficult to manage in the ends, which are the most difficult parts to manufacture and are the most unstable from a mechanical point of view. The peak fields on the conductors are reported in

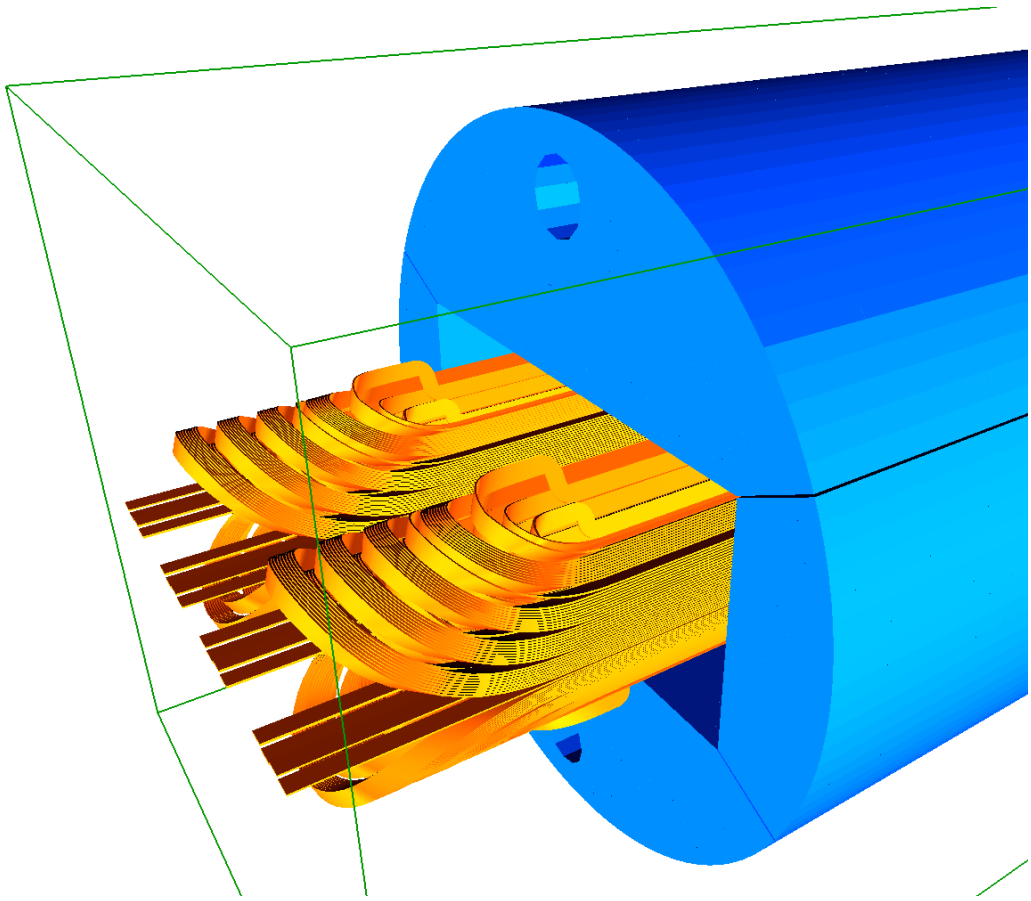

Figure 4.7: Side of the magnet connections in ROXIE. The coils are in yellow and the iron yoke in blue. The latter is a slightly different version with respect to the final one shown in Fig. 4.8.

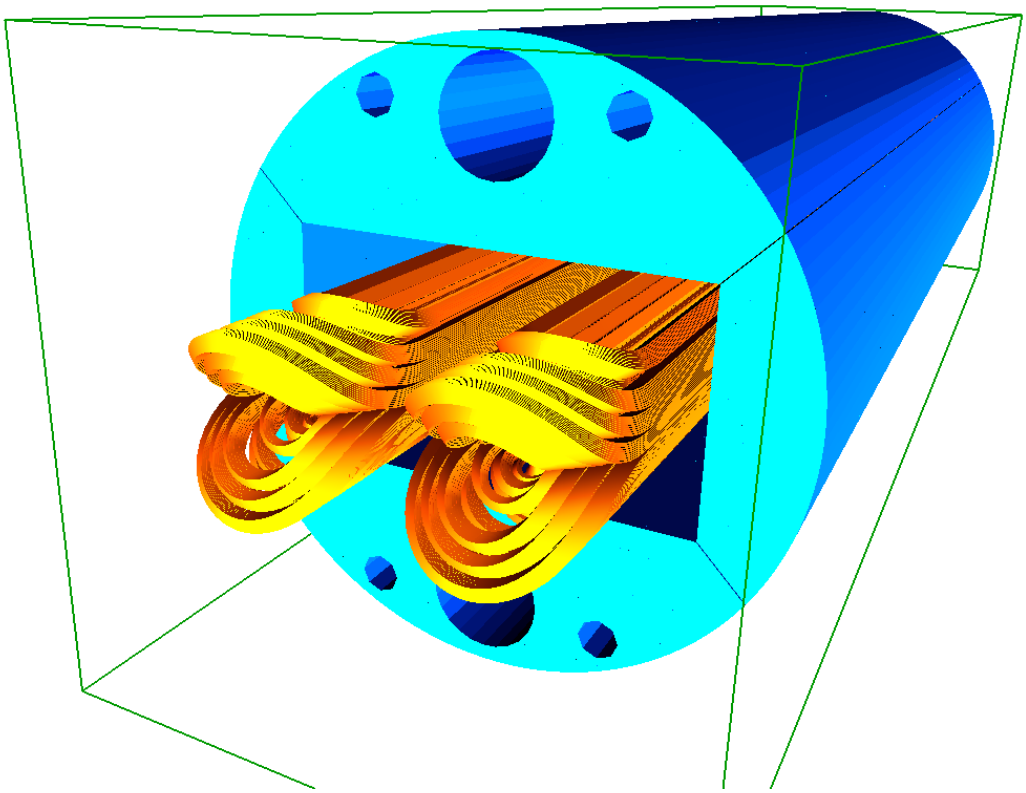

Figure 4.8: Side opposite to the magnet connections in ROXIE. The coils are in yellow and the iron yoke in blue.

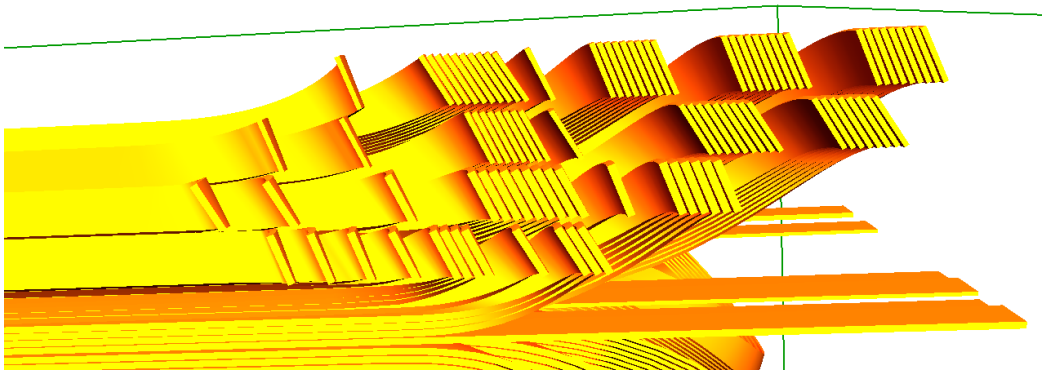

Figure 4.9: Section of the connection side of the magnet. The blocks of the cross-section have been split because of the connections between the blocks and the layers. The peak fields are in the leftmost conductors of the first and third layer. Their values are comparable with those reported in Table 4.6.

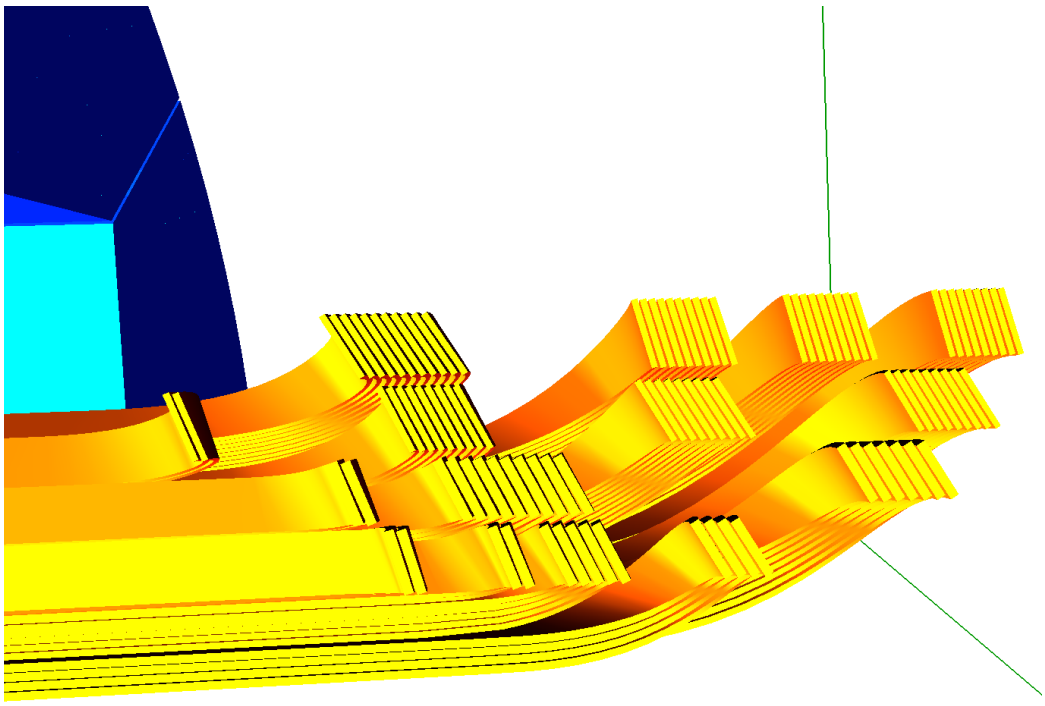

Figure 4.10: Section of the side opposite to the magnet connections. The peak fields are in the leftmost blocks of the first and third layer. Their values are reported in Table 4.6.

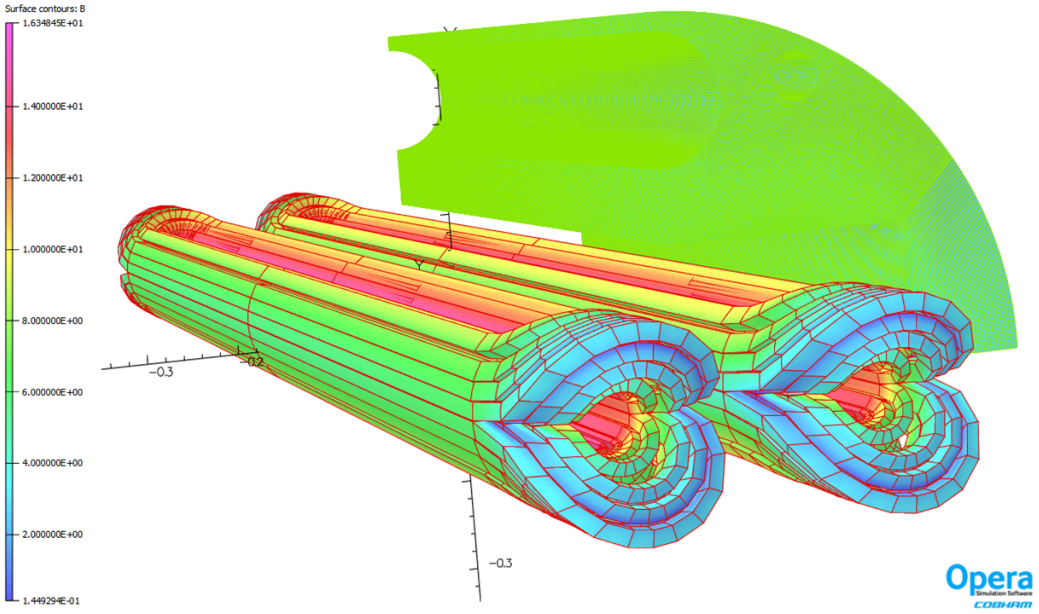

Figure 4.11: 3D electromagnetic model in Opera with the symmetric coil ends (two sides opposite to the connections). The magnetic field is shown at the operating current.

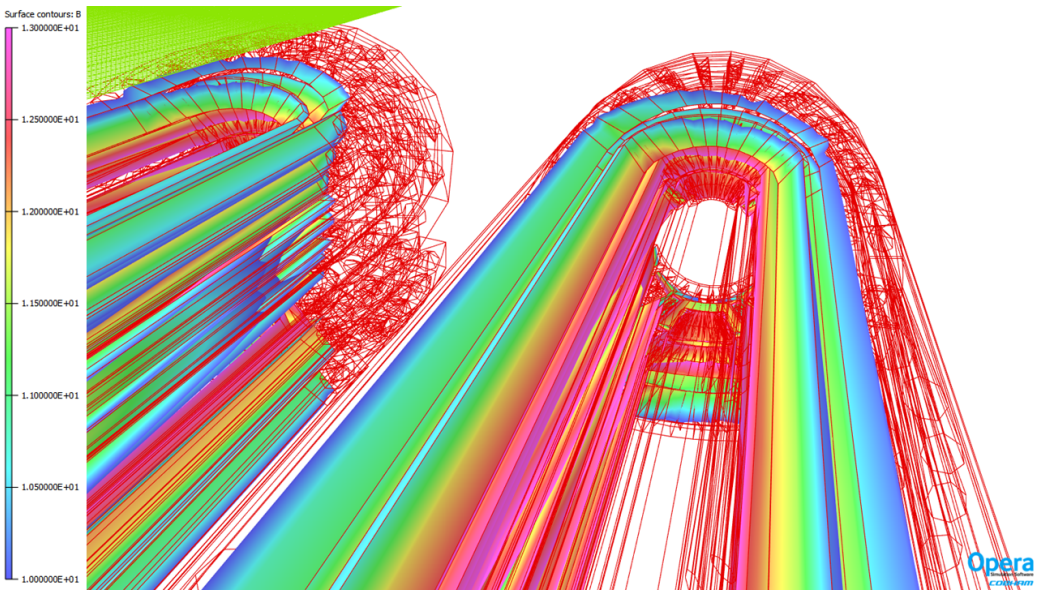

Figure 4.12: Magnetic field at operating current in the third and fourth layer of the side opposite to the magnet connections.

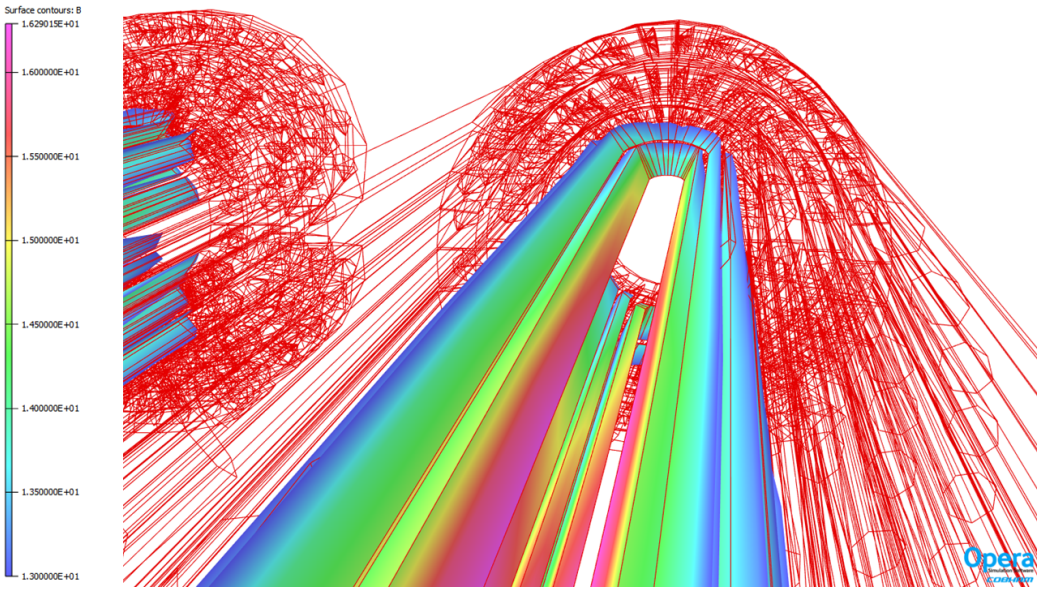

Figure 4.13: Magnetic field at operating current in the first and second layer of the side opposite to the magnet connections.

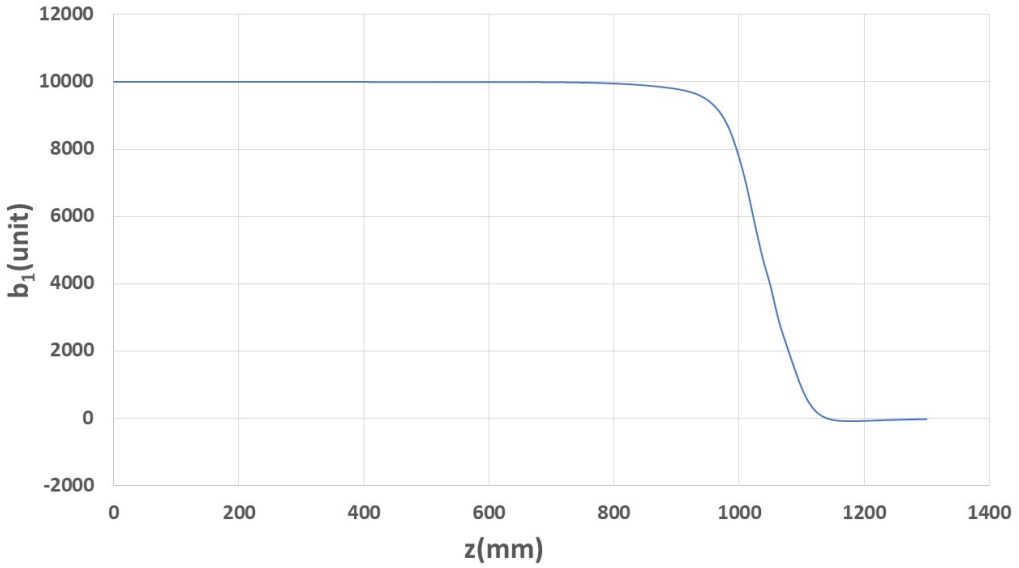

Figure 4.14: The harmonics b_1 as a function of the position along the z-axis for the side opposite to the magnet connections. The iron yoke ends at 890 mm.

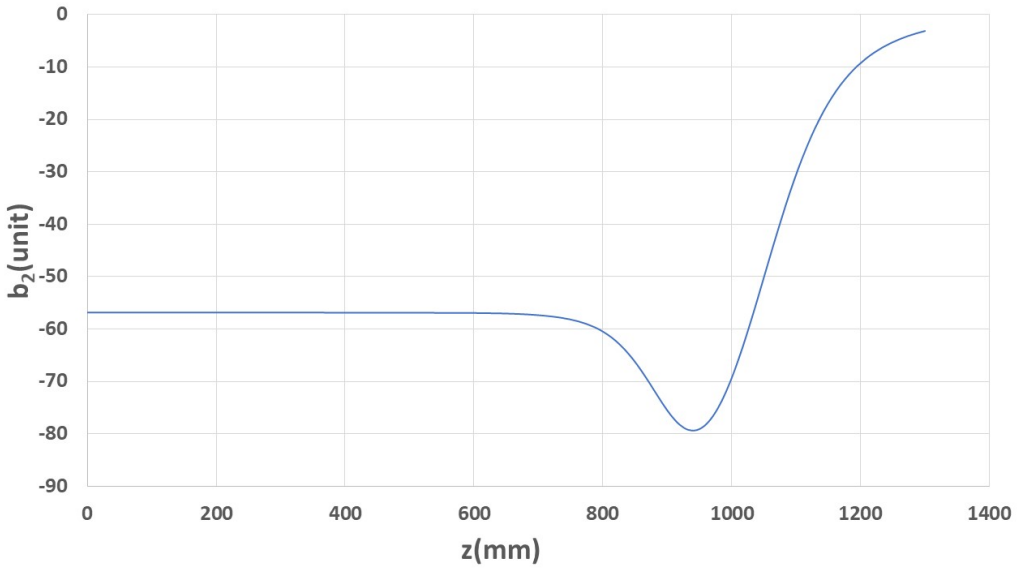

Figure 4.15: The harmonics b_2 as a function of the position along the z-axis for the side opposite to the magnet connections. The iron yoke ends at 890 mm.

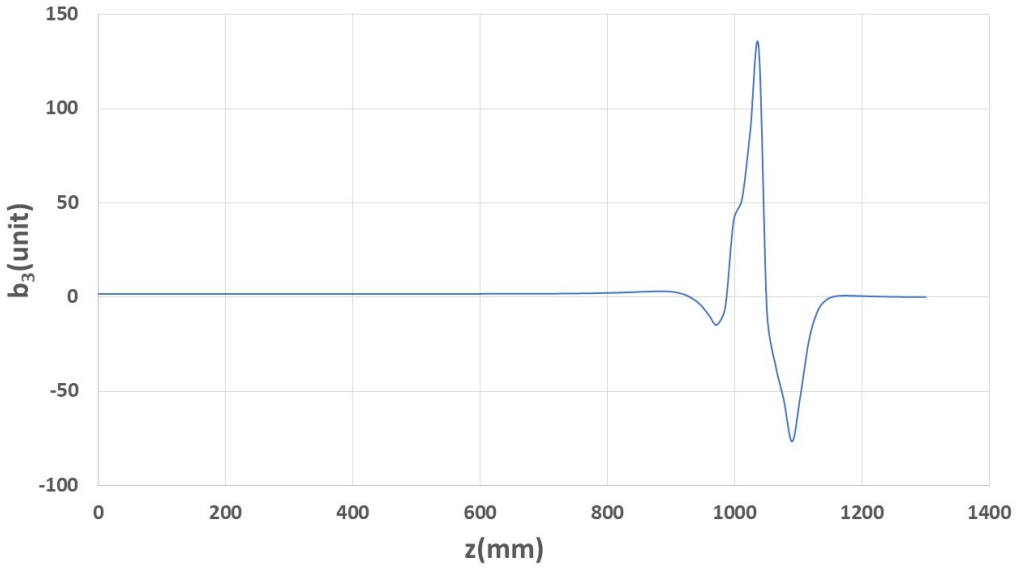

Figure 4.16: The harmonics b_3 as a function of the position along the z-axis for the side opposite to the magnet connections. The iron yoke ends at 890 mm.

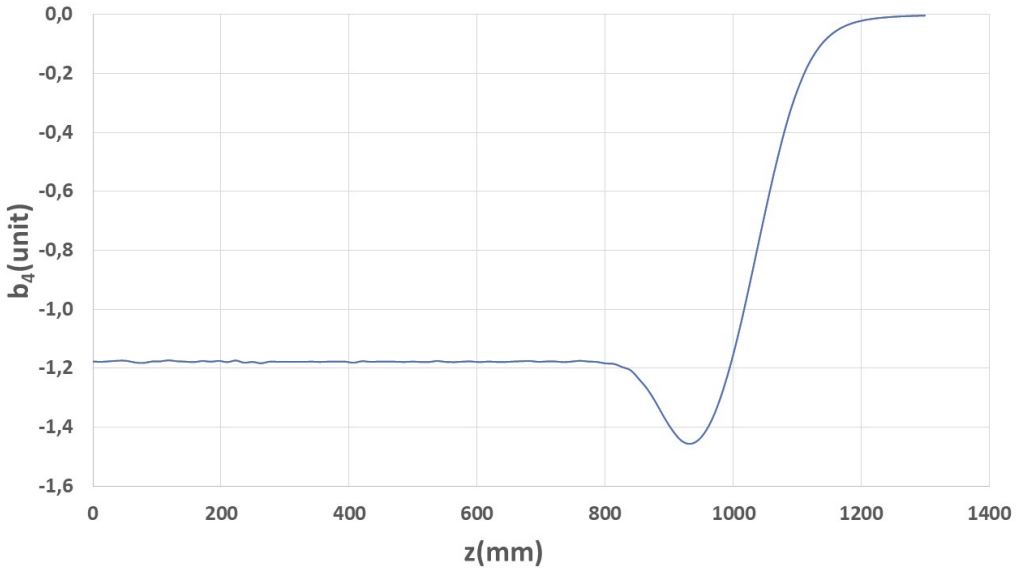

Figure 4.17: The harmonics b_4 as a function of the position along the z-axis for the side opposite to the magnet connections. The iron yoke ends at 890 mm.

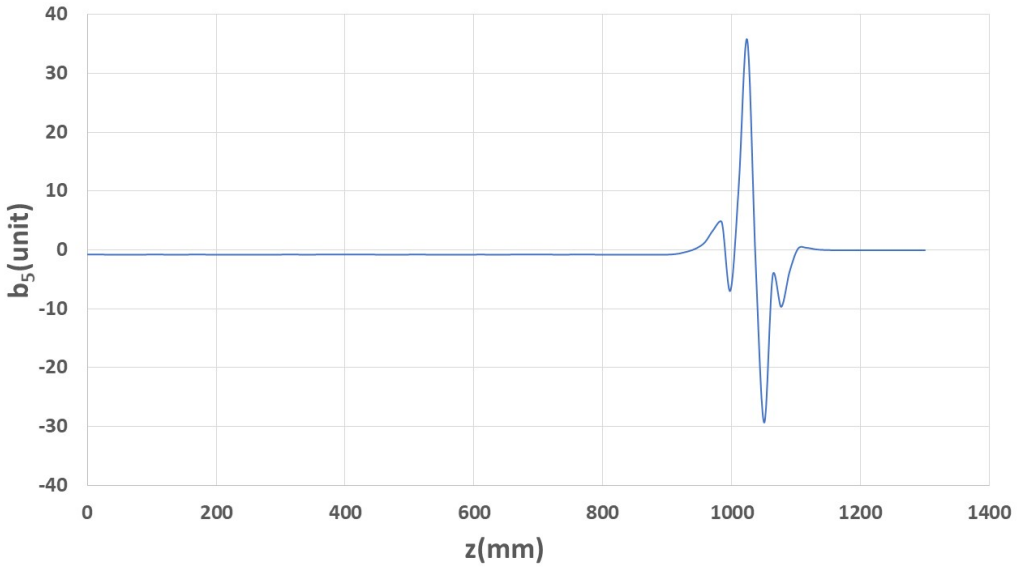

Figure 4.18: The harmonics b_5 as a function of the position along the z-axis for the side opposite to the magnet connections. The iron yoke ends at 890 mm.

Table 4.8: Material mechanical properties at room temperature (RT).

Material	Maximum stress [MPa]	E[GPa]	ν	$\alpha\,[\cdot 10^{-3}]$
Coil	150	$E_x = 30$	0.3	$\alpha_x = 3.1$
		$E_y = 25$		$\alpha_y = 3.4$
Copper wedges	270	100	0.3	3.37
Austenitic steel	350	193	0.28	2.8
Titanium	800	115	0.3	1.7
Iron	230	213	0.28	2.0
Aluminum	480	70	0.3	4.2

Table 4.6. Table 4.7 shows the lower-order normal harmonics at the operating current and integrated over the nominal magnetic length for the magnet with the symmetric coil ends (two sides opposite to the connections). The higher-order integrated normal multipoles are identical at those reported in Table 4.5. Figures 4.14, 4.15, 4.16, 4.17 and 4.18 display the lower-order normal harmonics as a function of the position along the z-axis.

4.2.3 Mechanical design

The Nb_3Sn is an extremely brittle material. There is little experience in how to optimize design criteria for high-field accelerator magnets made with this material. These concern the ideal pre-stress conditions to apply before and during powering, the treatment of interfaces (free, glued, with or without friction) and the maximum allowed strain and stress on the coil. Efforts in that sense are being supported by the development program carried out in the US National Laboratories [29, 33] and by ongoing work being performed at CERN mostly on the 11 T and the MQXF programs [32]. Starting from the above-mentioned experience, it was decided that stress on all materials are limited by their yield strength, except for coils, which are limited by degradation in the critical current (see Tables 4.8 and 4.9).

Concerning the ferromagnetic material (low carbon steel), a limit of tensile stress of $\sigma_1 < 380$ MPa shall be considered at cold. This limit has to be considered as a prudent design threshold: it may change considerably depending on the exact steel composition and on its treatment. At this stage of exploring, the coil must not detach from the pole tip [17]. This is also a conservative constraint, aimed to avoid unwanted movements and consequent quenches in the magnet.

The design proposed is schematically drawn in Fig. 4.19. The conductor

Table 4.9: Material mechanical properties at 1.9 K.

Material	Maximum stress [MPa]	E[GPa]	ν	$\alpha\,[\cdot 10^{-3}]$
Coil	200	$E_x = 33$	0.3	$\alpha_x = 3.1$
		$E_y = 27.5$		$\alpha_y = 3.4$
Copper wedges	> 300	110	0.3	3.37
Austenitic steel	1050	210	0.28	2.8
Titanium	1650	126	0.3	1.7
Iron	720[1]	224	0.28	2.0
Aluminum	690	79	0.3	4.2

[1] 380 MPa is the allowed limit for the first principal stress at cold conditions.

blocks are shown in red. They are separated and sustained by the copper wedges, displayed in orange, and pressed at the pole by titanium tip (in light grey). This structure is inserted in a steel pad, colored in light green, composed of two halves cut horizontally. Then there is the iron yoke, in blue, which is composed of four pieces, cut at 45°, and externally an aluminum alloy shell, in dark grey.

In such a configuration, the Lorentz forces tend to push the coil outward in the radial direction and toward the mid-plane in the azimuthal direction (see Fig. 4.20). This last component of the Lorentz force could cause the detachment of the conductor from the pole, which must be avoided to prevent local heating due to friction and, consequently, quenches. To compensate the Lorentz forces and keep the magnet in position to avoid unwanted movements, a suitable compression must be provided, the so-called pre-stress. Nb_3Sn is brittle, in particular at room temperature, so that giving the necessary pre-stress is a delicate issue. The well-known collaring system is not suitable, because it would give all the compression at room temperature, producing a too high level of stress in the conductor. Another method is the so-called *bladder & keys*, which has been already investigated in several works [10, 32], but is however quite innovative, since it has not been used yet in any magnet in present accelerator machines. The working principle is the following: aluminum bladders are inserted in the gap between the steel pad and the iron yoke and inflated by pressurized water, allowing the insertion of some keys, whose thickness is greater than the nominal gap between the two components. At that point, the bladders are deflated and removed from the gap. The interference between the keys, the pad and the yoke compresses the winding and generates the pre-load at room temperature. When the system is cooled down, the aluminum outer ring shrinks more than the inner

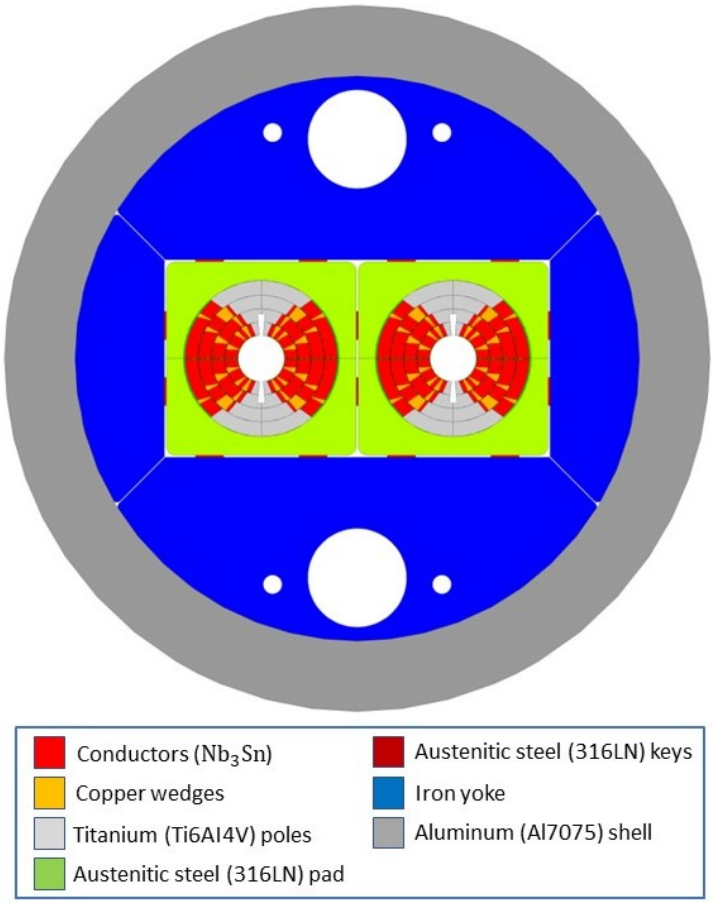

Figure 4.19: Layout of the cold mass.

components, giving an additional compression to the system. This method allows to give only a part of the pre-stress at room temperature, when the conductor is more brittle, and the remaining part at cryogenic temperature. Most of the geometrical parameters, such as the dimension and the shape of the steel pad, the dimension and position of the keys, the position of the cut in the iron yoke and the thickness of the aluminum shell were obtained by several iterations of optimization. Also the shape of the titanium pole is the result of extensive analysis. The notch in the first two layers allows to keep the contact between the conductor and the pole even after the energization. In fact, in this way, the pole behaves like a spring, which is compressed during assembly and cool down, and releases after the powering.

The problem was studied using the finite element analysis (FEA) ANSYS code [71]. The FEA model represents a quarter of the entire magnet, with proper boundary conditions. The contact elements between the four layers of

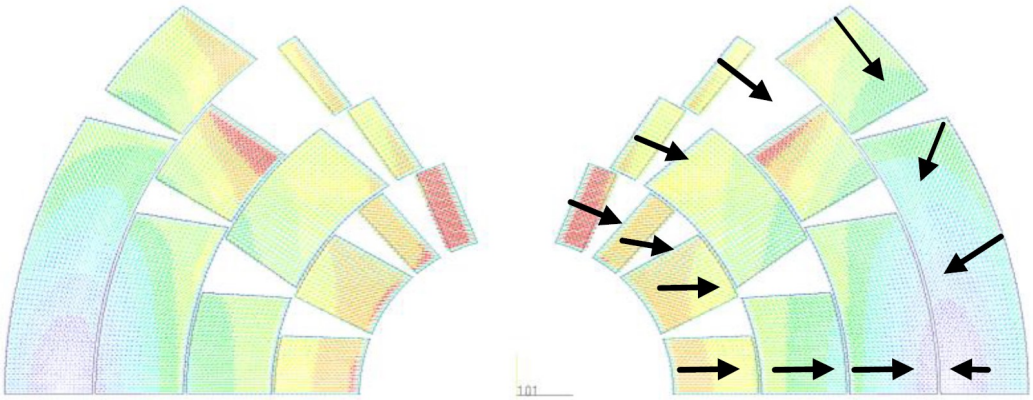

Figure 4.20: The Lorentz forces tend to push the coil outward in the radial direction and toward the mid-plane in the azimuthal direction.

conductors simulate a glued structure, while the fourth layer of the winding is in contact with the steel pad but can also slide with a friction coefficient of 0.28. The keys are glued to the pad, while sliding is permitting at their interference with the iron yoke. The aluminum shell can slide with respect to the yoke, and can also detach. The results of this configuration are reported in Fig. 4.21.

In the first row, the contact pressure between the pole and the conductor is shown for the three main steps, i.e., assembly, cooling down and energization. As can be seen, the contact pressure is very good in the first two phases, thanks to the bladder and key pre-stress, while it decreases after the powering of the magnets, remaining thus at an acceptable level. In the second row, the Von Mises (VM) stress in the conductor is displayed for the same three steps, showing that the constraints on the stress limit are fulfilled. The most critical step is the cooling down, where a hot spot of 211 MPa can be noticed at the edge in the third layer, though it is very localized and could be considered acceptable. Also the stress on the mechanical structures was studied in detail.

In Figures 4.22,4.23 and 4.24, the Von Mises (VM) stress on the steel pad, the iron yoke, the aluminum ring and the titanium pole are shown for the three main steps. Unavoidable hot spot very localized can be noted under the keys, where both the pad and the yoke undergo plasticization, though they do not affect the effectiveness of the structure.

During the assembly, the titanium pole presents a small region where the stress exceeds the yield, but this issue could be avoided with a finer optimization of the shape of the notch. After energization, the upper part of the iron yoke detaches of about 0.3 mm from the aluminum ring. To

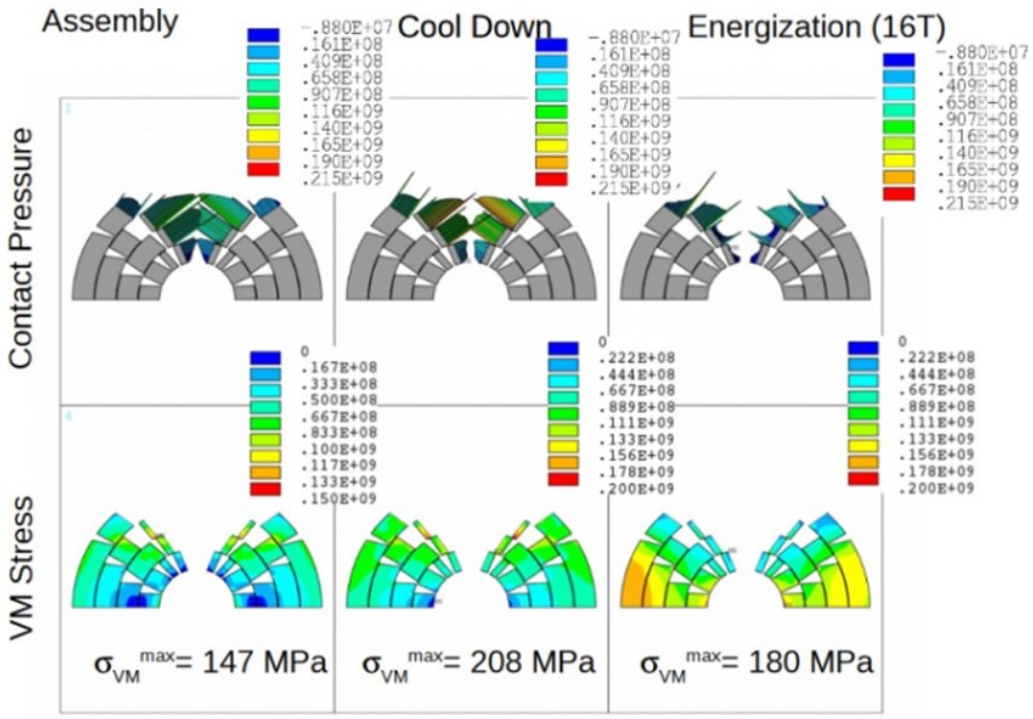

Figure 4.21: On the first row, contact pressure between conductor and pole at assembly (left), cooling down (center) and energization to 16 T (right). On the second row, Von Mises (VM) stress for the same three steps.

avoid this detachment, different configurations for the iron yoke, composed of only two pieces and cut horizontally or vertically in the middle, were also investigated. This configuration, though, makes the insertion of the keys unfeasible, requiring an unbearable bladder pressure. The solution found is then satisfying from the mechanical point of view and fulfilling all the previously cited constraints.

4.2.4 Quench protection

The quench protection is a challenging aspect due to the large energy stored in the magnet. Therefore, accurate studies were performed during the design phase [36, 37, 52, 63, 65]. For making a fair comparison between the four magnet options, the EuroCirCol collaboration defined the following rules for the quench protection: the protection system has 20 ms to detect the quench and other 20 ms to activate itself. Considering a quench with the 105% of the operating current, the magnet is considered acceptable if the hot spot temperature ($T_{\text{hot spot}}$) is below 350 K and the maximum voltage

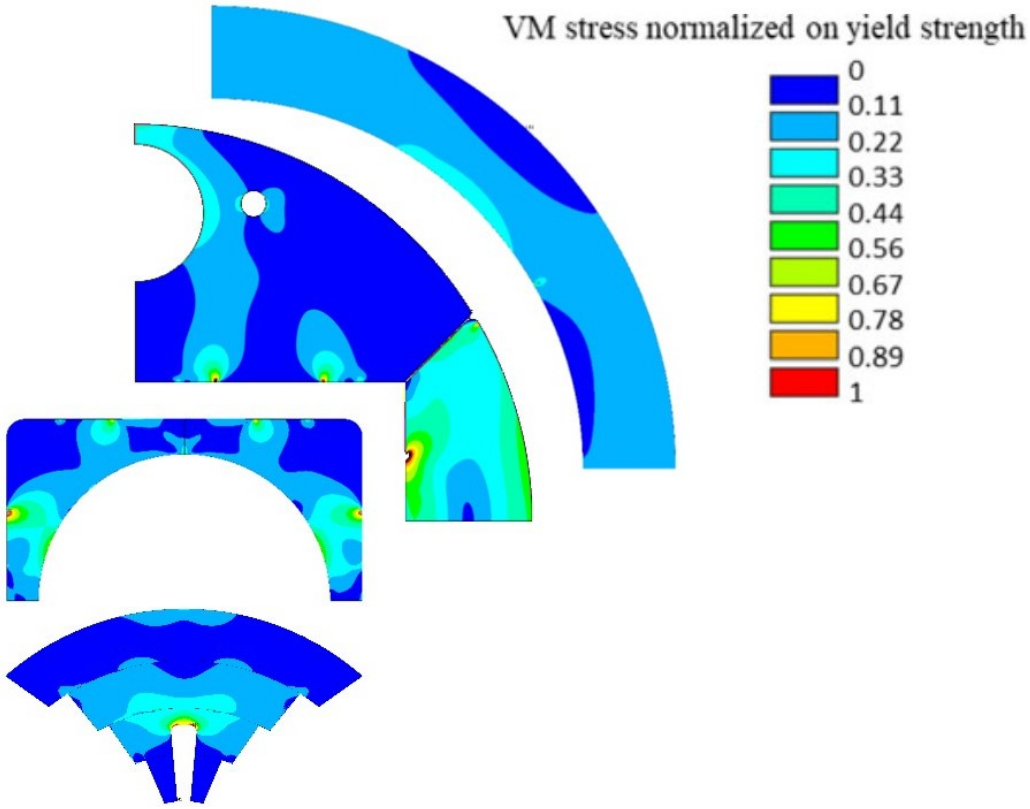

Figure 4.22: Von Mises stress on mechanical structures normalized to their yield strength at room temperature (RT) after assembly.

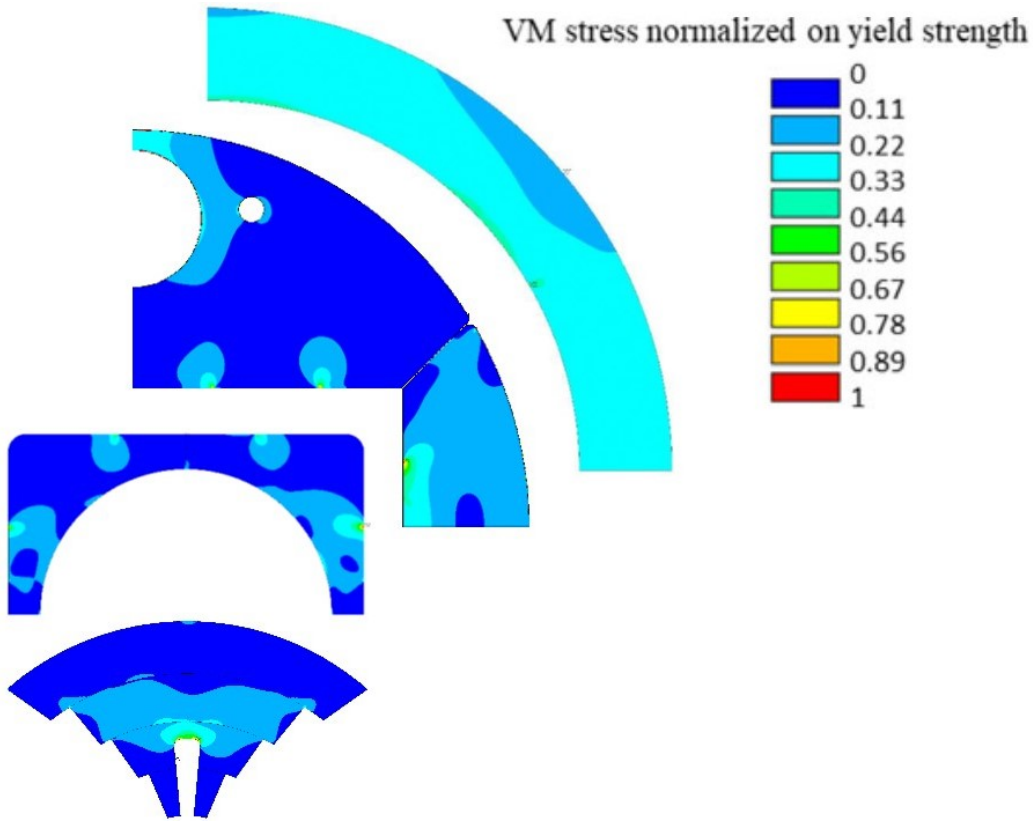

Figure 4.23: VM stress on mechanical structures normalized to their yield strength after cooling down.

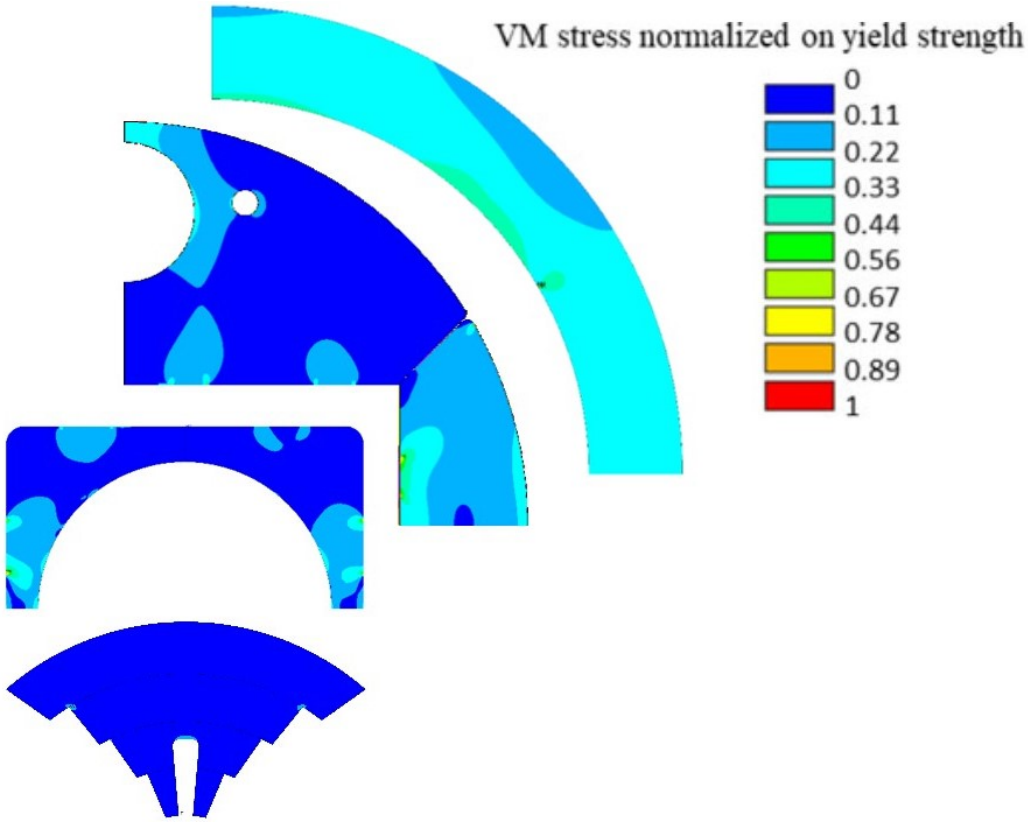

Figure 4.24: VM stress on mechanical structures normalized to their yield strength after energization to 16 T.

Table 4.10: Quench simulation results.

Devise option	$T_{\text{hot spot}}$(K)	V_{ground}(V)
QH	322	870
CLIQ	286	800

toward ground (V_{ground}) is below 1.2 kV. These values were determined by the HL-LHC experience with Nb_3Sn [26]. In the case of the $\cos\theta$ magnet, the quench protection analysis was performed considering Quench Heaters (QH) or Coupling-Loss Induced Quench system (CLIQ). Both of them allow to satisfy the above requirements. The results are summarized in Table 4.10.

4.3 Baseline design with asymmetric coil

4.3.1 Design parameters

Studies on the beam dynamics showed that an integrated quadrupole harmonics of about 65 units at the nominal current and its variation on the ramp greater than 40 units are not acceptable for the bending dipole. Therefore, the EuroCirCol collaboration decided to increase the inter-beam distance and the iron yoke diameter to 250 mm and 660 mm respectively for reducing as much as possible the cross-talk effect.

Furthermore, for mechanical purpose, the iron yoke is enclosed in an aluminum alloy shell, 50-mm thick, to provide the additional pre-stress in coils during the cool down. Besides, everything is bound together by a steel shell, 20-mm thick, which works as a vessel. The whole cold mass diameter is 800 mm. Taking into account that in the LHC tunnel the maximum outer cryostat diameter must be 1215 mm, the cold mass is compatible for the high-energy upgrade of LHC (HE-LHC). Table 4.11 shows the new design parameters.

With respect to the previous magnet design, the EuroCirCol collaboration decided to add some requirements for the 3D model: the length of each coil end must be within 300 mm and the peak field in the head must be at least 0.2 T lower than in the straight part.

Table 4.11: Main design parameters.

Feature	Unit	Value
Material		Nb_3Sn
Bore magnetic field	T	16
Magnetic length	m	14.3
Aperture diameter	mm	50
Beam distance	mm	250
Iron yoke outer radius	mm	330
Operating temperature	K	1.9
Operating point on load-line	%	86
Cu/non-Cu		≥ 0.8
Maximum no. of strands		40
Field harmonics (geom/sat)	unit	$\leq 3/10$
Number of apertures		2

4.3.2 Magnetic design

2D model

According to the new design parameters, we increased the iron yoke diameter and the inter-beam distance of the previous configuration. We obtained the cold mass cross-section shown in Fig. 4.25. The field quality of this layout is not yet satisfactory, because of the wide b_2 and b_3 values at the injection and collision energy (see Fig. 4.27). We studied different shapes of the iron yoke to minimize the harmonics variation during the ramp. The final result is shown in Fig. 4.25. The iron insert between apertures works as a pole and can decrease the b_2 variation from 35 units to 6 units (see Fig. 4.28). Nevertheless, an offset of about -35 units remains, which can not be eliminated by iron shaping only. Therefore, we decided to compensate for the cross-talk effect, breaking the left-right symmetry in the cross-section of each coil. The asymmetric configuration has been achieved in two different ways. On one hand, starting from the symmetric design described in section 4.2.2 we changed the angular positions and the tilt angles of each block by using the local ROXIE optimizer, named Extreme algorithm. On the other hand, we reconsidered the whole design on the basis of the developed analytic approach and looked for new coil configurations (see section 4.4).

Both methodologies found the coil cross-section shown in Fig. 4.30. The minimum tip thickness of the wedge in contact with the mandrel is 0.74 mm, located between the first and second block of the first layer on the right side

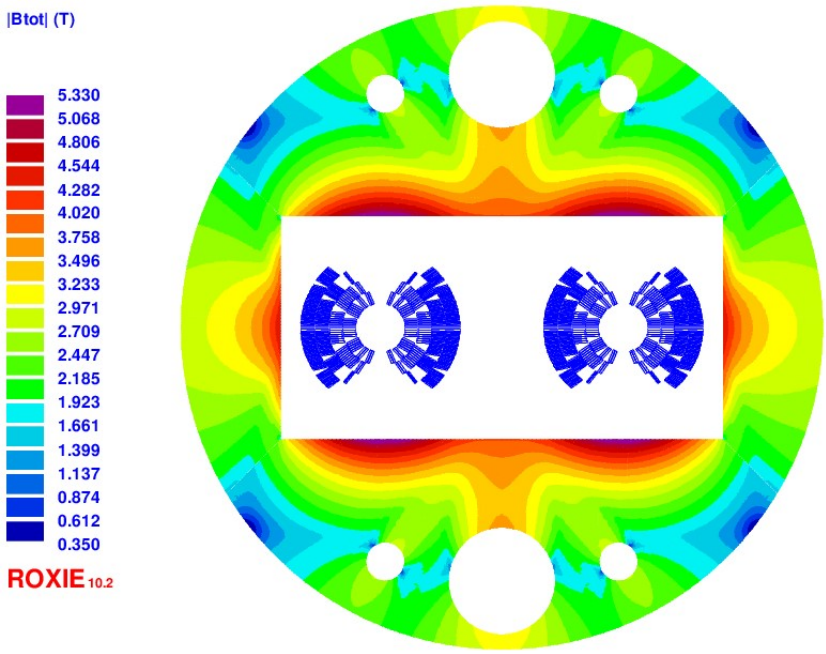

Figure 4.25: Iron yoke before the optimization. The magnetic field is shown at the operating current.

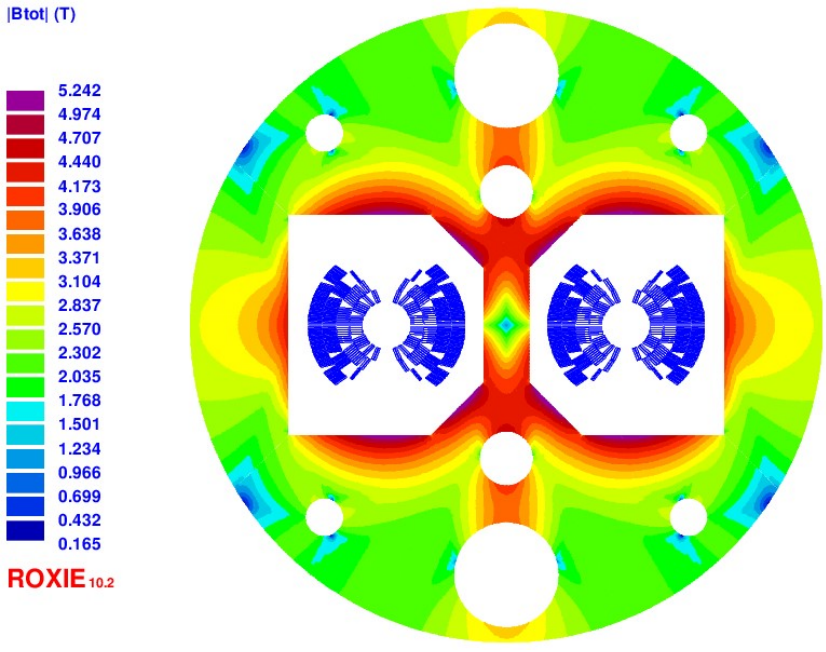

Figure 4.26: Iron yoke after the optimization. The magnetic field is shown at the operating current.

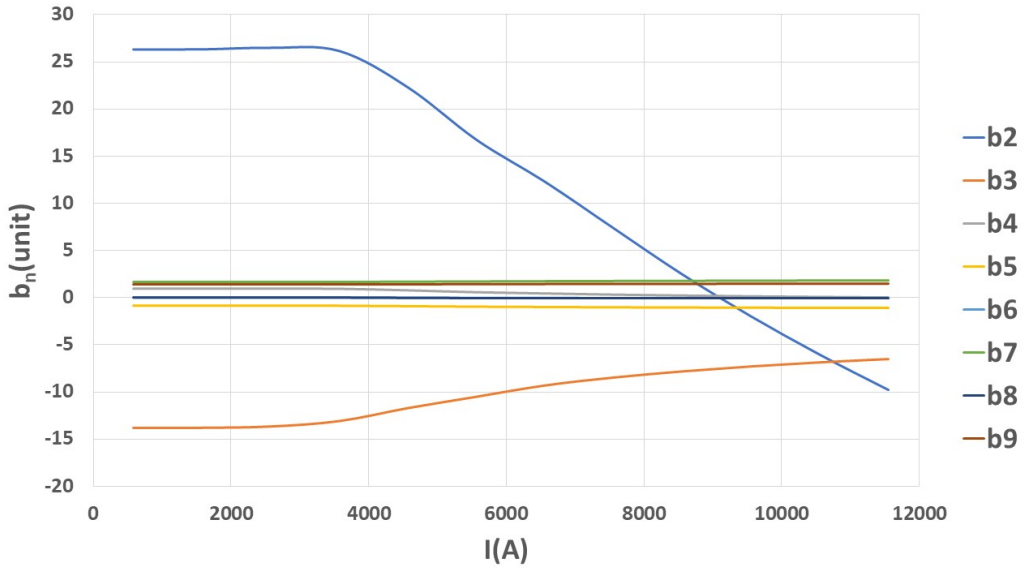

Figure 4.27: Field quality with the previous iron yoke design (see Fig. 4.25) and the symmetric coil configuration.

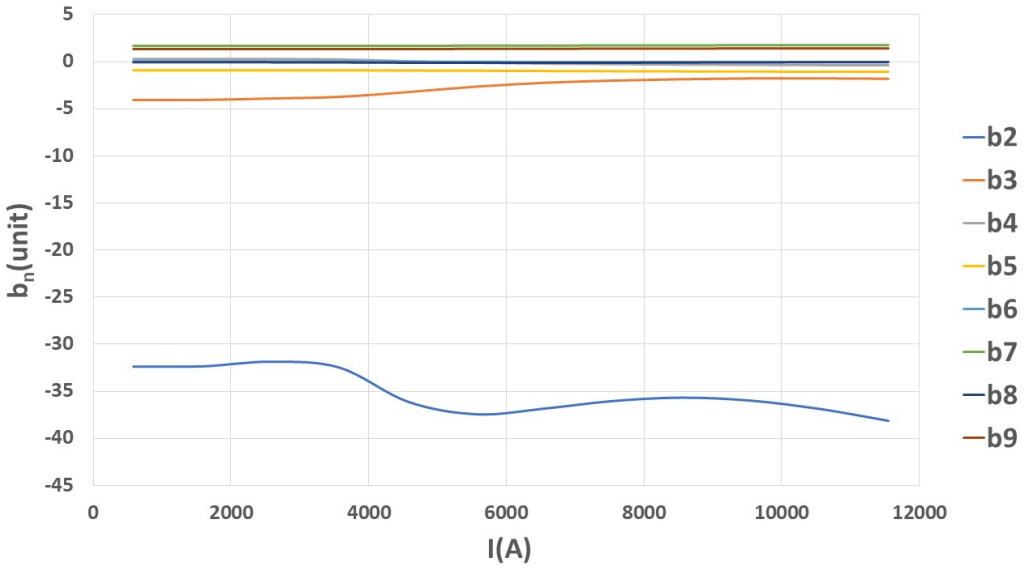

Figure 4.28: Field quality with the new iron yoke design (see Fig. 4.26) and the symmetric coil configuration.

Table 4.12: Lower-order normal harmonics at the operating current.

b_2	b_3	b_4	b_5	b_6	b_7	b_8	b_9	b_{10}
0.01	0.22	0.31	0.17	0.35	0.19	0.37	0.57	0.13

Table 4.13: Higher-order normal harmonics at the operating current.

b_{11}	b_{12}	b_{13}	b_{14}	b_{15}	b_{16}	b_{17}	b_{18}	b_{19}	b_{20}
1.1	0.09	−0.24	0.03	−0.02	0	−0.06	0	0	0

of the aperture. The conductor parameters are the same as the previous conceptual design, but the operating current has been increased to 11.44 kA to restore the bore field to 16 T. The operating point on the load-line remains at the 86% both for the low-field and high-field cables, i.e., within the minimum value determined by EuroCirCol collaboration (see Table 4.11). The peak field (16.4 T) on the high-field conductor is localized on the fourth block of the first layer in the coil side facing the other coil (the left side of the coil in Fig. 4.30). The peak field (12.7 T) on the low-field conductor is situated on the third block of the third layer in the coil side facing the external part of the iron yoke (the right side of the coil in Fig. 4.30).

The asymmetric coil allows to remove the b_2 offset. Now, the field quality fulfills any requirement. In fact, at the injection energy the harmonics are far below the threshold of 10 units, and at the collision energy they are not far from zero (see Fig. 4.29 and Tables 4.12 and 4.13).

3D model

The changes in the cross-section and the new constraints on the coil ends have required a new design of the side opposite to the connections (see Fig. 4.31). In the new mechanical design, the pole is common for all layers (see Fig. 4.42). So, to ensure that there are no uncompressed parts, all layers begin to bend nearly in the same longitudinal position (see Fig. 4.32). The solution adopted in the old design to reduce the peak fields in the heads is not practicable. For avoiding to space too much the blocks we have chosen to draw back the iron yoke with respect to the straight part. The coil extremity begins 40 mm after the end of the yoke. The minimum longitudinal distance between the blocks is about 5 mm and the maximum roughly 31 mm. The EuroCirCol collaboration considers reasonable these values, which will have to be confirmed through the 3D mechanical simulations. With respect to the previous

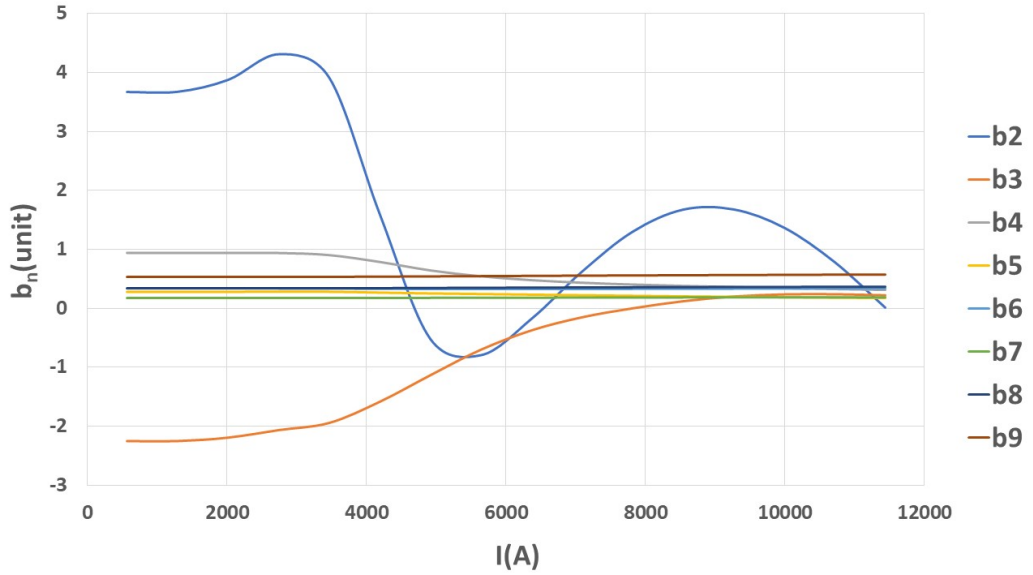

Figure 4.29: Field quality with the new iron yoke design (see Fig. 4.26) and optimized asymmetric coil arrangement (see Fig. 4.30).

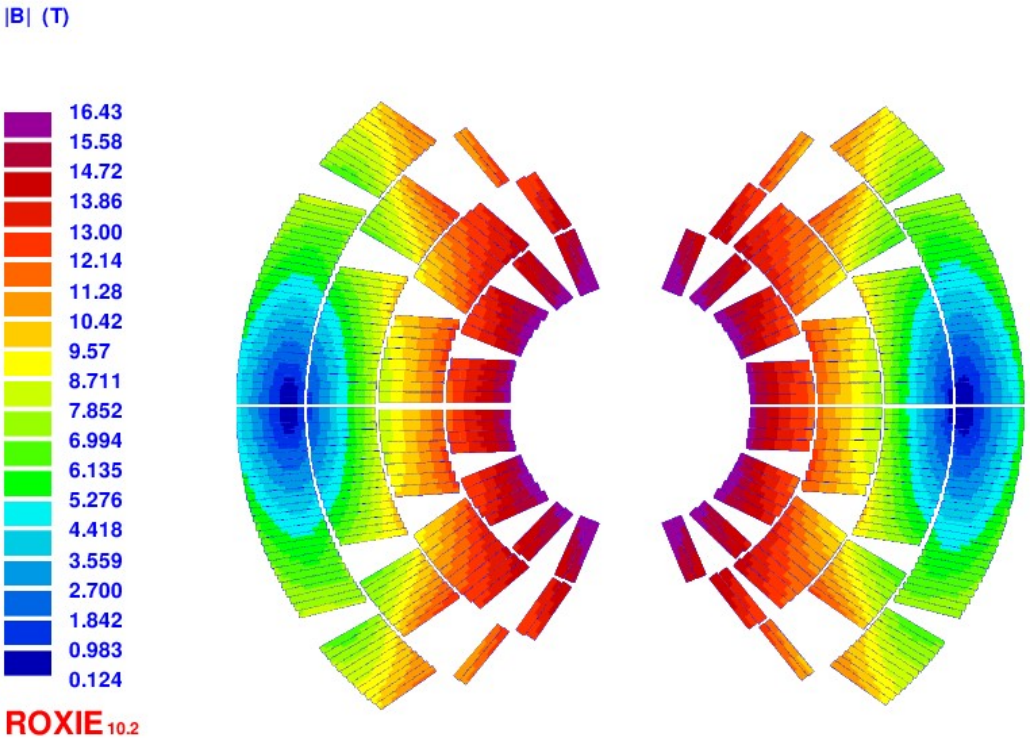

Figure 4.30: Asymmetric coil cross-section. The magnetic field is shown at the operating current.

Table 4.14: Peak fields on the conductors at the operating current in the side opposite to the connections.

Conductor	Cross-section (T)	Coil end (T)	ΔB_{peak} (T)
LF	12.7	12.5	0.2
HF	16.4	15.4	1

Table 4.15: Lower-order normal harmonics at the operating current and integrated over the nominal magnetic length for the magnet with the symmetric coil ends (two sides opposite to the connections).

$\bar{b}_2$	$\bar{b}_3$	$\bar{b}_4$	$\bar{b}_5$	$\bar{b}_6$	$\bar{b}_7$	$\bar{b}_8$	$\bar{b}_9$	$\bar{b}_{10}$
−0.6	−0.65	0.32	0.17	0.35	0.18	0.37	0.57	0.13

head design, we have removed all cross-section block divisions to make the head as compact as possible. The experience in magnet design teaches that the more compact the head, the easier the mechanical design. Since such a coil has never been made, the collaboration decided to postpone any block splits until after the mechanical simulations. Now, the extremity is 152 mm long, far below the requirements of the EuroCirCol collaboration.

The peak fields in the high and low field regions have been computed by using ROXIE and Opera. The values obtained are reported in Table 4.14. Both codes have confirmed that the peak fields in the straight part are higher than in the coil end. In particular, they have shown that in the first layer the peak field strongly decreases in the coil extremity, dropping from 16.4 T in the straight part to 15.4 T at the beginning of the bend (see Fig. 4.34). In the third layer, the field decrease is less pronounced (see Fig. 4.35).

Table 4.15 shows the lower-order normal harmonics at the operating current and integrated over the nominal magnetic length for the magnet with the symmetric coil ends (two sides opposite to the connections). The higher-order integrated normal multipoles are identical at those reported in Table 4.13. Figures 4.36, 4.37, 4.38, 4.39 and 4.40 display the lower-order normal harmonics as a function of the position along the z-axis.

4.3.3 Mechanical design

The optimization of the field quality required a certain number of modifications, the main one being the increase of the inter-beam distance from 204 mm to 250 mm, to reduce the magnetic cross-talk between the two

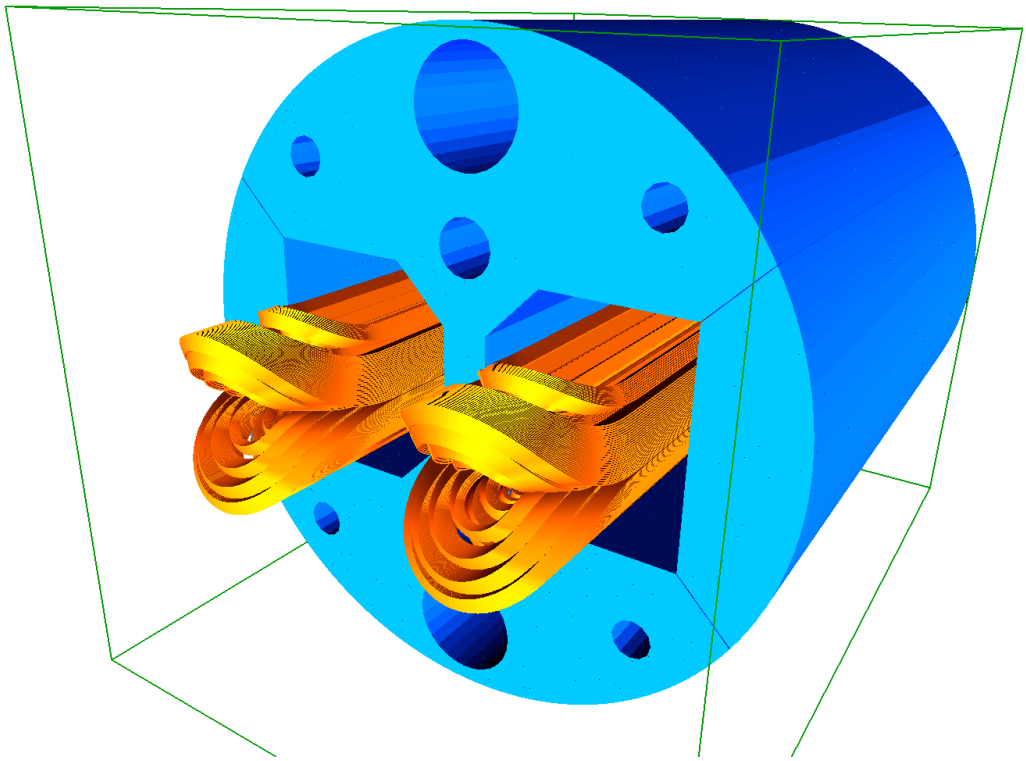

Figure 4.31: Side opposite to the magnet connections in ROXIE. The coils are in yellow and the iron yoke in blue.

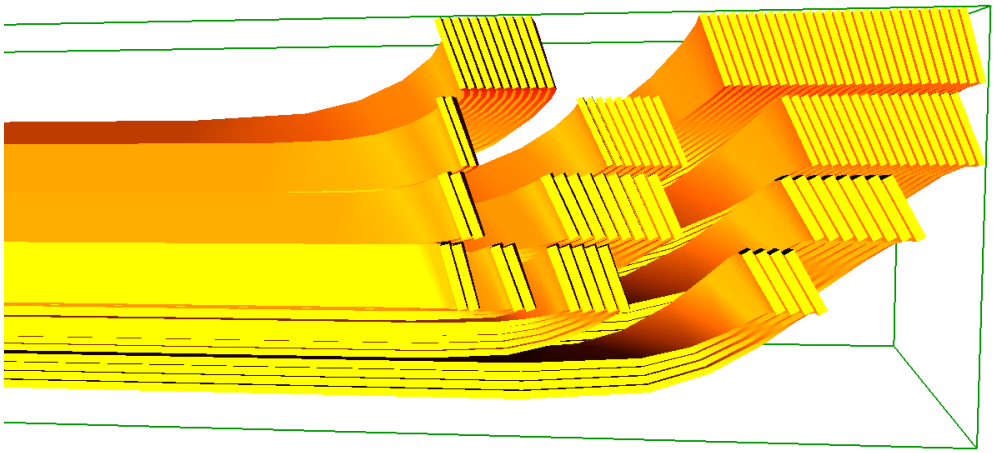

Figure 4.32: Section of the side opposite to the connections in ROXIE. The peak fields are in the leftmost blocks of the first and third layer. Their values are reported in Table 4.14.

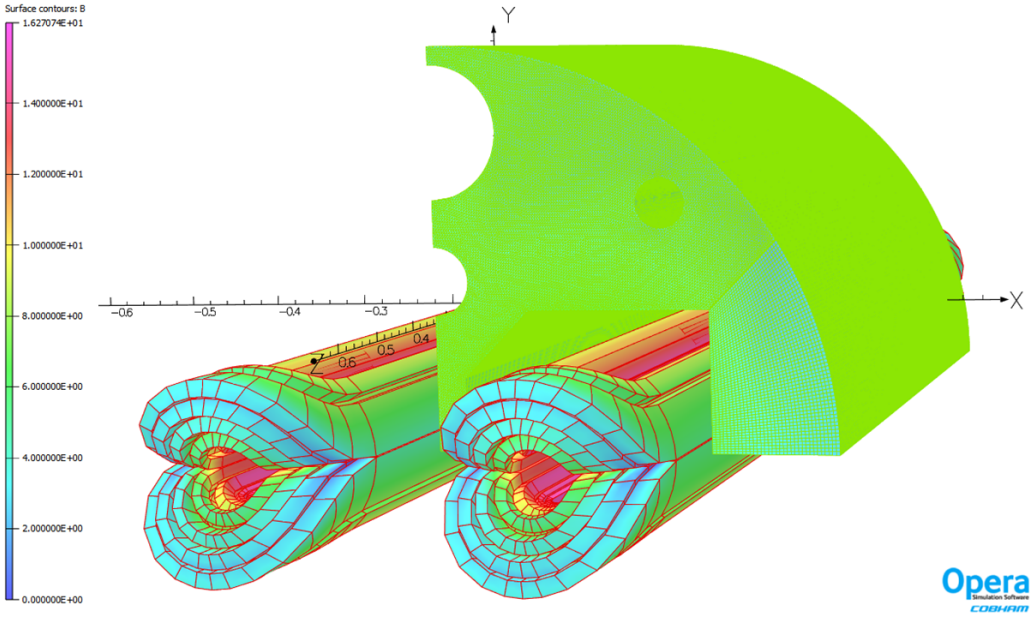

Figure 4.33: 3D electromagnetic model in Opera with the symmetric coil ends (two sides opposite to the connections). The magnetic field is shown at the operating current.

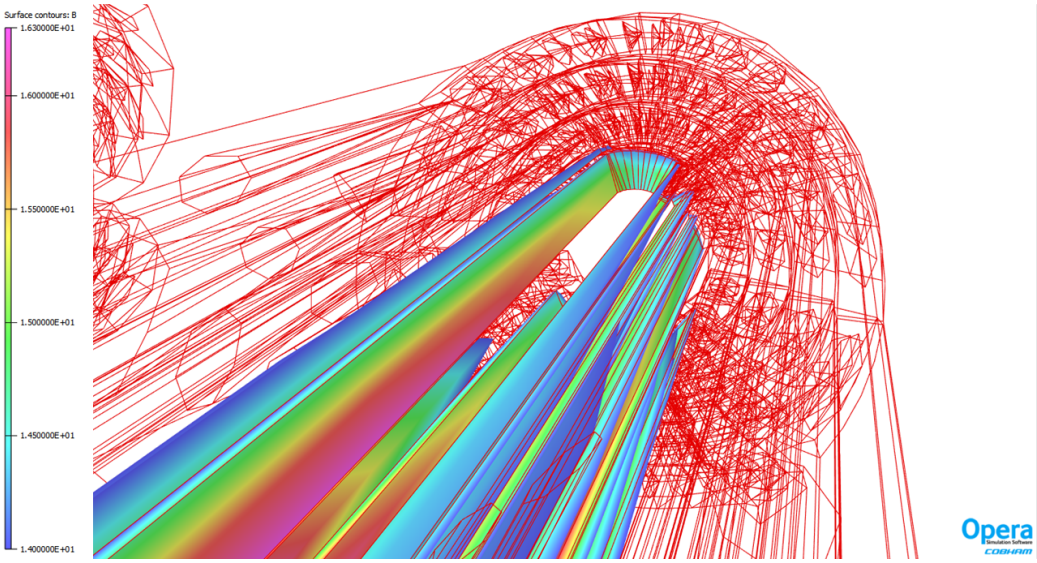

Figure 4.34: Magnetic field at operating current in the first layer of the side opposite to the magnet connections.

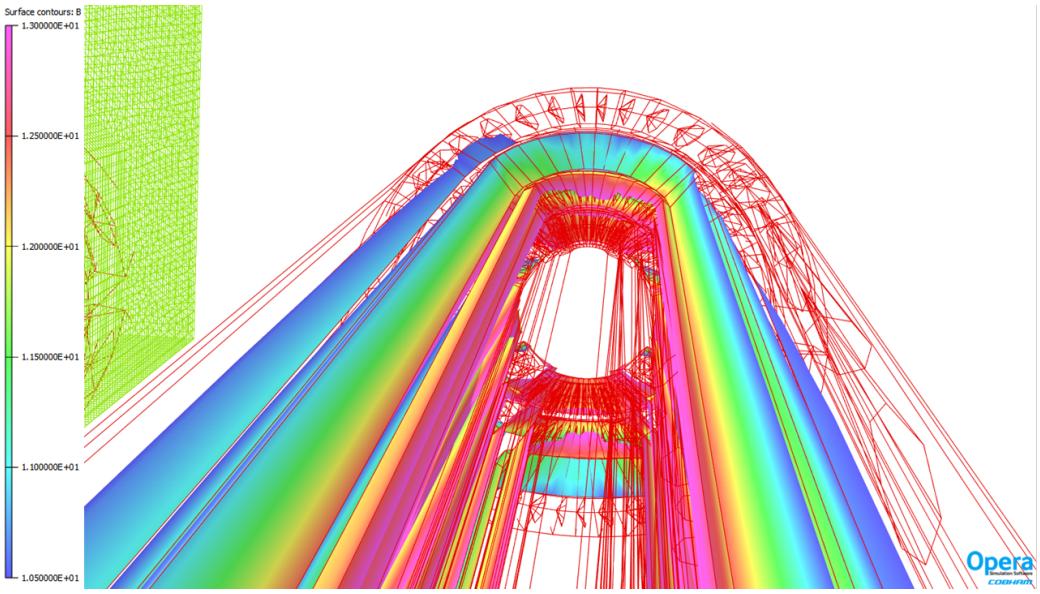

Figure 4.35: Magnetic field at operating current in the third layer of the side opposite to the magnet connections.

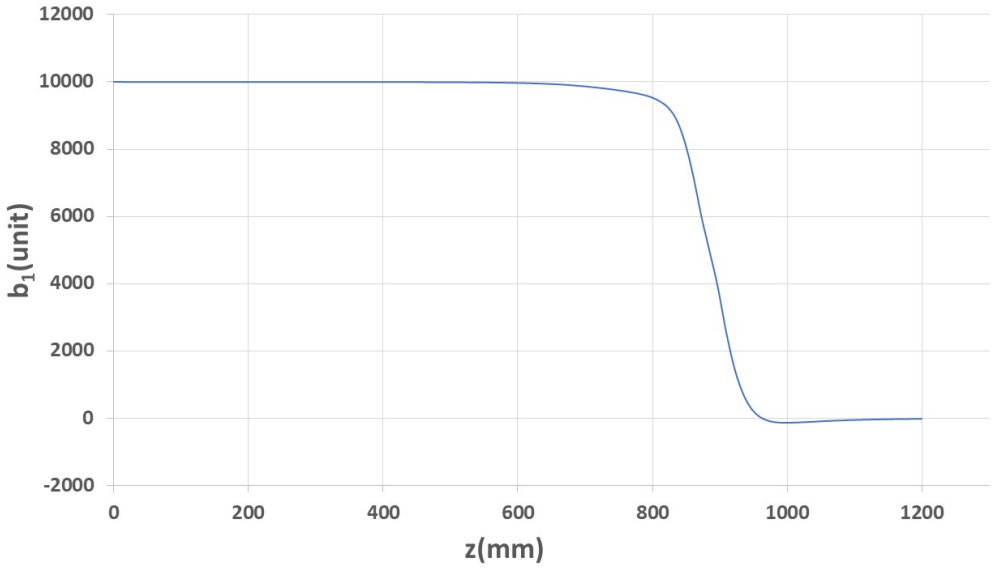

Figure 4.36: The harmonics b_1 as a function of the position along the z-axis for the side opposite to the magnet connections. The iron yoke ends at 750 mm.

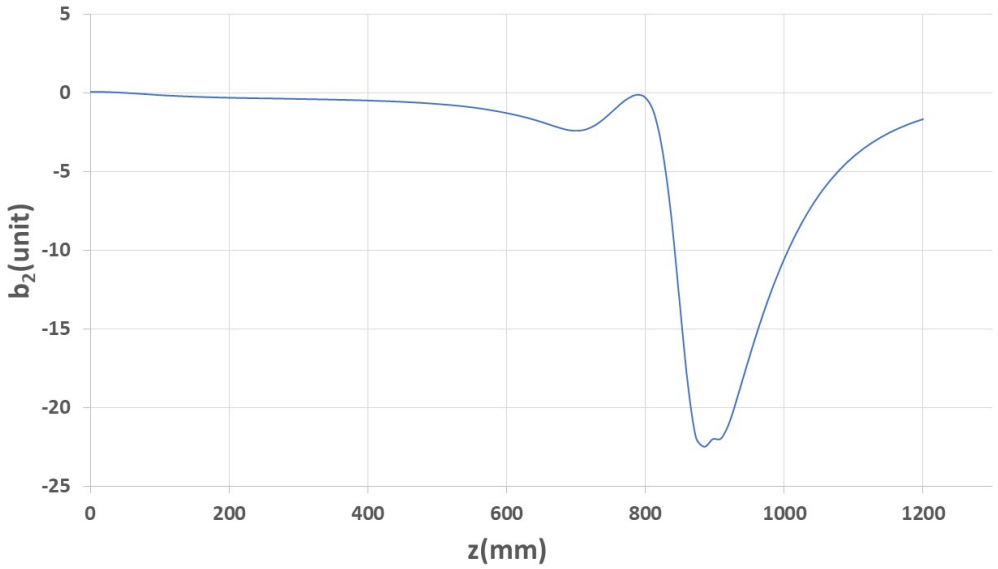

Figure 4.37: The harmonics b_2 as a function of the position along the z-axis for the side opposite to the magnet connections. The iron yoke ends at 750 mm.

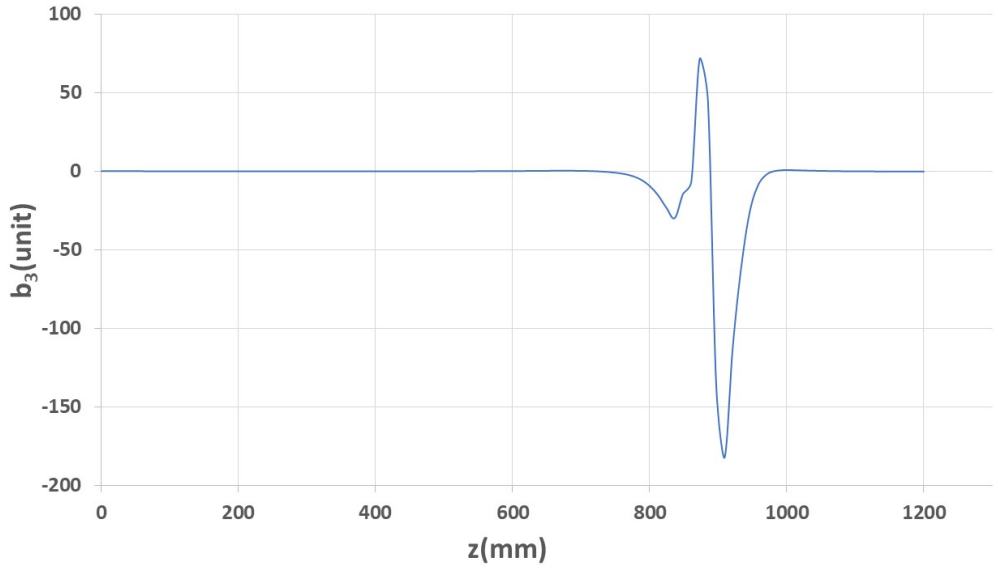

Figure 4.38: The harmonics b_3 as a function of the position along the z-axis for the side opposite to the magnet connections. The iron yoke ends at 750 mm.

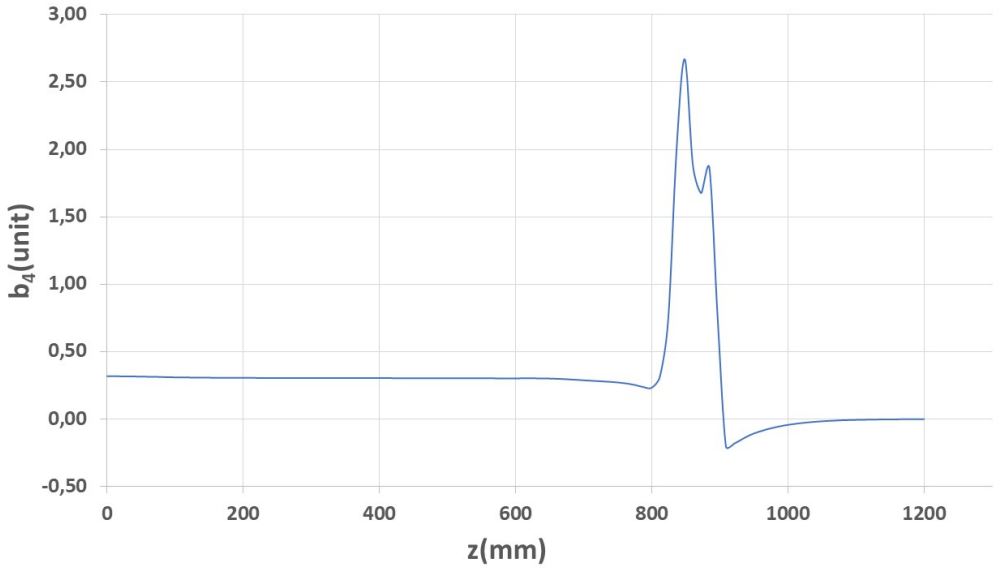

Figure 4.39: The harmonics b_4 as a function of the position along the z-axis for the side opposite to the magnet connections. The iron yoke ends at 750 mm.

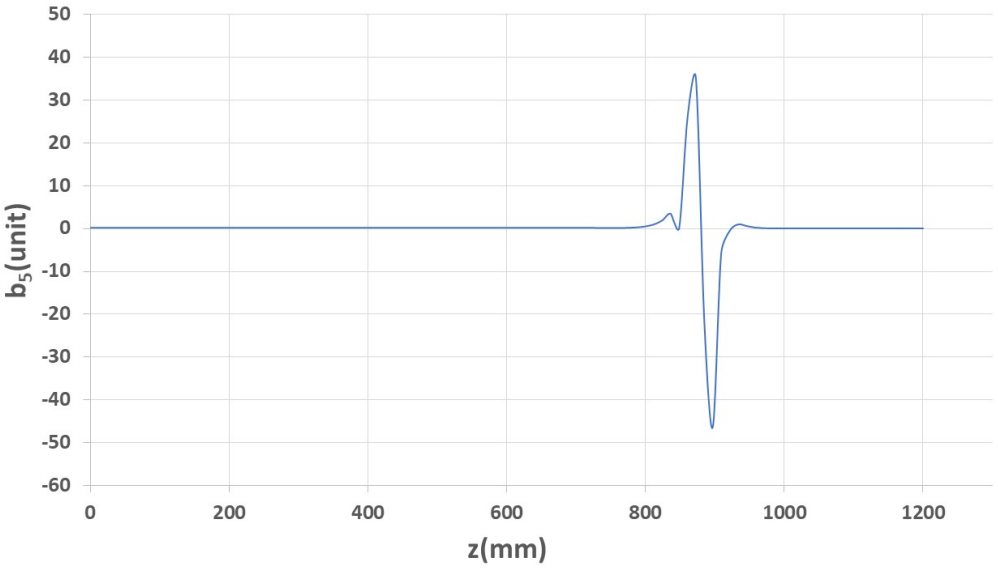

Figure 4.40: The harmonics b_5 as a function of the position along the z-axis for the side opposite to the magnet connections. The iron yoke ends at 750 mm.

apertures. This main modification, besides the requirement of keeping the compatibility with the LHC tunnel, leads to several changes in the design, as it can be seen from the comparison between Fig. 4.19 and Fig. 4.41. The main modifications are listed below:

1. an iron wall with a particular pole shape was added between the two apertures, to optimize further the field quality;

2. the outer diameter of the iron yoke was enlarged from 600 mm to 660 mm, to accommodate the new inter-beam distance;

3. the thickness of the aluminum ring was reduced from 70 mm to 50 mm to make the magnet more compact and keep the compatibility with the LHC tunnel;

4. a loading plate (i.e., a flat stainless steel sheet aligning all the four layers) was introduced to give pre-compression to the coil more uniformly and efficiently, and the shape of the titanium pole was modified accordingly.

The outer stainless steel shell is soldered under compression, so to compensate the thickness reduction of the aluminum shell in the new baseline design. When the system is cooled down, the aluminum shell shrinks more than the inner components, giving additional pre-stress. In this way, most of the pre-compression is given at cryogenic temperatures, where Nb_3Sn exhibits better mechanical properties. Fig. 4.42 shows an enlargement of the keys region, with indication of bladder positions. Due to the irregular pad/yoke shape, the inner vertical key has no interference; the total interference has been attributed to the right vertical key and corresponds to 1.2 mm. The bladder pressure needed to open those interference gaps is 60 MPa. The horizontal keys are much less critical, having an interference of only 0.2 mm.

A mechanical model was prepared with FE code ANSYS [71] including all the relevant geometrical details. The material properties for the structural components are listed in Tables 4.8 and 4.9. The four layers are assumed to be glued together, including the wedges. This possibly implies that the four layers are impregnated together, but to definitely set how to construct and assemble the two double pancakes an intense R&D activity has been funded and is foreseen in the next years. The coil and the titanium pole can slide (with a friction coefficient of 0.2) and detach from each other. The same kind of contact surfaces were also defined between the keys, the iron yoke, the aluminum ring and the steel shell. The simulation reproduces the

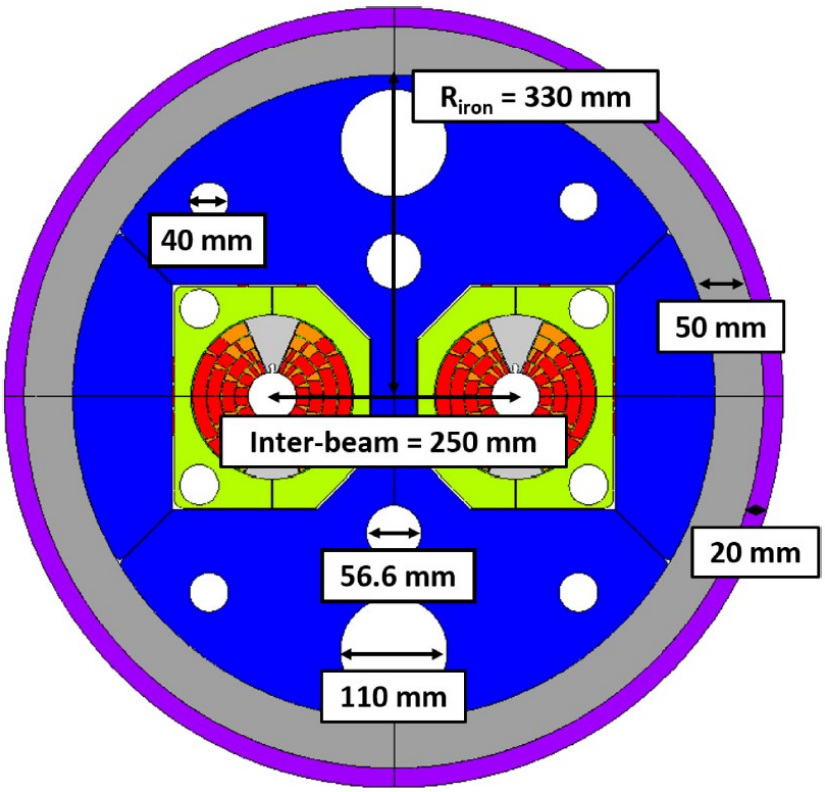

Figure 4.41: Main dimensions of the baseline design published in the CDR.

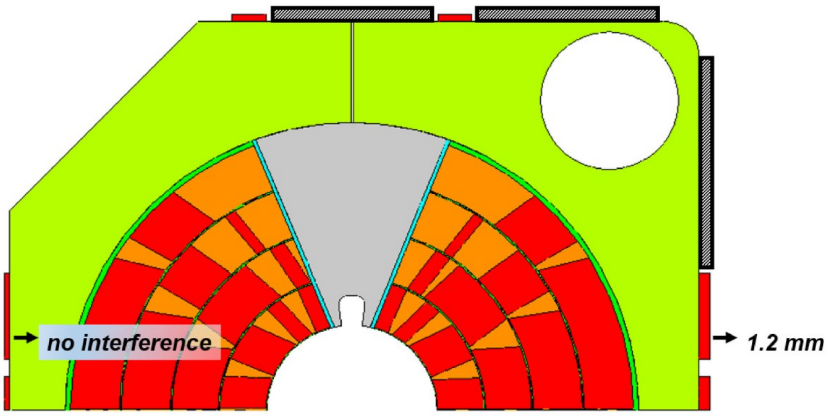

Figure 4.42: Enlargement of the keys region, with indication of bladder positions.

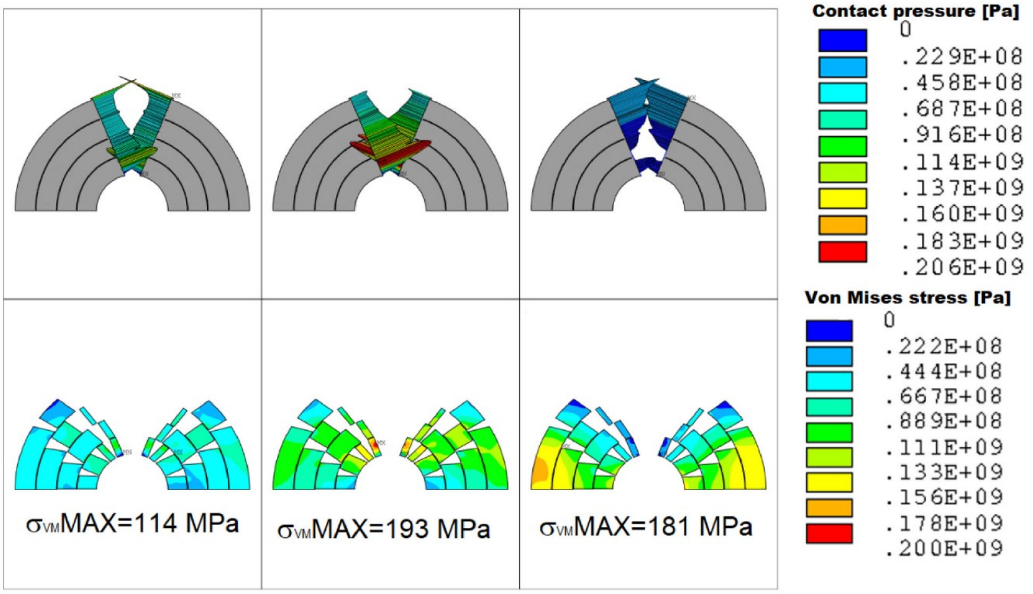

Figure 4.43: Contact pressure between the coil and the pole (upper row) and Von Mises stress in the conductor (lower row) after assembly (left), cool down (center) and energization to 16 T (right).

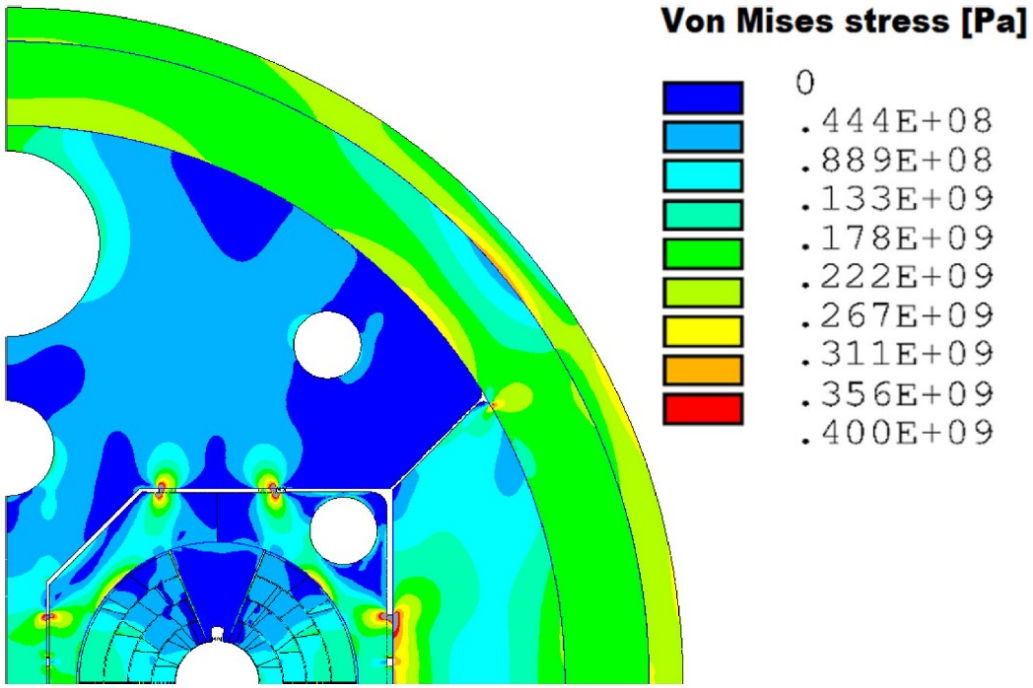

Figure 4.44: Von Mises stress in the structural components after energization to 16 T.

following three main steps: the assembly of the magnet, which includes the insertion of the keys and the closing of the steel shell in pressure, the cool down and the energization to 16 T. The results regarding the VM stress in the conductor and the contact pressure between the coil and the pole are shown in Fig. 4.43: the stress is below the acceptable limit in all the calculation steps. The requirements on the pole-coil contact pressure are also satisfied. As the coil are not glued to the pole, a small gap of 2 µm opens in that region, but it can be considered negligible. The asymmetry in the coil position does not introduce any issue from the mechanical point of view. The radial displacement of the mid-plane turns goes from −85.6 µm to 226 µm from energization to cool-down and this can be taken into account during the coil construction to not affect the field quality. The stress on the mechanical structures are shown in Fig. 4.44. For sake of simplicity, the results are shown only after energization. The level of stress was found to be lower than the limits, except for very localized hot spots under the keys, where interference cause plasticization to occur, but without compromising the effectiveness of the structure.

4.3.4 Cost estimate

The EuroCirCol collaboration has made a careful assessment of the magnet costs [38, 66] and split them into three main contributions: the conductor cost, the assembly cost, and the cost of the magnet parts. The main contributor is the conductor cost, which is of about 670 k€/magnet, considering the FCC target conductor cost of 5 €/kAm at 4.2 K and 16 T. This cost is between three and four times lower than the present cost of the HL-LHC conductor, noting that the expected J_c-increase has a direct impact on the cost reduction [27, 58]. Recent results demonstrated that is possible to obtain a J_c-enhancement well above than the target cost [57]. These results will have a positive impact on the cost reduction. Due to the limited number of suppliers and limited demand on the market at this stage, this cost is considered the most uncertain.

The cost of the parts amount to 450 k€/magnet. It is based on present costs and is estimated to be solid as the production can be performed by standard manufacturing industry.

The assembly cost is set to 600 k€, which is about twice the cost of the LHC magnet assembly. This cost is dominated by the number of coils in the magnet and by their increased complexity. The manufacturing will require a tailor-made production line, and the final cost will depend on the industrialization degree that can be achieved during the series production.

Mainly due to the uncertainty of the cost of the conductor, and also to

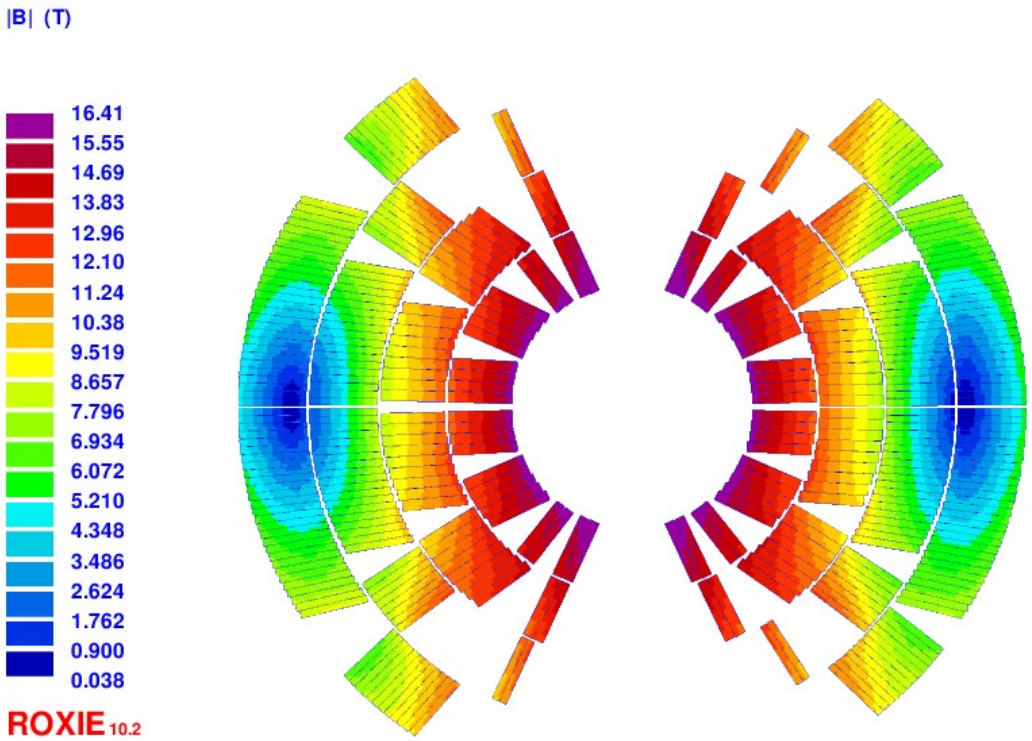

Figure 4.45: Asymmetric coil cross-section which is alternative to that shown in Fig. 4.30. The magnetic field is shown at the operating current.

the opportunities that an R&D program may provide to simplify the magnet manufacture, the EuroCirCol collaboration has believed more reasonable to give a range than a given number: between 1.7 and 2.0 M€/magnet.

4.4 Alternative coil design

A global scan of the parameter space by using the genetic algorithm of the ROXIE optimizer has required a computational time of the order of a few seconds to evaluate both the iron yoke saturation and the asymmetric coil cross-section, made of 12 blocks of Rutherford cables. Because the algorithm has taken tens of thousands of evaluations, the optimization has been time-consuming.

By applying the analytical approach described in chapter 3, we have looked for new configurations with a lower or equal number of sectors. By performing just one iteration, we have minimized the quadratic sum of the b_n^{coil} in Eq. (3.28) up to b_{10}^{coil}. In this way, we have generated a coil cross-section to estimate the shifts $\Delta b_n^{sat+geom}$ of Eq. (3.29) by means of a usual

Table 4.16: Lower-order normal harmonics at the operating current before and after a small fine-tuning by means of ROXIE.

b_2	b_3	b_4	b_5	b_6	b_7	b_8	b_9	b_{10}
0.82	−1.68	0.15	−0.66	−0.02	0.17	0.02	−0.36	0.02
0	0	0	0	0	0.49	0	−0.24	0.02

Table 4.17: Higher-order normal harmonics at the operating current before and after a small fine-tuning by means of ROXIE.

b_{11}	b_{12}	b_{13}	b_{14}	b_{15}	b_{16}	b_{17}	b_{18}	b_{19}	b_{20}
1.09	0	−0.26	0	−0.05	0	−0.05	0	0	0
1.13	0	−0.25	0	−0.05	0	−0.05	0	0	0

numerical code and by assuming the iron yoke in Fig. 4.26. We have considered non-negligible only the terms $\Delta b_2^{sat+geom}$ and $\Delta b_3^{sat+geom}$ (about 30 units and −20 units respectively). Then, by using the iterative method and by assuming 10-12 sectors we have minimized the quadratic sum of Eq. (3.29) up to b_{10} with the only non-zero terms $\Delta b_2^{sat+geom}$ and $\Delta b_3^{sat+geom}$. Our code has evaluated the asymmetric coil cross-section up to 12 sectors in a computational time of about 6 milliseconds, i.e., roughly 1000 times faster than the traditional numerical codes, as ROXIE or Opera. The computational time of every iteration has been at most of about 20 minutes. The code has stopped almost always after one iteration. This means that every 20 minutes we had the coordinates of a possible asymmetric coil cross-section, which already considered with excellent approximation the iron yoke saturation (see Tables 4.16 and 4.17). Owing to this speed, we were able to scan a much higher number of possible configurations. This fact, united with the ability of our code to better escape the local minima (see section 3.3), has allowed to find more than 30 possible solutions with the coil cross-section made of 10-12 sectors.

We have inserted the found configurations in ROXIE, for computing the peak fields and the operating margins with the coil cross-section made of blocks of Rutherford cables and the iron yoke shown in Fig. 4.26. The analysis has shown that all the configurations with less than 12 sectors bring to either too high peak fields or too big blocks.

Fig. 4.45 shows the alternative solution which best fits the specifications. Tables 4.16 and 4.17 show the harmonics of this configuration. The first

line displays the multipoles at the nominal current when the solution has been inserted in ROXIE. The second line shows the harmonics after a small fine-tuning on the positions and the tilts of the blocks by using the local optimizer of ROXIE. The current intensity in each block is 11.41 kA, the peak fields are 16.4 T in the high-field conductor and 12.5 T in the low-field conductor, the operating points on the load-line are about at 86% for the high-field conductor and roughly at 85% for the low-field conductor. This design has a field quality lightly better than the baseline configuration and has a margin lightly higher on the load-line of the low-field conductor. These results show that in principle this configuration could be a valid alternative to the current one.

Chapter 5

Recombination Dipoles for HL-LHC and FCC

5.1 Introduction

We have used the analytical method described in chapter 3 to study possible improvements to the present design [31] of the recombination dipoles D2 for HL-LHC. Moreover, by using the commercial software Opera [45] we have developed the 3D electromagnetic simulations of the short model under construction at ASG Superconductors in Genova [40, 46, 59]. We have generated a magnetic field map on the coil conductors and have found the position of the peak field in the coil end of the side opposite to the magnet connections.

We have helped to develop the preliminary electromagnetic design of the Double-Aperture Recombination Dipoles (DARD) for FCC [62]. The design is based on the study for the $\cos\theta$ bending dipole presented in chapter 4 and shares with that several features. The Nb_3Sn Rutherford cable allows to generate a 10-T field in a 60-mm bore, resulting in an integrated magnetic field of 122 T m, with the same polarity in both apertures. The inter-beam distance is 204 mm and the asymmetric coil has been optimized (by using only ROXIE [9]) to cope with the cross-talk between the two apertures.

5.2 Design of D2 for HL-LHC

5.2.1 Magnetic design

2D model

The recombination dipoles D2 must bend the particle beams in opposite directions. They are twin-aperture magnets with a separation between the

Table 5.1: Main requirements for the recombination dipoles D2.

Feature	Unit	Value
Integrated magnetic field	T m	35
Magnetic length	m	< 10
Aperture diameter	mm	105
Inter-beam distance	mm	188
Operating temperature	K	1.9
Margin on load-line	%	35
Multipole variation due to iron saturation	unit	< 10
Number of apertures		2

apertures of 188 mm and a bore diameter of 105 mm. The dipoles must generate an integrated magnetic field of 35 T m with the same polarity in both apertures. The separation distance between the coils allows a strong magnetic cross-talk. In the LHC recombination dipoles [8, 18] (see Fig. 1.11), this issue has been solved by interposing the iron yoke between the apertures. The magnetic field is low enough (2.77 T) for allowing the iron to magnetically shield the two coils from each other. This solution is not practicable in the new D2 design. Due to the length limitation (< 10 m), the HL-LHC dipole will have to generate a magnetic field higher than 3.5 T in each aperture. Because the field direction is identical in both apertures, the magnetic field between the coils sums up and saturates the iron yoke [22], resulting in a dramatic increase of unwanted multipoles, b_2, b_3, and b_4 mainly.

Studies performed at CERN [20], Fermilab [13], BNL [22] and LBNL [24] showed that solutions can be found with no iron close to the coils and a asymmetric coil geometry. Starting from these ideas, the INFN section of Genova have developed the new magnet design.

The baseline requirements given by CERN for the recombination dipoles D2 of HL-LHC are shown in Table 5.1. The INFN has moved toward a design with no iron between the apertures, because this choice reduces the saturation effects on the field quality. At the same time, just due to the lack of the iron, a magnetic cross-talk between the two coils takes place from very low currents.

The basic idea is that the magnetic cross-talk could be suitably compensated through a left-right asymmetric coil layout. In order to simplify the design, the choice has been made to proceed with 4–5 blocks in single-layer coils. This option practically limits the magnetic field to about 4.5 T. The Rutherford cable used for the winding is that of the outer layer of the LHC

Table 5.2: Main features of the D2 short model.

Feature	Unit	Value
Magnetic length	m	7.78
Bore magnetic field	T	4.5
Peak field	T	5.2
Operating current	kA	12.34
Stored energy	MJ	2.28
Overall current density	A/mm^2	443
Magnet physical length	m	8.11
Operating point on load-line	%	66.7

Table 5.3: Main features of the conductor.

Feature	Unit	Value
Material		NbTi
Cu/Non-Cu		1.95
No. of strands		36
Strand diameter	mm	0.825
Cable bare width	mm	15.1
Cable bare inner thickness	mm	1.362
Cable bare outer thickness	mm	1.598
Insulation azimuthal thickness	mm	0.1
Insulation radial thickness	mm	0.125

bending dipoles [11] (see features in Tab. 5.3). Some interesting configurations have been found with low or negligible unwanted multipoles. Nevertheless, the asymmetric coil design alone has been unable to completely solve the problem of the multipole variation due to iron saturation.

Taking advantages of the studies done in BNL [22] about the possibility to control the saturation effects through a suitable shaping of the iron yoke with an elliptical cross-section (307 mm semi-major axis, 275 mm semi-minor axis), the INFN has found that one particular configuration was fulfilling the magnetic requirements shown in Table 5.1. Figures 5.1 and 5.2 show the best configuration found following this approach. The first figure shows the elliptical cross-section of the iron yoke and the latter displays the asymmetric coil layout with 31 turns on a coil quarter. The coils are placed in an almost rectangular window of the iron yoke with round corners (398 mm wide and

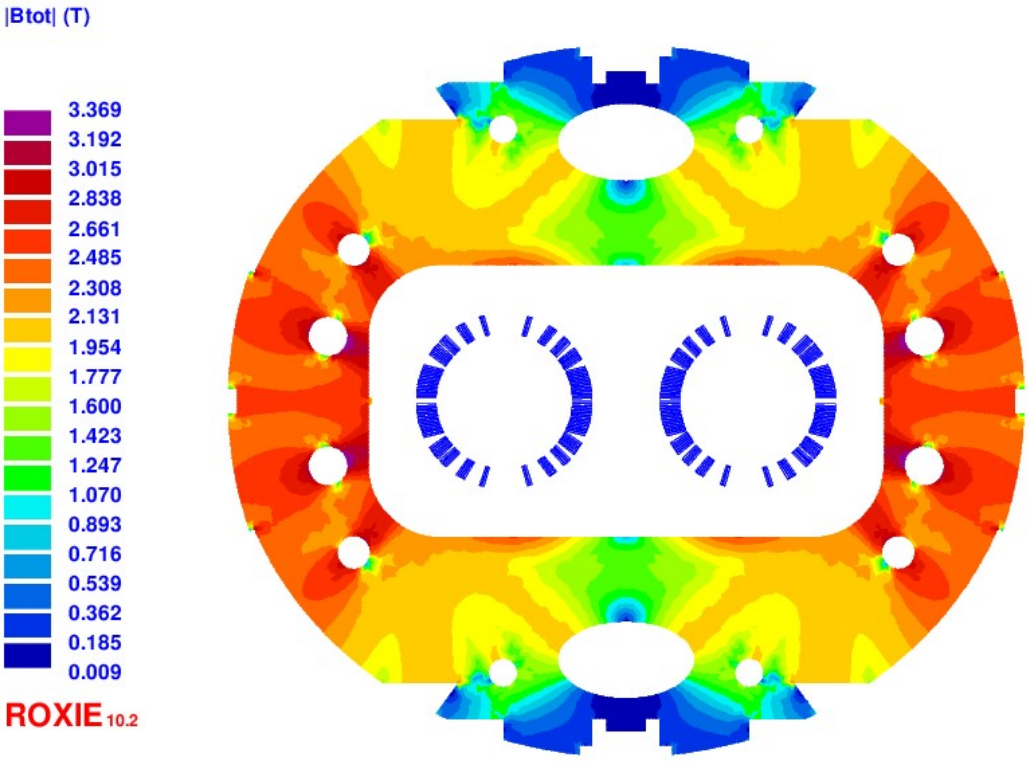

Figure 5.1: Iron yoke design of the recombination dipoles D2. The magnetic field is shown at the operating current.

211 mm high). The curvature radius of the corners is an important factor limiting the multipole variation as the magnetic field is increased, as well as the elliptical outer shape of the yoke. The main characteristics of the optimized layout are shown in Table 5.2 (target data shown in Table 5.1 are not duplicated if unchanged). The optimization has been performed with ROXIE, after preliminary systematic analyses done with ANSYS [71], which has been also used for mechanical analyses and for calculating the effects of mechanical deformation on multipoles. Tables 5.4 and 5.5 show the normal harmonics at the operating current and Fig. 5.3 displays the lower-order multipoles as a function of the magnetic field in the aperture. The four holes of the yoke closer to the horizontal axis have been design to control the b_3 and b_5 variation due to the iron saturation.

Fig. 5.4 shows the load-line of the D2 conductor. The operating point is at about 66.7% of the load-line, slightly higher than the initial project specification. Taking into account that the LHC bending dipoles work at about 86% of the load-line, CERN and INFN have evaluated that a slightly lower margin than the initial project requirement will not cause issues. The

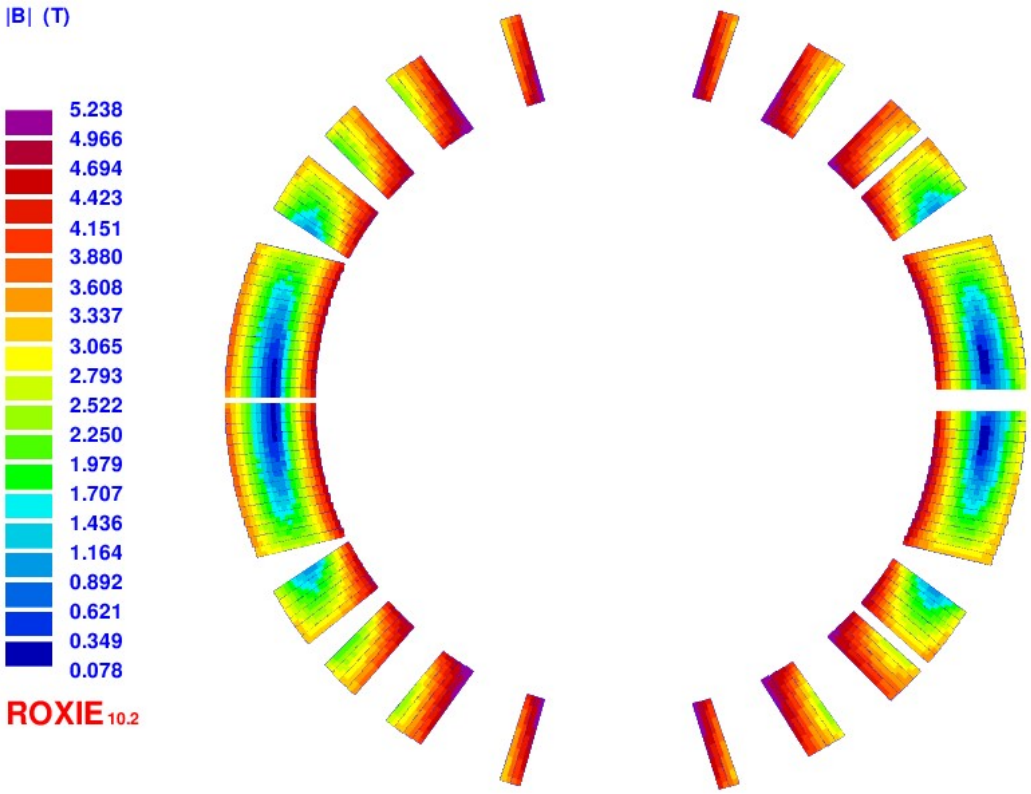

Figure 5.2: Asymmetric coil cross-section of the recombination dipoles D2. The magnetic field is shown at the operating current.

Table 5.4: Lower-order normal harmonics at the operating current.

b_2	b_3	b_4	b_5	b_6	b_7	b_8	b_9	b_{10}
0	0	0	0	0	0	0	0	0

Table 5.5: Higher-order normal harmonics at the operating current.

b_{11}	b_{12}	b_{13}	b_{14}	b_{15}	b_{16}	b_{17}	b_{18}	b_{19}	b_{20}
−1.89	−1.80	−1.91	−1	−0.76	0.12	−0.04	0.14	0.16	−0.07

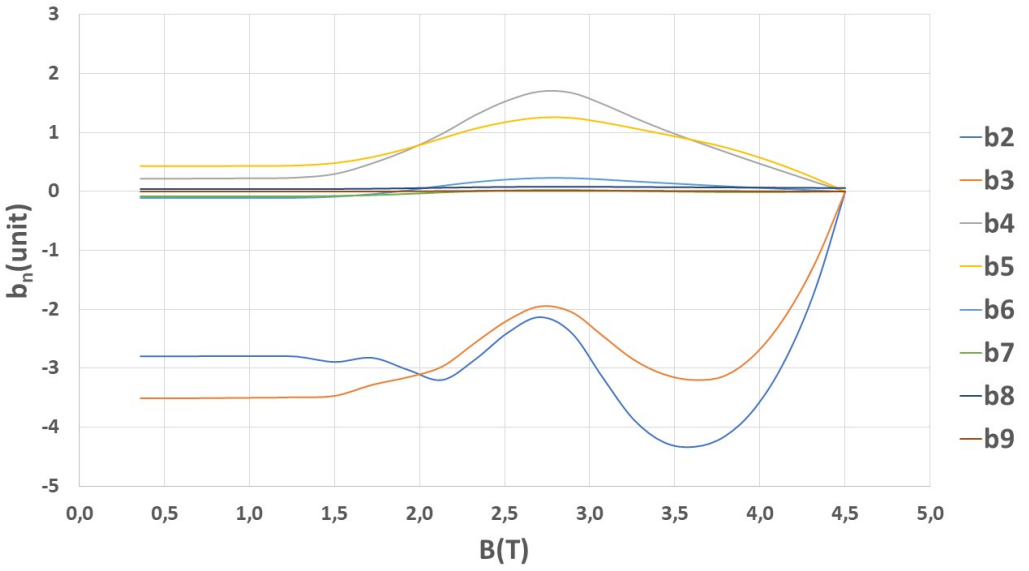

Figure 5.3: Normal harmonics as a function of the magnetic field in the aperture.

peak field (5.24 T) is localized on the fourth block in the coil side facing the other coil (the left side of the coil in Fig. 5.2).

3D model

The coil end design of the D2 magnet has required a compromise between the minimization of the peak field and the optimization of the integrated harmonics. On one hand, the heads must be as compact as possible to optimize the field quality. On the other hand, the turns must be located as far as possible from each other to lower the peak field on the conductors. The design of the short model is the best compromise between these two requirements. Figures 5.5 and 5.6 show the coil ends in ROXIE.

The peak field in the connection side (4.84 T) is lower than the peak value in the straight part (5.24 T). Instead, the peak field in the side opposite to the connections is slightly higher (5.26 T). The region of the peak field is the point where the margin on the load-line is lower, i.e., the point where a transition of the superconductor is more probable. Hence, it is important to know its location. The minimal difference between the values of the peak field in the straight part and the coil end has required confirmation by using other simulation software.

We have performed the 3D electromagnetic simulations by means of Opera, building the short model with the symmetric coil ends, i.e., two sides opposite to the magnet connections (see Fig. 5.7). The ROXIE and Opera

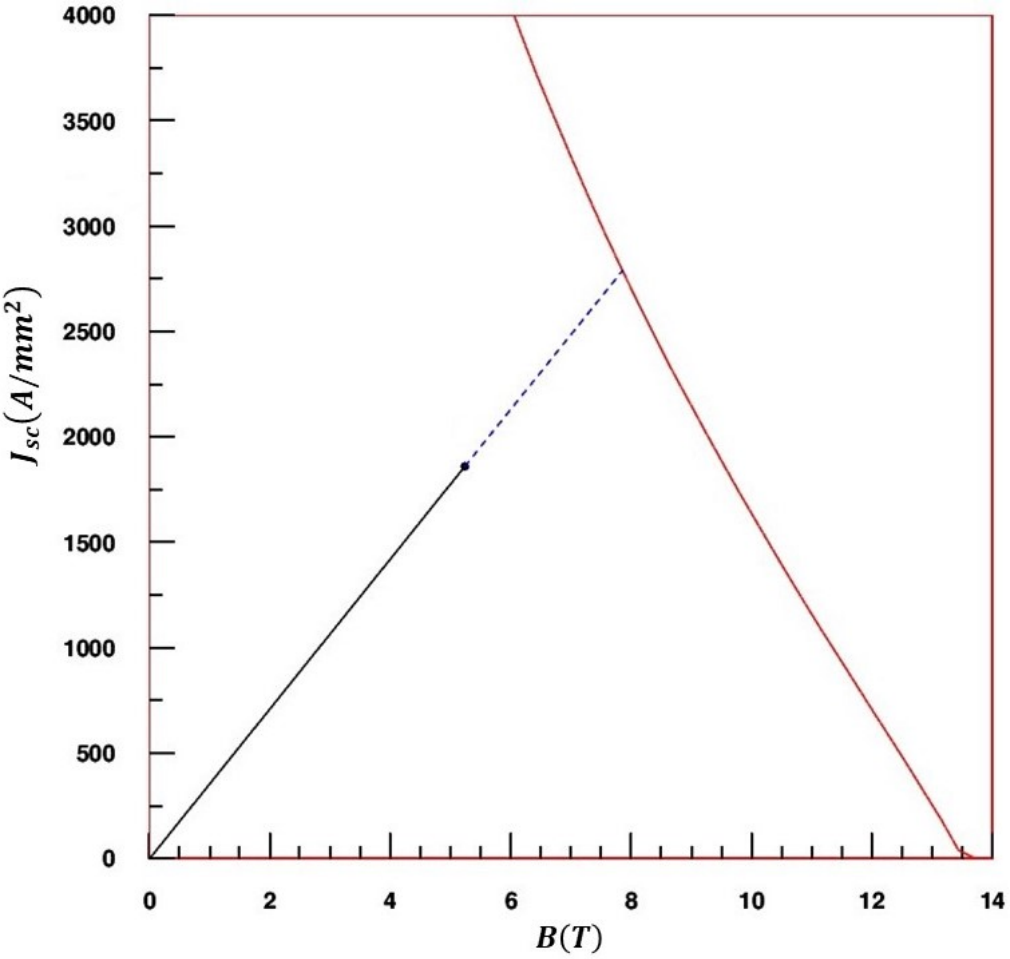

Figure 5.4: Load-line of the D2 conductor for HL-LHC. The red curve is the NbTi critical current density. The operating point is about at 66.7% of the load-line.

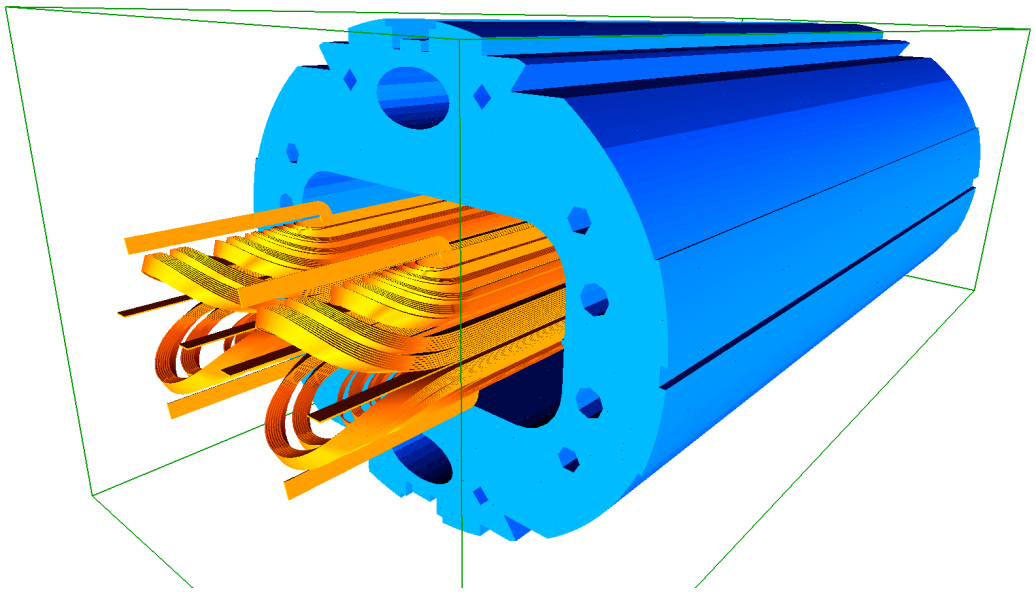

Figure 5.5: Side of the magnet connections in ROXIE. The coils are in yellow and the iron yoke in blue.

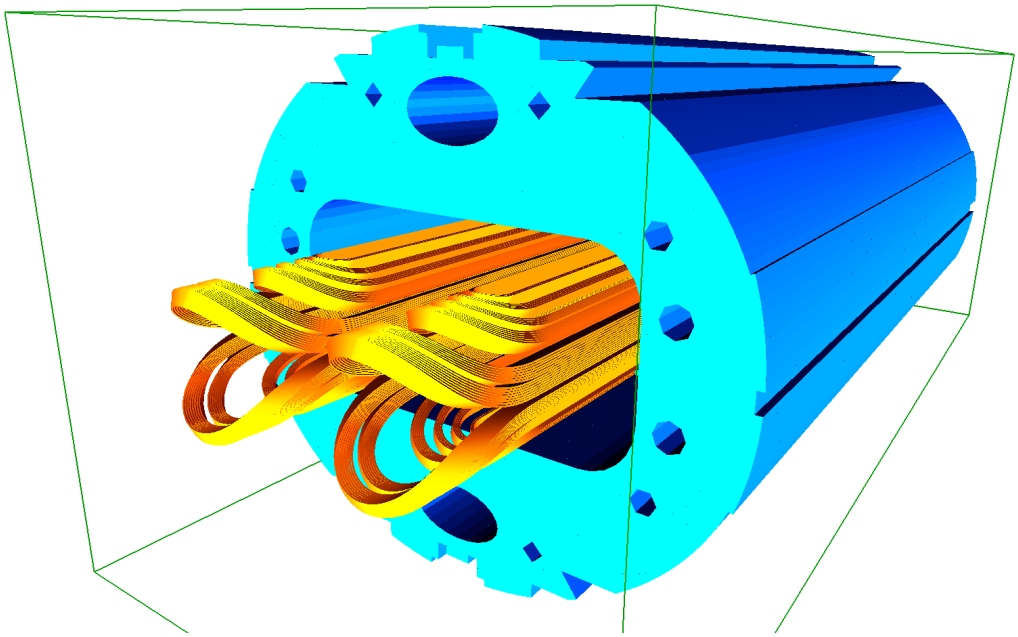

Figure 5.6: Side opposite to the magnet connections in ROXIE. The coils are in yellow and the iron yoke in blue.

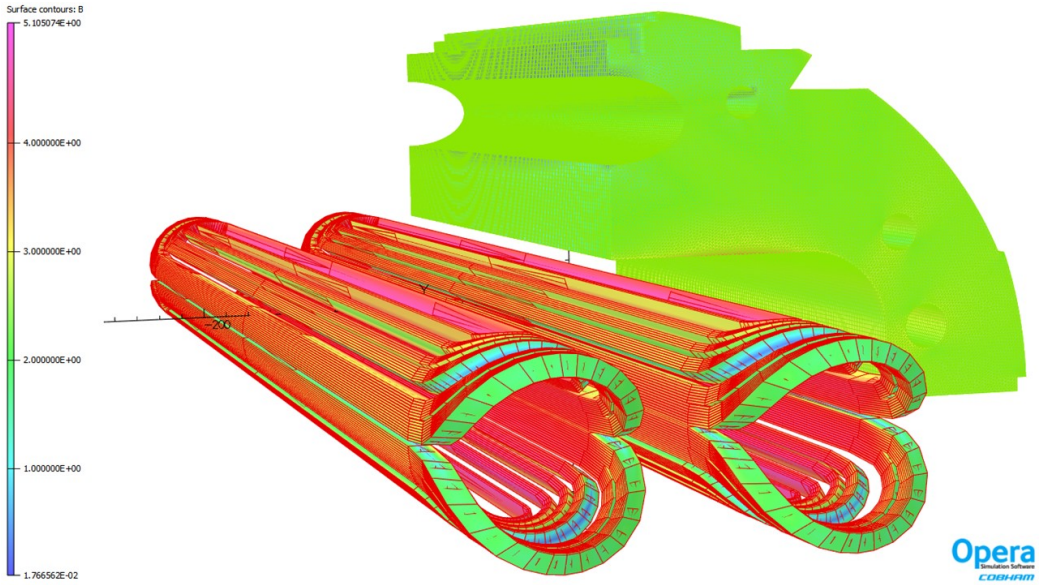

Figure 5.7: 3D electromagnetic model in Opera with the symmetric coil ends (two sides opposite to the magnet connections). The magnetic field is shown at the operating current.

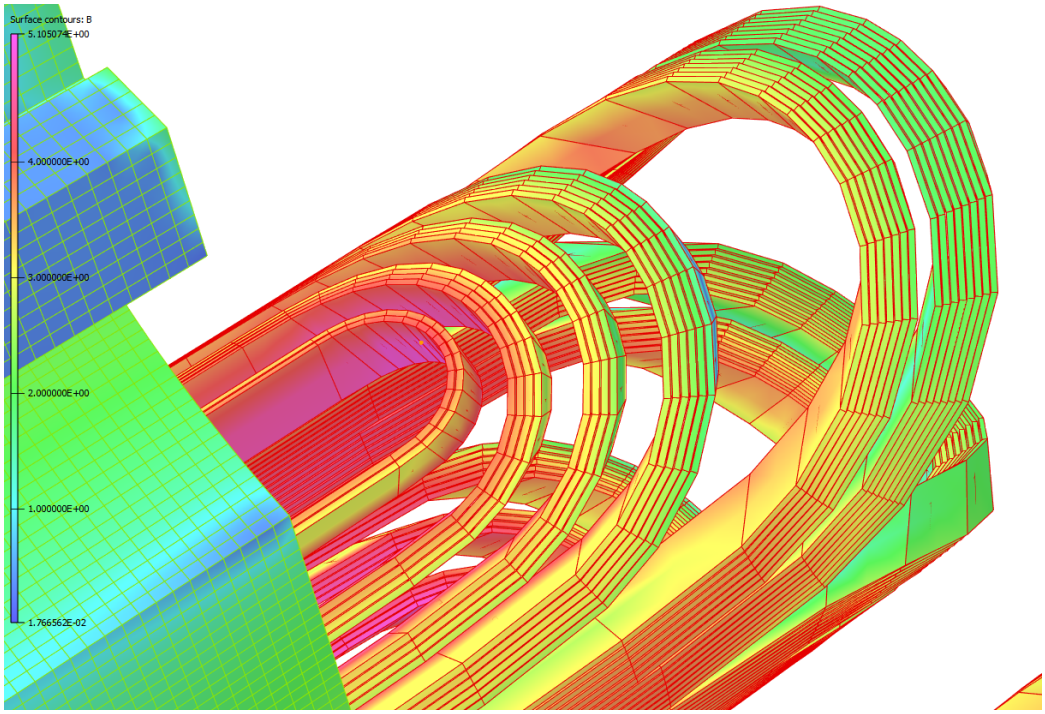

Figure 5.8: Map of the magnetic field on the conductors. The yellow point in the most internal conductor shows the position of the peak field.

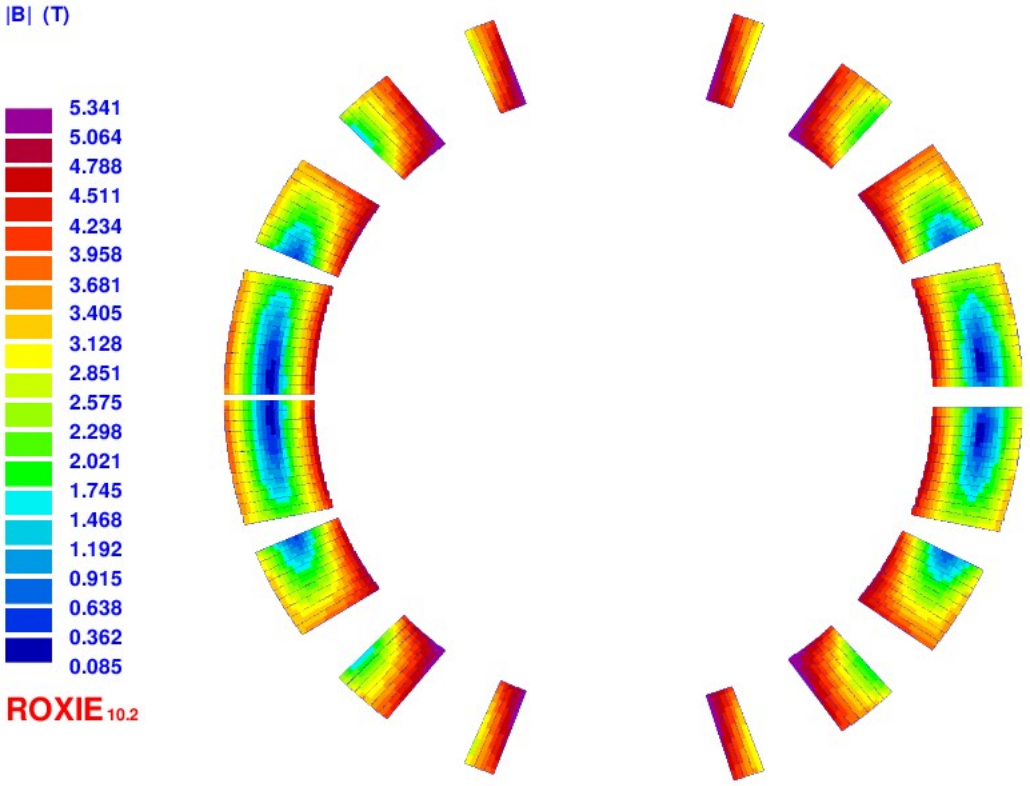

Figure 5.9: Asymmetric coil cross-section which is alternative to that shown in Fig. 5.2. The magnetic field is shown at the operating current.

simulations have shown a difference of about 0.1 T in the values of the magnetic field on the conductors. The electromagnetic model has confirmed that the peak field in the coil end is slightly higher than in the straight part. In particular, both ROXIE and Opera have confirmed that the peak field is located in the most internal conductor of the extremity (see Fig. 5.8).

5.2.2 Alternative coil design

The ROXIE optimizer has required a computational time of the order of the seconds to evaluate both the asymmetric coil cross-section, made of 4 or 5 blocks of Rutherford cables, and the iron yoke saturation. Because the genetic algorithm has taken thousands of evaluations, the optimization has been time-consuming.

We have reconsidered the D2 design on the basis of the analytical approach described in chapter 3 and have looked for new coil configurations with four or five sectors. By performing just one iteration, we have minimized

Table 5.6: Lower-order normal harmonics at the operating current before and after a small fine-tuning by means of ROXIE.

b_2	b_3	b_4	b_5	b_6	b_7	b_8	b_9	b_{10}	b_{11}
8.98	3.23	9.35	2.92	0.72	−1.81	0.08	−0.66	−0.12	−0.09
0	0	0	0	0	0	0.05	0	−0.25	0.03

Table 5.7: Higher-order normal harmonics at the operating current before and after a small fine-tuning by means of ROXIE.

b_{12}	b_{13}	b_{14}	b_{15}	b_{16}	b_{17}	b_{18}	b_{19}	b_{20}
−0.2	0.14	−0.29	0.41	−0.71	−1.12	0.12	−0.09	0.09
−0.37	−0.02	−0.38	0.43	−0.7	−1.09	0.11	−0.10	0.09

the quadratic sum of the b_n^{coil} in Eq. (3.28) up to b_9^{coil}. In this way, we have generated a coil cross-section to estimate the shifts $\Delta b_n^{sat+geom}$ of Eq. (3.29) by means of a usual numerical code and by assuming the iron yoke in Fig. 5.1. We have considered non-negligible only the terms $\Delta b_2^{sat+geom}$ and $\Delta b_3^{sat+geom}$ (about −200 units and −80 units respectively). Then, by using the iterative method we have minimized the quadratic sum of Eq. (3.29) up to b_9 for 4 sectors and up to b_{11} for 5 sectors, with the only non-zero terms $\Delta b_2^{sat+geom}$ and $\Delta b_3^{sat+geom}$. Our code has evaluated the asymmetric coil cross-section, made of 4 or 5 sectors, in a computational time of about 2 milliseconds, i.e., roughly 1000 times faster than the traditional numerical codes, as ROXIE or Opera. The computational time of every iteration has been at most of about 7-8 minutes. The code has stopped after about 2-3 iterations. This means that about every 15-20 minutes we had the coordinates of a possible asymmetric coil cross-section, which already considered with good approximation the iron yoke saturation (see Tables 5.6 and 5.7). Owing to this speed, we were able to scan a much higher number of possible configurations. This fact, united with the ability of our code to better escape the local minima (see section 3.3), has allowed to find more than 40 possible solutions with the coil cross-section made of 4 or 5 sectors.

We have inserted the found configurations in ROXIE, for computing the peak fields and the operating margins with the coil cross-section made of blocks of Rutherford cables and the iron yoke shown in Fig. 5.1.

Fig. 5.9 shows the solution which best fits the specifications. Tables 5.6 and 5.7 show the harmonics of this configuration. The first line displays

Table 5.8: Main design parameters for DARD.

Feature	Unit	Value
Material		Nb_3Sn
Bore magnetic field	T	10
Magnetic length	m	12.2
Aperture diameter	mm	60
Beam distance	mm	204
Operating temperature	K	1.9
Operating point on load-line	%	74
Cu/non-Cu		≥ 0.8
Maximum no. of strands		40
Field harmonics (geom/sat)	unit	≤ 10
Number of apertures		2

the multipoles at the nominal current when the solution has been inserted in ROXIE. The second line shows the harmonics after a small fine-tuning on the positions and the tilts of the blocks by using the local optimizer of ROXIE. The current intensity in each block is 12.72 kA, the peak field is 5.34 T and the operating point on the load-line is about at 68.3%. This coil design has a field quality lightly better than the current configuration, but it has a margin lightly lesser on the load-line. These results, united with the more simple layout, show that in principle this coil arrangement could be a valid alternative to the current one.

5.3 Design of DARD for FCC

5.3.1 Magnetic design

The design parameters given by the EuroCirCol collaboration for FCC DARD are shown in Table 5.8. Based on previous experiences, i.e., LHC D2 [12] and HL-LHC D2, we moved toward a winding layout with a left-right asymmetry, an elliptical iron yoke and a rectangular window for the iron yoke in which the coils are installed. The simultaneous optimization of all the geometrical parameters of these components is needed to suitably compensate the magnetic cross-talk in order to obtain a field quality that completely fulfills all the project requirements. In particular, the optimization proved that an elliptical iron yoke is mandatory to reach this goal.

Fig. 5.10 shows the cross-section of the cold mass and Fig. 5.11 displays

Table 5.9: Main features of the optimized design.

Feature	Unit	Value
Peak field	T	10.56
Operating current	kA	14.68
Iron yoke semi-major axis	mm	330
Iron yoke semi-minor axis	mm	265
Stored energy at nominal current	MJ/m	0.8
Inductance at nominal current	mH/m	7.5

Table 5.10: Main features of the conductors.

Feature	Unit	Value
Material		Nb_3Sn
Cu/Non-Cu		2.1
No. of strands		40
Strand diameter	mm	0.8
Bare width	mm	16.8
Bare inner thickness	mm	1.376
Bare outer thickness	mm	1.610
Insulation thickness	mm	0.15
Keystone angle	°	0.8
Operating point on load-line	%	74

in more detail the cable distribution in the winding. In Table 5.9 the main characteristics of the optimized magnetic design are listed. The peak field is localized on the fourth block of the first layer in the coil side facing the iron yoke (the right side of the coil in Fig. 5.11).

The magnetic $\cos\theta$ layout is based on two asymmetric apertures with an inter-beam distance of 204 mm and a bore diameter of 60 mm. To have a magnetic field of 10 T in the bore, two layer of conductor are required. The main features of the conductor used for this preliminary design are listed in Table 5.10. Fig. 5.12 shows the load-line of the conductor. The operating point is about at 74% leaving a wide margin on the load-line, as required in the specifications.

The magnetic optimization has been performed by using ROXIE. The lower-order and higher-order normal harmonics at the operating current are listed in Tables 5.11 and 5.12 respectively. While the field multipoles as a

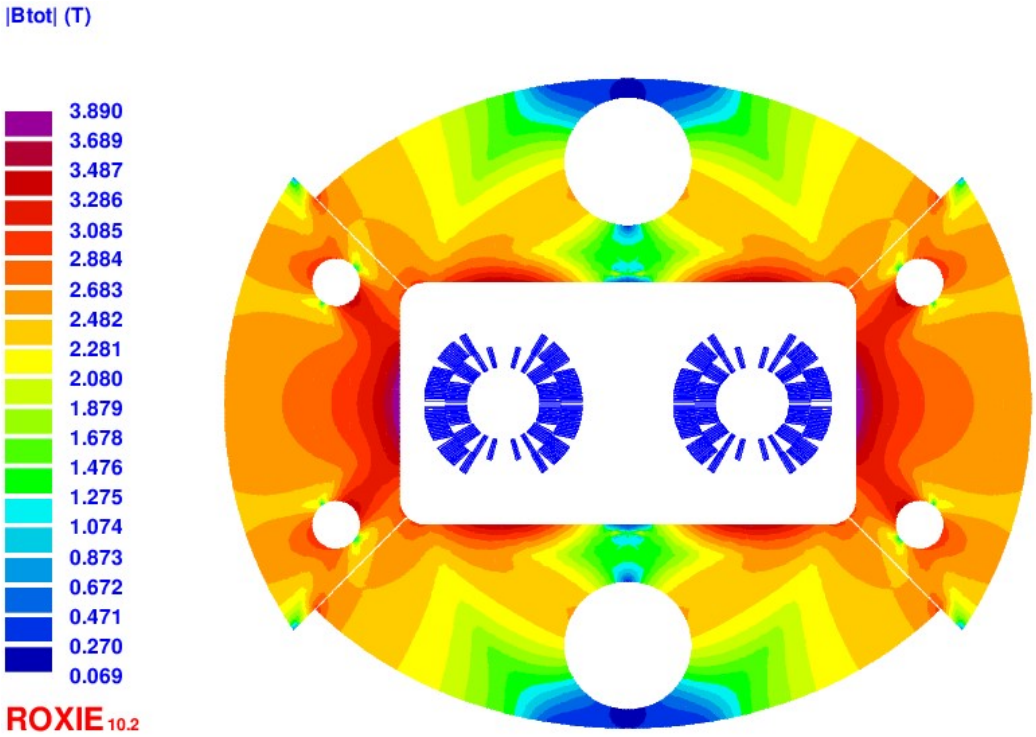

Figure 5.10: Design of the iron yoke for DARD. The magnetic field is shown at the operating current.

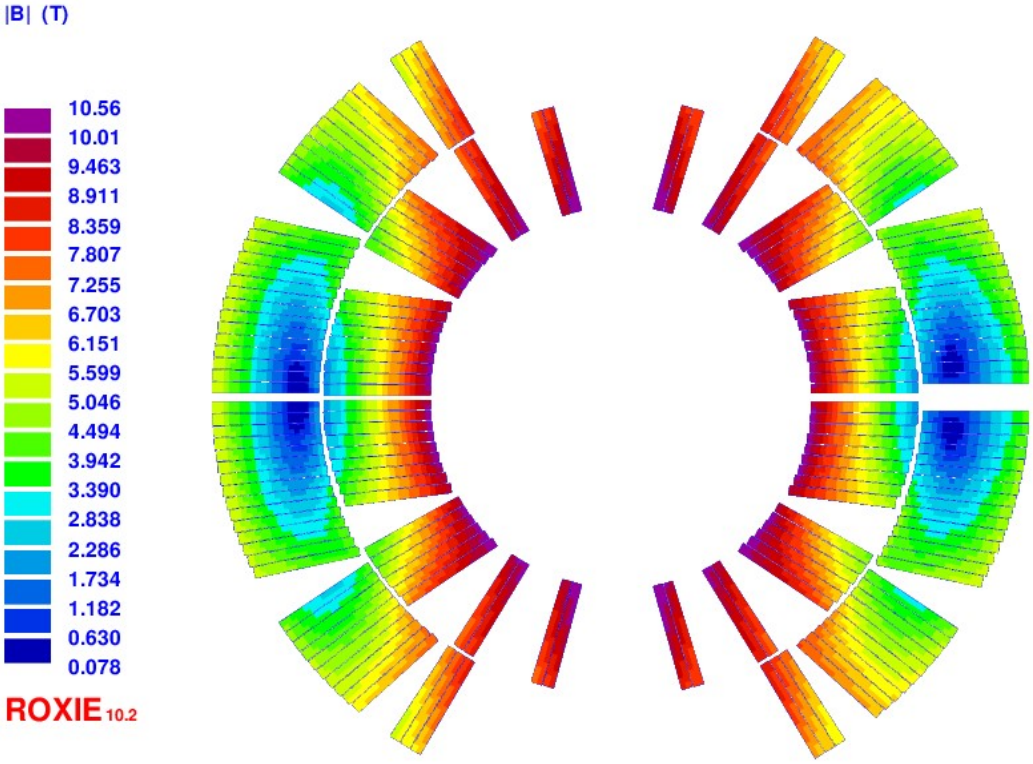

Figure 5.11: Asymmetric coil cross-section for DARD. The magnetic field is shown at the operating current.

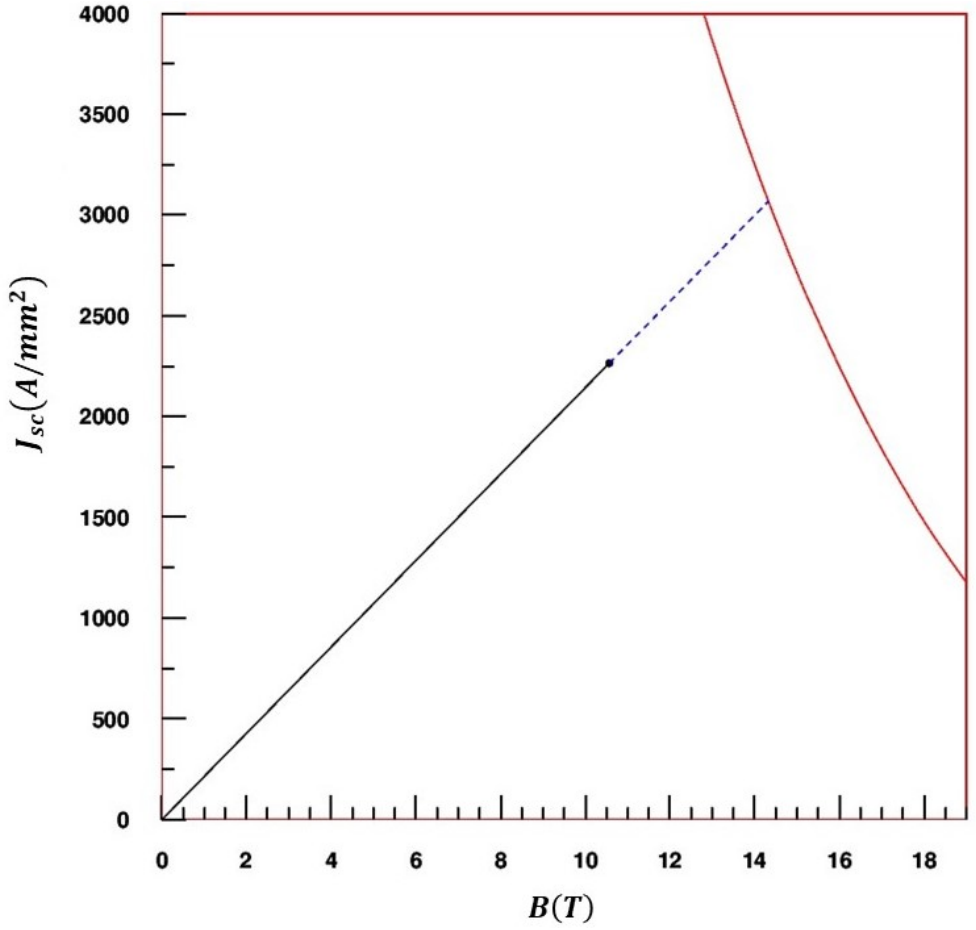

Figure 5.12: Load-line of the DARD conductor for FCC. The red curve is the Nb_3Sn critical current density. The operating point is about at 74% of the load-line.

function of the current intensity are shown in Fig. 5.13. All harmonics stay well within the limits and the field quality of this optimized magnetic design completely fulfills all the requirements imposed by the project.

5.3.2 Mechanical design

The pre-stress is provided by the bladder and key technique. The iron yoke is divided into four pieces to ensure the correct insertion of the bladders. In this way, during assembly, part of the pre-stress is given by the interference of the keys. Then, in the cool down, the aluminum shell shrinks more than the inner components, so that additional pre-stress is given to the coil at cryogenic temperature when Nb_3Sn is less brittle.

This preliminary design aims to guarantee the contact pressure between the pole turn and the titanium nose after energization at 10 T and ensure that each component of the structure stays within its stress limit during assembly, cool down and energization to prevent any degradation of the magnet performances.

In Table 4.8 the material properties and stress limit for each component of the model at room temperature (293 K) are reported, while in Table 4.9 the same parameters are given at cryogenic temperature (1.9 K).

The mechanical analysis has been performed using ANSYS code [71]. The optimized cross-section is shown in Fig. 5.14. The finite element method has been iteratively used to optimize position, length, and interference of the keys and thickness of the aluminum shell. To guarantee an optimal match between the elliptic iron yoke and the external aluminum shell a stainless steel filler has been added.

The preliminary design of the recombination dipole for FCC widely fulfills all the project requirements regarding the contact pressure and the Von Mises stress distribution with no particular criticality. In Fig. 5.15 the contact pressure between pole and nose and the Von Mises stress distribution inside the winding after assembly, cool down, energization at the operating current and energization at 110% of the operating current are shown.

The peak stresses are well below the limits in all conditions. It is worth noting that the mechanical structure is optimized to ensure that the contact pressure of the winding at the pole level is positive everywhere in operating conditions. At 110% of the operating current, it is required that the peak stress remains within safe limit, but there is no additional requirement on the contact pressure. Finally, the Von Mises stress distribution in the overall cold mass after energization is shown in Fig. 5.16.

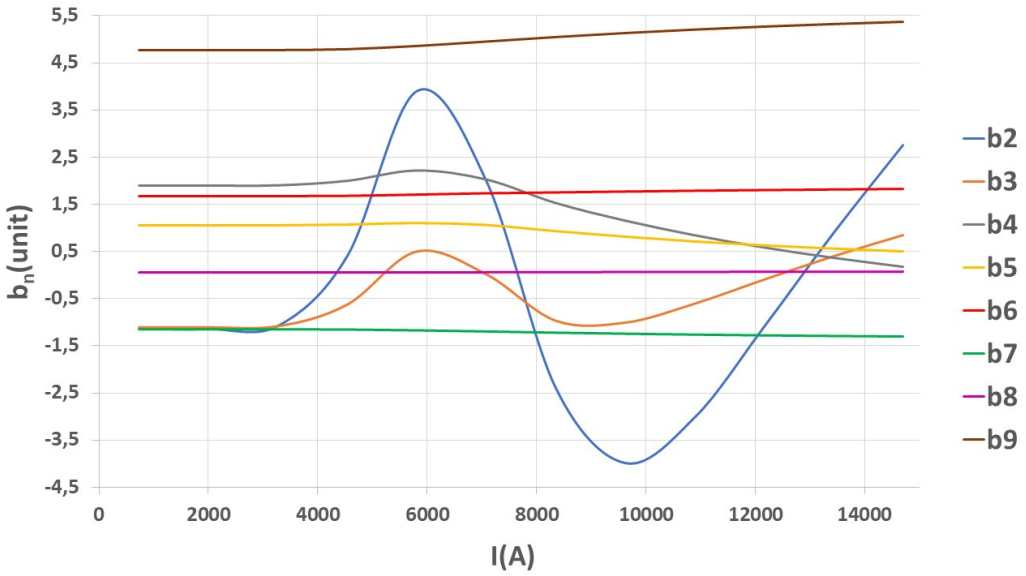

Figure 5.13: Field harmonics as a function of the current intensity.

Table 5.11: Lower-order normal harmonics at the operating current.

b_2	b_3	b_4	b_5	b_6	b_7	b_8	b_9	b_{10}
2.73	0.84	0.18	0.51	1.83	−1.31	0.08	5.37	−0.66

Table 5.12: Higher-order normal harmonics at the operating current.

b_{11}	b_{12}	b_{13}	b_{14}	b_{15}	b_{16}	b_{17}	b_{18}	b_{19}	b_{20}
−1.59	−0.27	−0.68	−0.06	−0.08	0.06	0.03	0.01	0.05	−0.02

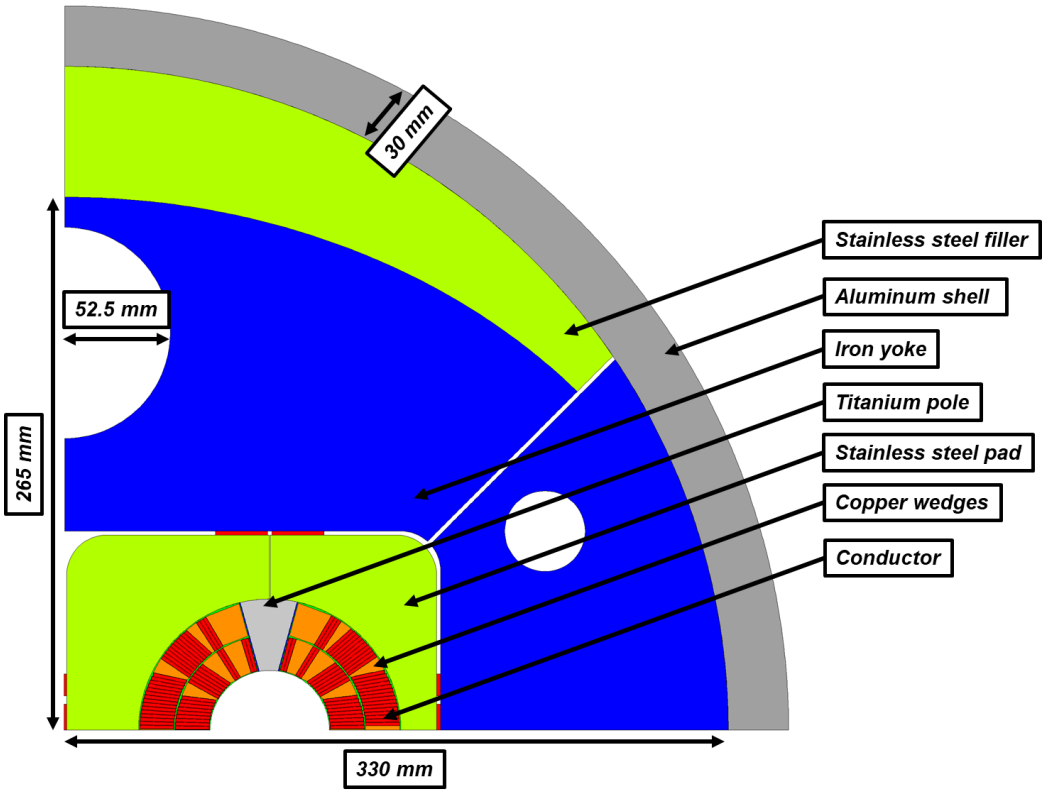

Figure 5.14: Main dimensions of the cold mass.

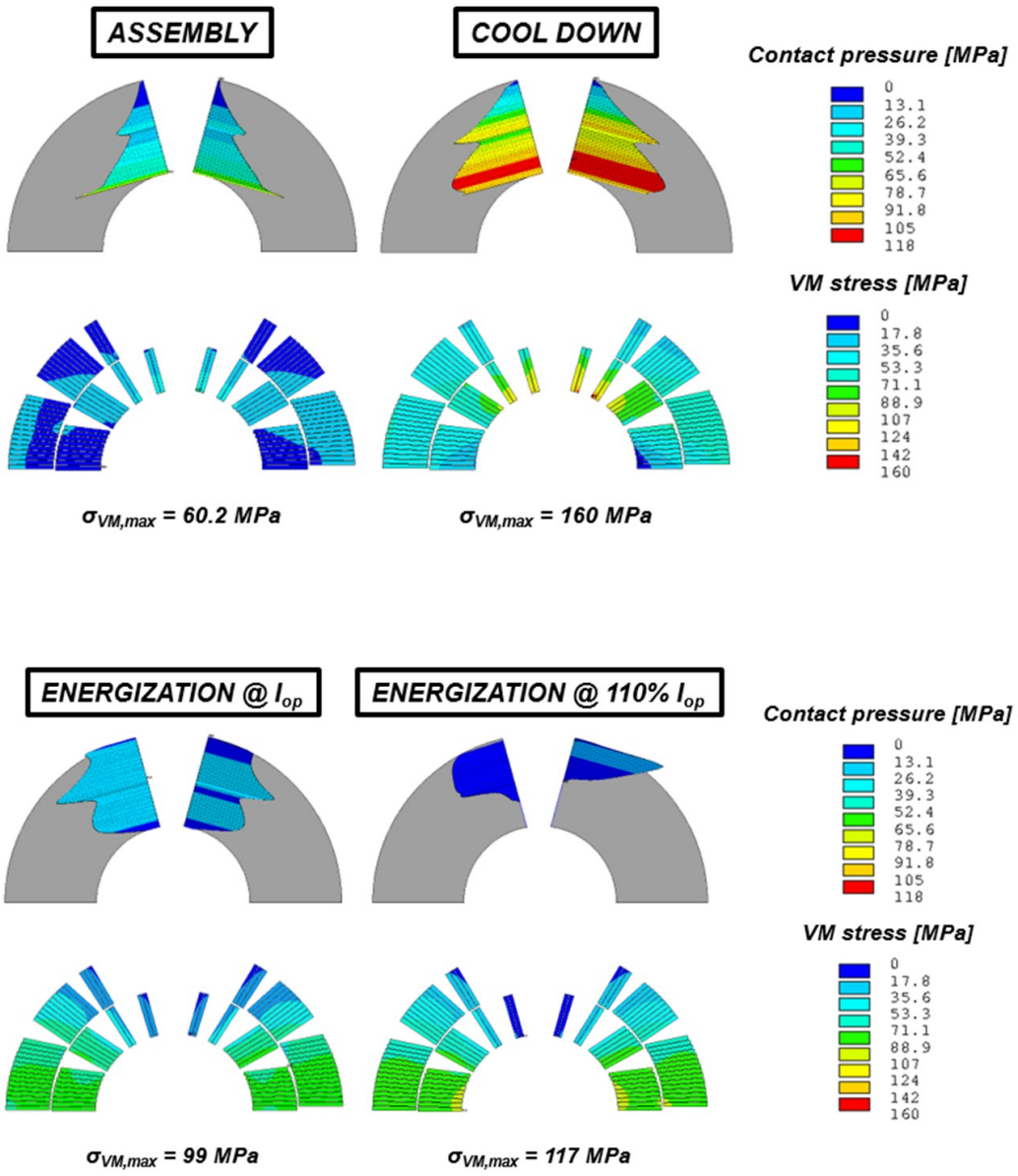

Figure 5.15: Contact pressure and Von Mises stress distribution [MPa]: after assembly at room temperature, after cool down, after energization at the operating current and after energization at 110% of the operating current.

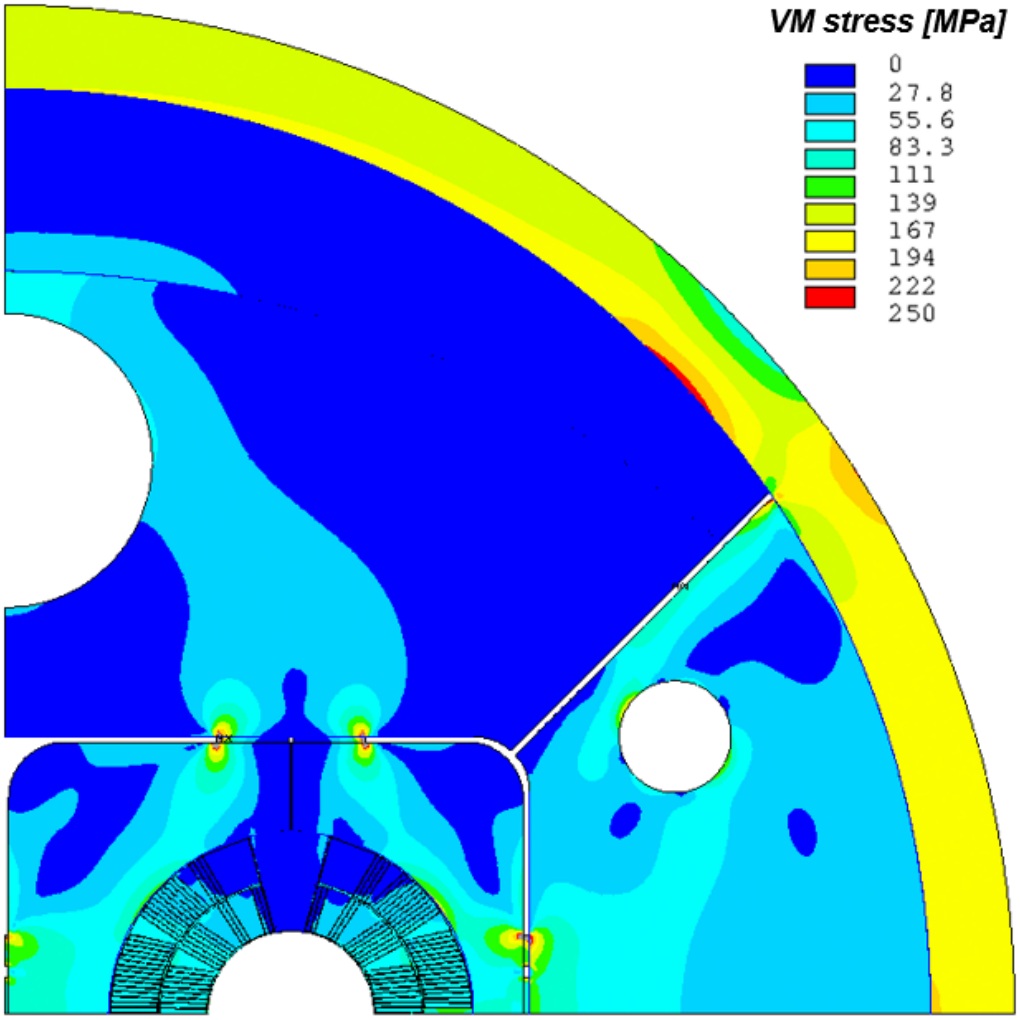

Figure 5.16: Von Mises stress distribution [MPa] in the cross-section of the magnet after energization at 10 T.

Conclusions

The first step in the coil design is to find the block arrangements, which generate a high-homogeneous magnetic field, given the bending radius, the cable width, the layer number and the inter-beam distance. These configurations cannot be derived explicitly and many numerical algorithms exist to find the optimal cross-sections [18]. Owing to the complicated magnet geometry (coils made of blocks, blocks made of cables and cables made of strands), they are time-consuming and, to be really effective, they have to operate on configurations that are not too far from a local optimum.

In the single-aperture layout, the sector model, approximating the blocks as annular sectors, is a powerful analytical tool, which allows to carry out an initial scan on a very large number of possible configurations [16, 25, 60]. This makes easier to find the cross-section which best suits the specifications.

The twin-aperture layout introduces a complicating factor: the contribution to the harmonic components which one coil exerts on the other aperture. This effect is referred to as magnetic cross-talk. If it is not negligible, an extension of the single-aperture sector model is required to analytically scan the parameter space. This is the case of the recombination dipoles D2 for the High Luminosity upgrade of LHC and the 16-T bending dipole for the Future Circular Collider.

We have developed an extension of the sector model [64], which we have used to find the asymmetric coil configurations, that minimize the magnetic cross-talk. Both for D2 and the FCC dipole, this method has allowed to faster optimize the magnetic designs and to find better configurations (lower higher-order harmonics) than those found with the standard techniques [18]. Our methodology has helped to finalize a design, which has been presented as the baseline in the Conceptual Design Report of FCC [55, 56]. Moreover, this method has allowed to find a new coil design for the recombination dipoles D2 of HL-LHC. The new layout is more simple and generates a magnetic field more homogeneous than the configuration currently under construction at ASG Superconductors in Genova.

We have developed the 3D electromagnetic simulations of both magnet

classes. In particular, we have been responsible for the 3D electromagnetic modeling of the FCC bending dipole, which we have realized by two different tools. The first is the commercial software Opera [45] based on the Finite Element Method (FEM). The second is a specific CERN program, ROXIE [9], based on the coupling between the Boundary Element Method and the Finite Element Method (BEM-FEM) [18].

A magnet for accelerator has two ends: the side of the connections between the blocks and the layers of the coil, and the side opposite to the connections. Each head generates unwanted multipoles, which alter the field homogeneity. Due to the magnet complexity and for easing the computation by ROXIE and Opera, we have created an independent model for each extremity with a magnetic length arbitrarily shorter than the design one. These models have allowed to quickly evaluate the effects of each head on the field harmonics. Projecting the results on the nominal magnetic length by appropriate analytical formulas, we could minimize the 3D multipoles and obtain a high-homogeneity magnetic field.

Due to the coil return, the peak field on the conductors in the ends is usually higher than in the straight part (typically several %) [18]. A transition of the superconductor due to possible disturbances is more probable in the region where the peak field is localized. The electromagnetic analysis has pointed out that, in the inner layers of the FCC coil, the magnetic field on the conductors quickly drops after the end of the iron yoke. This phenomenon has simplified the design process, precisely where the magnetic field is higher and more difficulties may arise.

Finally, we have helped to develop a preliminary design of the FCC recombination dipoles (called DARD), which have required a completely different approach with respect to the D2 magnets for LHC. The design is based on the study for the 16-T bending dipole and shares with that several features.

Bibliography

[1] R. A. Beth, "Complex Representation and Computation of Two-Dimensional Magnetic Fields", *Journal of Applied Physics*, vol. 37, no. 7, pp. 2568–2571, 1966. DOI: 10.1063/1.1782086. eprint: https://doi.org/10.1063/1.1782086.

[2] ——, "An Integral Formula for Two-Dimensional Fields", *Journal of Applied Physics*, vol. 38, no. 12, pp. 4689–4692, 1967. DOI: 10.1063/1.1709204. eprint: https://doi.org/10.1063/1.1709204.

[3] Foner Simon and Schwartz Brian, *Superconductor Materials Science: Metallurgy, Fabrication, and Applications*. Springer, 1981, ISBN: 978-1-4757-0039-8. DOI: 10.1007/978-1-4757-0037-4.

[4] R. Storn and K. Price, "Differential evolution–a simple and efficient adaptive scheme for global optimization over continuous spaces: technical report TR-95-012", *International Computer Science, Berkeley, California*, 1995.

[5] K.-H. Mess, S. Wolff, and P. Schmüser, *Superconducting Accelerator Magnets*. Word Scientific, 1996. DOI: 10.1142/3219. eprint: https://www.worldscientific.com/doi/pdf/10.1142/3219.

[6] R. Storn and K. Price, "Minimizing the real functions of the ICEC'96 contest by differential evolution", in *Proceedings of IEEE International Conference on Evolutionary Computation*, IEEE, 1996, pp. 842–844.

[7] A. Devred, "1999 Review of superconducting dipole and quadrupole magnets for particle accelerators", DAPNIA-STCM-99-24, 1999.

[8] A. Jain, P. Wanderer, and E. Willen, "Field quality in the twin aperture D2 dipoles for LHC under asymmetric excitation", in *Proceedings of the 1999 Particle Accelerator Conference (Cat. No.99CH36366)*, vol. 5, Mar. 1999, 3173–3175 vol.5. DOI: 10.1109/PAC.1999.792240.

[9] S. Russenschuck, "ROXIE: A Computer code for the integrated design of accelerator magnets", in *Particle accelerator. Proceedings, 6th European conference, EPAC'98, Stockholm, Sweden, June 22-26, 1998. Vol. 1-3*, 1999, pp. 2017–2019.

[10] S. Caspi *et al.*, "The use of pressurized bladders for stress control of superconducting magnets", *IEEE Transactions on Applied Superconductivity*, vol. 11, no. 1, pp. 2272–2275, Mar. 2001, ISSN: 2378-7074. DOI: 10.1109/77.920313.

[11] J. D. Adam *et al.*, "Status of the LHC superconducting cable mass production", *IEEE Transactions on Applied Superconductivity*, vol. 12, no. 1, pp. 1056–1062, Mar. 2002, ISSN: 2378-7074. DOI: 10.1109/TASC.2002.1018583.

[12] O. S. Brüning *et al.*, *LHC Design Report*, ser. CERN Yellow Reports: Monographs. Geneva: CERN, 2004. DOI: 10.5170/CERN-2004-003-V-1.

[13] V. V. Kashikhin and A. V. Zlobin, "Design study of 2-in-1 large-aperture ir dipole (D2) for the LHC luminosity upgrade", in *2007 IEEE Particle Accelerator Conference (PAC)*, Jun. 2007, pp. 464–466. DOI: 10.1109/PAC.2007.4440246.

[14] M. Conte and W. W. MacKay, *An Introduction to the Physics of Particle Accelerators*, 2nd. World Scientific, 2008. DOI: 10.1142/6683. eprint: https://www.worldscientific.com/doi/pdf/10.1142/6683.

[15] H. Padamsee, *RF Superconductivity*. John Wiley & Sons, Ltd, 2009, ISBN: 9783527627172. DOI: 10.1002/9783527627172.fmatter.

[16] F. Borgnolutti, E. Todesco, and A. Mailfert, "A Method for Coil Design of Superconducting Quadrupoles Based on Sector Coils and Fourier Series", *IEEE Transactions on Applied Superconductivity*, vol. 20, no. 3, pp. 1790–1793, Jun. 2010. DOI: 10.1109/TASC.2010.2043239.

[17] H. Felice *et al.*, "Test results of TQS03: A LARP shell-based Nb_3Sn quadrupole using 108/127 conductor", *Journal of Physics: Conference Series*, vol. 234, no. 3, p. 032 010, Jun. 2010. DOI: 10.1088/1742-6596/234/3/032010.

[18] S. Russenschuck, *Field computation for accelerator magnets: Analytical and numerical methods for electromagnetic design and optimization*. Weinheim: Wiley-VCH, 2010, ISBN: 9783527407699. DOI: 10.1002/9783527635467.

[19] S. Das and P. Suganthan, "Differential evolution: A survey of the state-of-the-art.", *IEEE Trans. Evolutionary Computation*, vol. 15, pp. 4–31, Jan. 2011.

[20] E. Todesco. (2013). "D2 field error tentative table", [Online]. Available: https://lhc-div-mms.web.cern.ch/lhc-div-mms/tests/MAG/docum/hilumi/Presentations/2013-10-22_et_D2_fq_1013.pptx.

[21] (Feb. 2014). "Future Circular Collider Study Kickoff Meeting", [Online]. Available: https://indico.cern.ch/e/fcc-kickoff.

[22] R. Gupta, "Conceptual Magnetic Design of the Large Aperture D2 Dipole for LHC Upgrade", in *Proc. 5th International Particle Accelerator Conference (IPAC'14), Dresden, Germany, June 15-20, 2014*, (Dresden, Germany), ser. International Particle Accelerator Conference, Geneva, Switzerland: JACoW, Jul. 2014, pp. 2737–2739. DOI: https://doi.org/10.18429/JACoW-IPAC2014-WEPRI102.

[23] B. Holzer, "Introduction to Transverse Beam Dynamics", Comments: contribution to the CAS - CERN Accelerator School: Course on Superconductivity for Accelerators, Erice, Italy, 24 Apr - 4 May 2013, edited by R. Bailey, CERN-2014-005, Apr. 2014, 27–45. 19 p. DOI: 10.5170/CERN-2013-007.27.

[24] G. Sabbi and X. Wang, *Design Study of the High Luminosity LHC Recombination Dipole (D2)*, ser. Technical Report. U.S. Department of Energy, May 2014. DOI: 10.2172/1164211.

[25] E. Todesco, "Magnetic Design of Superconducting Magnets", contribution to the CAS-CERN Accelerator School: Superconductivity for Accelerators, Erice, Italy, 24 April - 4 May 2013, edited by R. Bailey, 2014, 24 p. DOI: 10.5170/CERN-2014-005.269.

[26] ——, "Quench limits in the next generation of magnets", 10–16. 7 p, Jan. 2014, Comments: 7 pages, Contribution to WAMSDO 2013: Workshop on Accelerator Magnet, Superconductor, Design and Optimization; 15 - 16 Jan 2013, CERN, Geneva, Switzerland. DOI: 10.5170/CERN-2013-006.10.

[27] A. Ballarino and L. Bottura, "Targets for R&D on Nb_3Sn Conductor for High Energy Physics", *IEEE Transactions on Applied Superconductivity*, vol. 25, no. 3, pp. 1–6, Jun. 2015, ISSN: 2378-7074. DOI: 10.1109/TASC.2015.2390149.

[28] (Jun. 2015). "EuroCirCol Kickoff Meeting", [Online]. Available: https://indico.cern.ch/event/389991/overview.

[29] A. Zlobin *et al.*, "Design Concept and Parameters of a 15 T Nb_3Sn Dipole Demonstrator for a 100 TeV Hadron Collider", in *Proc. 6th International Particle Accelerator Conference (IPAC'15), Richmond, VA, USA, May 3-8, 2015*, (Richmond, VA, USA), ser. International Particle Accelerator Conference, Geneva, Switzerland: JACoW, Jun. 2015, pp. 3365–3367, ISBN: 978-3-95450-168-7. DOI: https://doi.org/10.18429/JACoW-IPAC2015-WEPTY041.

[30] L. Bottura *et al.*, "Superconducting Magnets for Particle Accelerators", *IEEE Transactions on Nuclear Science*, vol. 63, no. 2, pp. 751–776, Apr. 2016, ISSN: 1558-1578. DOI: 10.1109/TNS.2015.2485159.

[31] S. Farinon *et al.*, "The Design of Superconducting Separation Dipoles D2 for the High Luminosity Upgrade of LHC", *IEEE Transactions on Applied Superconductivity*, vol. 26, no. 4, pp. 1–4, Jun. 2016. DOI: 10.1109/TASC.2016.2523060.

[32] P. Ferracin *et al.*, "Development of MQXF: The Nb_3Sn Low-β Quadrupole for the HiLumi LHC", *IEEE Transactions on Applied Superconductivity*, vol. 26, no. 4, pp. 1–7, Jun. 2016, ISSN: 2378-7074. DOI: 10.1109/TASC.2015.2510508.

[33] I. Novitski *et al.*, "Development of a 15 T Nb_3Sn Accelerator Dipole Demonstrator at Fermilab", *IEEE Transactions on Applied Superconductivity*, vol. 26, no. 4, pp. 1–1, Jun. 2016, ISSN: 2378-7074. DOI: 10.1109/TASC.2016.2517024.

[34] A. G. *et al.*, *High-Luminosity Large Hadron Collider (HL-LHC): Technical Design Report V. 0.1*, ser. CERN Yellow Reports: Monographs. Geneva: CERN, 2017. DOI: 10.23731/CYRM-2017-004.

[35] C. Lorin, D. Durante, and M. Segreti, "EuroCirCol 16 T Block-Coils Dipole Option for the Future Circular Collider", *IEEE Transactions on Applied Superconductivity*, vol. 27, no. 4, pp. 1–5, Jun. 2017. DOI: 10.1109/TASC.2016.2639546.

[36] V. Marinozzi *et al.*, "Quench Protection Study of the Eurocircol 16 T $\cos\theta$ Dipole for the Future Circular Collider (FCC)", *IEEE Transactions on Applied Superconductivity*, vol. 27, no. 4, pp. 1–5, Jun. 2017, ISSN: 2378-7074. DOI: 10.1109/TASC.2017.2656156.

[37] T. Salmi *et al.*, "Quench protection analysis integrated in the design of dipoles for the Future Circular Collider", *Physical Review Accelerators and Beams*, vol. 20, Mar. 2017. DOI: 10.1103/PhysRevAccelBeams.20.032401.

[38] D. Schoerling *et al.*, "Considerations on a Cost Model for High-Field Dipole Arc Magnets for FCC", *IEEE Transactions on Applied Superconductivity*, vol. 27, no. 4, pp. 1–5, Jun. 2017, ISSN: 2378-7074. DOI: 10.1109/TASC.2017.2657510.

[39] M. Sorbi *et al.*, "The EuroCirCol 16 T Cosine–Theta Dipole Option for the FCC", *IEEE Transactions on Applied Superconductivity*, vol. 27, no. 4, pp. 1–5, Jun. 2017. DOI: 10.1109/TASC.2016.2642982.

[40] *Technical Design Report of the D2 Superconducting Prototype Dipole (MBRDP1) for the Luminosity Upgrade of LHC at CERN*, ser. Technical Report. INFN-LNF, Nov. 2017. eprint: https://www.ge.infn.it/~farinon/D2/TDR-D2.pdf.

[41] D. Tommasini *et al.*, "The 16 T Dipole Development Program for FCC", *IEEE Transactions on Applied Superconductivity*, vol. 27, no. 4, pp. 1–5, Jun. 2017. DOI: 10.1109/TASC.2016.2634600.

[42] F. Toral *et al.*, "EuroCirCol 16 T Common-Coil Dipole Option for the FCC", *IEEE Transactions on Applied Superconductivity*, vol. 27, no. 4, pp. 1–5, Jun. 2017. DOI: 10.1109/TASC.2016.2641483.

[43] B. Auchmann *et al.*, "Electromechanical Design of a 16-T CCT Twin-Aperture Dipole for FCC", *IEEE Transactions on Applied Superconductivity*, vol. 28, no. 3, pp. 1–5, Apr. 2018. DOI: 10.1109/TASC.2017.2772898.

[44] B. Caiffi *et al.*, "Update on Mechanical Design of a $\cos\theta$ 16-T Bending Dipole for the Future Circular Collider", *IEEE Transactions on Applied Superconductivity*, vol. 28, no. 4, pp. 1–4, Jun. 2018. DOI: 10.1109/TASC.2018.2805918.

[45] Dassault Systèmes, *Opera Simulation Software, Version 18R2*, Oxfordshire, UK, 2018.

[46] P. Fabbricatore *et al.*, "Development of a Short Model of the Superconducting Separation Dipoles D2 for the High Luminosity Upgrade of LHC", *IEEE Transactions on Applied Superconductivity*, vol. 28, no. 3, pp. 1–5, Apr. 2018. DOI: 10.1109/TASC.2017.2772779.

[47] C. Lorin, M. Segreti, and M. Durante, "Design of a Nb3Sn 16 T Block Dipole for the Future Circular Collider", *IEEE Transactions on Applied Superconductivity*, vol. 28, no. 3, pp. 1–5, Apr. 2018. DOI: 10.1109/TASC.2018.2800692.

[48] V. Marinozzi *et al.*, "Conceptual Design of a 16 T $\cos\theta$ Bending Dipole for the Future Circular Collider", *IEEE Transactions on Applied Superconductivity*, vol. 28, no. 3, pp. 1–5, Apr. 2018. DOI: 10.1109/TASC.2018.2795533.

[49] E. Todesco. (2018). "HL-LHC magnet cross-sections", [Online]. Available: https://edms.cern.ch/document/1865374/4.

[50] D. Tommasini *et al.*, "Status of the 16 T Dipole Development Program for a Future Hadron Collider", *IEEE Transactions on Applied Superconductivity*, vol. 28, no. 3, pp. 1–5, Apr. 2018. DOI: 10.1109/TASC.2017.2780045.

[51] F. Toral, J. Munilla, and T. Salmi, "Magnetic and Mechanical Design of a 16 T Common Coil Dipole for an FCC", *IEEE Transactions on Applied Superconductivity*, vol. 28, no. 3, pp. 1–5, Apr. 2018. DOI: 10.1109/TASC.2018.2797909.

[52] J. Zhao *et al.*, "Mechanical stress analysis during a quench in CLIQ protected 16 T dipole magnets designed for the future circular collider", *Physica C: Superconductivity and its Applications*, vol. 550, pp. 27–34, 2018, ISSN: 0921-4534. DOI: https://doi.org/10.1016/j.physc.2018.04.003.

[53] A. Abada *et al.*, "FCC Physics Opportunities", *The European Physical Journal C*, vol. 79, no. 6, p. 474, Jun. 2019, ISSN: 1434-6052. DOI: 10.1140/epjc/s10052-019-6904-3.

[54] ——, "FCC-ee: The Lepton Collider", *The European Physical Journal Special Topics*, vol. 228, no. 2, pp. 261–623, Jun. 2019, ISSN: 1951-6401. DOI: 10.1140/epjst/e2019-900045-4.

[55] ——, "FCC-hh: The Hadron Collider", *The European Physical Journal Special Topics*, vol. 228, no. 4, pp. 755–1107, Jul. 2019, ISSN: 1951-6401. DOI: 10.1140/epjst/e2019-900087-0.

[56] ——, "HE-LHC: The High-Energy Large Hadron Collider", *The European Physical Journal Special Topics*, vol. 228, no. 5, pp. 1109–1382, Jul. 2019, ISSN: 1951-6401. DOI: 10.1140/epjst/e2019-900088-6.

[57] S. Balachandran *et al.*, "Beneficial influence of Hf and Zr additions to Nb4at%Ta on the vortex pinning of Nb_3Sn with and without an O source", *Superconductor Science and Technology*, vol. 32, no. 4, pp. 1–9, Feb. 2019. DOI: 10.1088/1361-6668/aaff02.

[58] A. Ballarino *et al.*, "The CERN FCC Conductor Development Program: A Worldwide Effort for the Future Generation of High-Field Magnets", *IEEE Transactions on Applied Superconductivity*, vol. 29, no. 5, pp. 1–9, Aug. 2019, ISSN: 2378-7074. DOI: 10.1109/TASC.2019.2896469.

[59] A. Bersani *et al.*, "The Superconducting Separation Dipoles MBRD for the High Luminosity Upgrade of LHC: From Short Model to Prototype", *IEEE Transactions on Applied Superconductivity*, vol. 29, no. 5, pp. 1–5, Aug. 2019. DOI: 10.1109/TASC.2019.2900598.

[60] A. Louzguiti *et al.*, "Optimization of the Electromagnetic Design of the FCC Sextupoles and Octupoles", *IEEE Transactions on Applied Superconductivity*, vol. 29, no. 5, pp. 1–5, Aug. 2019. DOI: 10.1109/TASC.2019.2892839.

[61] G. Montenero *et al.*, "Coil Manufacturing Process of the First 1-m-Long Canted–Cosine–Theta (CCT) Model Magnet at PSI", *IEEE Transactions on Applied Superconductivity*, vol. 29, no. 5, pp. 1–6, Aug. 2019. DOI: 10.1109/TASC.2019.2897326.

[62] A. Pampaloni *et al.*, "Preliminary Design of the Recombination Dipole for Future Circular Collider", *IEEE Transactions on Applied Superconductivity*, vol. 29, no. 5, pp. 1–4, Aug. 2019, ISSN: 2378-7074. DOI: 10.1109/TASC.2019.2892725.

[63] M. Prioli *et al.*, "The CLIQ Quench Protection System Applied to the 16 T FCC-hh Dipole Magnets", *IEEE Transactions on Applied Superconductivity*, vol. 29, no. 8, pp. 1–9, Dec. 2019, ISSN: 2378-7074. DOI: 10.1109/TASC.2019.2930705.

[64] A. M. Ricci and P. Fabbricatore, "A method for minimizing the magnetic cross-talk in twin-aperture cos-theta superconducting dipoles", *submitted to IEEE Transactions on Applied Superconductivity*, 2019. arXiv: 1910.06751 [physics.acc-ph].

[65] T. Salmi *et al.*, "Quench Protection of the 16 T Nb_3Sn Dipole Magnets Designed for the Future Circular Collider", *IEEE Transactions on Applied Superconductivity*, vol. 29, no. 5, pp. 1–5, Aug. 2019, ISSN: 2378-7074. DOI: 10.1109/TASC.2019.2895421.

[66] D. Schoerling *et al.*, "The 16 T Dipole Development Program for FCC and HE-LHC", *IEEE Transactions on Applied Superconductivity*, vol. 29, no. 5, pp. 1–9, Aug. 2019. DOI: 10.1109/TASC.2019.2900556.

[67] D. Schoerling and A. V. Zlobin, *Nb_3Sn Accelerator Magnets: Designs, Technologies and Performance*. Springer, 2019.

[68] M. Segreti *et al.*, "2-D and 3-D Design of the Block-Coil Dipole Option for the Future Circular Collider", *IEEE Transactions on Applied Superconductivity*, vol. 29, no. 5, pp. 1–4, Aug. 2019. DOI: 10.1109/TASC.2019.2892058.

[69] R. Valente *et al.*, "Baseline Design of a 16 T $\cos\theta$ Bending Dipole for the Future Circular Collider", *IEEE Transactions on Applied Superconductivity*, vol. 29, no. 5, pp. 1–5, Aug. 2019. DOI: 10.1109/TASC.2019.2901604.

[70] Wolfram Research, Inc., *Mathematica, Version 11.3*, Champaign, IL, 2019.

[71] ANSYS, Inc., *ANSYS*, Canonsburg, Pennsylvania.

Acknowledgments

I thank my supervisor, Dr. P. Fabbricatore, and the group members, Dr. A. Bersani, Dr. B. Caiffi, Dr. S. Farinon and Dr. R. Musenich.

I thank the external referees, Prof. M. Breschi and Prof. M. Greco.

I thank the teachers, Prof. M. Putti and Dr. E. Santopinto.

Finally, I thank all my friends in Genova.